University of Colorado, Boulder
CU Scholar

Mechanical Engineering Graduate Theses & Dissertations

Mechanical Engineering

Spring 1-1-2014

Flow Field Investigation of Hyperthermal MicroTubular Reactor Using CFD and DSMC Methods

Qi Guan
University of Colorado at Boulder, mech_guanqi@163.com

Follow this and additional works at: https://scholar.colorado.edu/mcen_gradetds

Part of the Mechanical Engineering Commons

Recommended Citation
Guan, Qi, "Flow Field Investigation of Hyperthermal MicroTubular Reactor Using CFD and DSMC Methods" (2014). *Mechanical Engineering Graduate Theses & Dissertations*. 89.
https://scholar.colorado.edu/mcen_gradetds/89

This Dissertation is brought to you for free and open access by Mechanical Engineering at CU Scholar. It has been accepted for inclusion in Mechanical Engineering Graduate Theses & Dissertations by an authorized administrator of CU Scholar. For more information, please contact cuscholaradmin@colorado.edu.

Flow Field Investigation of Hyperthermal MicroTubular Reactor Using CFD and DSMC Methods

by

Qi Guan

B.E., Southeast University, 2008

M.S., University of Colorado at Boulder, 2010

A thesis submitted to the

Faculty of the Graduate School of the

University of Colorado in partial fulfillment

of the requirements for the degree of

Doctor of Philosophy

Department of Mechanical Engineering

2014

This thesis entitled:
Flow Field Investigation of Hyperthermal MicroTubular Reactor Using CFD and DSMC Methods
written by Qi Guan
has been approved for the Department of Mechanical Engineering

Prof. John W. Daily

Prof. G. Barney Ellison

Date

The final copy of this thesis has been examined by the signatories, and we find that both the content and the form meet acceptable presentation standards of scholarly work in the above mentioned discipline.

Guan, Qi (Ph.D., Mechanical Engineering)

Flow Field Investigation of Hyperthermal MicroTubular Reactor Using CFD and DSMC Methods

Thesis directed by Prof. John W. Daily

Thermal decomposition reaction is an interesting yet challenging subject in biomass gasification process. For a number of years, researchers at CU-Boulder and NREL have been studying the pyrolysis chemistry of typical biomass compounds by cracking them in a hyperthermal tubular reactor. Downstream of the reactor, matrix isolation/infrared spectroscopy (MI/IR) or photoionization mass spectrometry (PIMS) is used to diagnose products generated in the process. To study the pyrolysis reaction mechanism and kinetics, one needs to characterize the thermal and fluid properties in the system. The reactors are typically 2 to 4 cm in length with an i.d. of 0.5 to 1 mm. Direct experimental measurements of the thermodynamic states distribution are difficult to conduct due to the small geometry and high operating temperatures (up to 1800 K). Thus there has been little learned about the details of the internal flow field, the downstream molecular flow in the vacuum chamber or the chemical kinetics throughout the system. In this thesis, numerical methods of computational fluid dynamics (CFD) and direct simulation Monte Carlo (DSMC) are used to obtain the thermal and fluid information. Presented are simulation results within and downstream of the reactor under different operating conditions. We conclude that both continuum and non-equilibrium flows exist in the system. In order to solve the flow field transitions between the two flow regimes, hybrid CFD/DSMC algorithms are implemented and results are discussed in detail. The hybrid approach provides us with a complete picture of the distribution of the thermodynamic and flow properties for quantitative kinetics studies.

Dedication

To my family and friends.

Acknowledgements

The past six years as a graduate student at CU Boulder has been a difficult yet interesting journey. I began with my graduate studies with barely any experience in any kind of research activity and I am now happy to find that I finally may know a little bit. Combustion is such a complicated subject!

Firstly, I would like to thank my thesis advisor, Professor John W. Daily, for guiding me through my research during these years. He has been very patient about my progress and always offers helpful opinions, poses challenging questions and provides much-needed help. I am surprised that he can still work energetically and efficiently in his 70s, not only as a good advisor but also a university teacher and a golf player. His colorful career has led me to think seriously how to plan a productive career of my own.

Secondly, I would like to thank the other team members in the Chemistry department, especially Kim, Tom, AJ and Dr. Musa's group at Berkeley. They have carried out numerous experimental measurements just to validate my simulation results. It is their enthusiastic help that has made this work possible. I also need give special thanks to Professor G. Barney Ellison for his constantly challenging questions related to chemistry.

Thirdly, I would like to thank my other committee members. Professor Vasilyev and Professor Hamlington have provided guidance on the CFD portions of my work and Professor Argrow and his student Dr. Turanski have provided important assistance with the DSMC methods.

Finally, I would like to thank my parents for their patience, my wife Yuchen for her mental support and nice dinner and my daughter Georgia who hasn't had any complaints ever since she

was born.

Contents

Chapter

1 Introduction 1

1.1 Background and motivation 1

1.2 Pyrolysis experiments 4

1.3 General flow considerations 8

1.4 Discussion of numerical methods 10

1.4.1 Continuum flow and computational fluid dynamics (CFD) 12

1.4.2 Rarefied flow and direct simulation Monte Carlo (DSMC) 12

1.4.3 Coupling of CFD/DSMC 13

1.5 Thesis organization 14

2 Simple Flow Analysis 15

2.1 Continuous flow inside the reactor 15

2.2 Role of wall reactions: the Peclet number 19

2.3 Role of secondary radical reactions 21

2.4 Rarefied flow in the vacuum chamber 22

3 Reactor Simulations with CFD Method 29

3.1 Impact of carrier gas 32

3.2 Impact of wall temperature 36

3.3 Impact of flow rate 36

3.4 Impact of reactor diameter 39
3.5 Impact of reactor length 42
3.6 Reacting flow simulation 46
3.6.1 Cyclohexene decomposition in helium 49
3.6.2 Cyclohexene decomposition in argon and neon 55

4 Development of CFD and DSMC Codes 59
4.1 CFD solver 59
4.1.1 Finite volume method (FVM) 59
4.1.2 Multi-block data structure 61
4.1.3 Time integration methods 63
4.1.4 Pressure boundary condition 63
4.1.5 Density based method 64
4.2 DSMC solver 65
4.2.1 DSMC basics 65
4.2.2 DSMC components 66
4.2.3 Multi-block data structure 68
4.2.4 Macroscopic stream boundary 69
4.2.5 Species weighting factor 69
4.3 Hybrid CFD/DSMC methods 74
4.3.1 Zonally-decoupled CFD/DSMC method 76
4.3.2 Fully coupled CFD/DSMC method 76
4.3.3 Hybrid code structure 77

5 Downstream Vacuum Simulations with DSMC Method 79
5.1 Supersonic jet expansion 81
5.1.1 Important properties 81
5.1.2 DSMC simulations of the expansion region 82

5.2 Ideal molecular beam performance 89

5.3 DSMC simulation of the skimmer interference 90

5.3.1 Reactor-skimmer distance l_s 92

5.3.2 Skimmer entry diameter D_s 95

5.3.3 Adsorption coefficient α_s 97

5.3.4 Carrier gas 97

5.4 Seeded species in carrier gas 100

6 Conclusion and Future Work 106

6.1 Conclusion 106

6.2 Future Work 106

Bibliography 108

Appendix

A Physical Properties of He, Ne, Ar and SiC 114

B The Navier-Stokes Equations 117

C CFD: Conversion from 2D to 2D axially symmetric 119

Tables

Table

1.1 Reactor geometry 6

1.2 Downstream geometry 8

1.3 Operating conditions 8

3.1 Thermal accommodation coefficients of helium for different T_{wall} 31

3.2 Reactors for parametric study 32

5.1 Modeled cases of downstream expansion 83

5.2 Physical properties of helium, xenon and oxygen used in mixture expansion 102

A.1 Physical properties of helium, neon and argon 114

A.2 Physical properties of SiC 116

Figures

Figure

1.1 Pulsed reactor and IR diagnostic 2

1.2 CW reactor and PIMS diagnostic 2

1.3 Skimmer used in PIMS diagnostic 3

1.4 Experimental arrangement of CW and pulsed reactors 7

1.5 Supersonic jet expansion 9

1.6 Knudsen number and mathematical models 11

1.7 Gas dynamics regimes 11

2.1 Comparison of residence and diffusion times for acetaldehyde in helium and argon . 20

2.2 Supersonic jet beam and skimmer sampling 24

2.3 Temperature as a function of downstream distance from reactor exit 26

2.4 Knudsen numbers as a function of downstream distance 27

3.1 CFD modeled geometry 31

3.2 Centerline pressure and temperature distributions with $T_{wall} = 1500$K 33

3.3 Centerline velocity and Mach number distribution with $T_{wall} = 1500$K 33

3.4 Centerline Knudsen number distribution with $T_{wall} = 1500$K 34

3.5 Radial velocities with $T_{wall} = 1500$K 35

3.6 Radial temperatures with $T_{wall} = 1500$K 35

3.7 Centerline pressure and temperature distributions as a function of wall temperature 36

3.8 Centerline velocity distributions as a function of wall temperature 37

3.9 Centerline Mach number distributions as a function of wall temperature 37

3.10 Knudsen number distributions as a function of wall temperature 38

3.11 Centerline pressure and temperature distributions as a function of flow rate 39

3.12 Centerline velocity distributions as a function of flow rate 40

3.13 Centerline Mach number distributions as a function of flow rate 40

3.14 Knudsen number distributions as a function of flow rate 41

3.15 Centerline pressure and temperature distributions with different reactor diameters . 43

3.16 Centerline velocity distributions with different reactor diameters 43

3.17 Centerline Mach number distributions with different reactor diameters 44

3.18 Centerline Knudsen number distributions with different reactor diameters 45

3.19 Centerline pressure and temperature distributions with different reactor lengths . . . 46

3.20 Centerline velocity distributions with different reactor lengths 47

3.21 Centerline Mach number distributions with different reactor lengths 47

3.22 Centerline Knudsen number distributions with different reactor lengths 48

3.23 Mole fraction of cyclohexene: T_{wall} = 1500K, 280 sccm, reactor #1, He 50

3.24 Mole fraction of cyclohexene: T_{wall} = 1200-1500K, 280 sccm, reactor #1, He 51

3.25 Radial mole fraction of cyclohexene at reactor exit: 280 sccm, reactor #1, He 51

3.26 Percent conversion of cyclohexene vs. temperature: T_{wall} = 1200-1500K, 280 sccm, reactor #1, He 52

3.27 Pressure/Temperature product vs. distance: T_{wall} = 1200-1500K, 280 sccm, reactor #1, He 53

3.28 Cyclohexene decomposition rate vs. distance: T_{wall} = 1200-1500K, 280 sccm, reactor #1, He 54

3.29 Cyclohexene decomposition rate constant vs. distance: T_{wall} = 1200-1500K, 280 sccm, reactor #1, He 55

3.30 Comparison of "experimental" rate constant from CFD simulations with rate constants calculated at the effective temperature and pressure: T_{wall} = 1200-1500K, 280 sccm, reactor #1, He 56
3.31 Mole fraction of cyclohexene vs. distance: T_{wall} = 1500K, 280 sccm, reactor #1, Ar 57
3.32 Pressure/Temperature product vs. distance: T_{wall} = 1200-1500K, 280 sccm, reactor #1, Ar 58
3.33 Cyclohexene decomposition rate vs. distance: T_{wall} = 1200-1500K, 280 sccm, reactor #1, Ar 58

4.1 CFD program cycle 60
4.2 Three-block structure of the pyrolysis reactor 61
4.3 Message data type for CFD code 61
4.4 Block data type for CFD code 62
4.5 Mesh data type for CFD code 63
4.6 Computing cycle of typical DSMC programs 67
4.7 Block data type for DSMC code 70
4.8 Downstream multiblock mesh for DSMC simulation 71
4.9 Standard and reservoir boundary conditions for DSMC 72
4.10 Split-merge method in conservative collision scheme 75
4.11 Code structure for hybrid CFD/DSMC 78

5.1 Effusive oven beam and supersonic nozzle beam 80
5.2 Geometry and multi-block mesh of the DSMC model 84
5.3 Mach number contour in a supersonic underexpanded jet 84
5.4 Knudsen number contour of a supersonic underexpanded jet 85
5.5 Log10 of number density contour in a supersonic underexpanded jet 85
5.6 Downstream centerline number density in log10 format 86
5.7 Downstream centerline temperature 86

5.8 Downstream centerline velocity 87

5.9 Downstream centerline Mach number 87

5.10 Terminal velocity validation by experiment 88

5.11 Important parameters impacting beam performance (adapted from [4]) 89

5.12 Cone shaped skimmer in molecular beam simulations 91

5.13 Log10 of number density contour 92

5.14 Centerline number vs. distance with different reactor-skimmer distance 93

5.15 Centerline velocity vs. distance with different reactor-skimmer distance 93

5.16 Centerline temperature vs. distance with different reactor-skimmer distance 94

5.17 Centerline number density vs. distance with different skimmer entry diameter 95

5.18 Centerline velocity vs. distance with different skimmer entry diameter 96

5.19 Centerline temperature vs. distance with different skimmer entry diameter 96

5.20 Centerline number density vs. distance with different adsorption coefficient 98

5.21 Centerline velocity vs. distance with different adsorption coefficient 98

5.22 Centerline temperature vs. distance with different adsorption coefficient 99

5.23 Centerline number vs. distance with different carrier gas 100

5.24 Centerline velocity vs. distance with different carrier gas 101

5.25 Centerline temperature vs. distance with different carrier gas 101

5.26 Log10 of number density contour in a pumping system 103

5.27 Mole fractions of O_2, Xe and He along centerline 104

5.28 Mole fraction ratio of O_2 and Xe vs. He along centerline 104

A.1 Thermal conductivity of helium and argon 115

A.2 Dynamic viscosity of helium and argon 116

B.1 Axisymmetic coordinate system used in simulations 117

C.1 Computing cycle of typical CFD programs 119

Chapter 1

Introduction

1.1 Background and motivation

Generating alternative fuels from biomass materials using pyrolysis techniques has long been considered an important research topic. At CU-Boulder [75, 69] and NREL [38, 54], we focus on studying the decomposition reaction mechanisms and chemical kinetics of typical biomass species. The experiments are carried out in a highly heated micro-tubular reactor under a pulse or CW mode. In recent years, we have become interested in quantifying the pyrolysis reactions. This requires a complete knowledge of the thermodynamic data inside the reactor, which are typically obtained by direct measurements. However, in our case, the small dimensions make this a formidable task. Probing a thermocouple would severely disturb the flow field and optical access is very difficult. As a result, we must use numerical tools to characterize the flow and validate the results by comparing them with limited measurements. A brief description of the nature of the flow field is given in sec. 1.3 and numerical methods used throughout this work are discussed in sec. 1.4.

The flow reactor assembly is shown in Fig. 1.1 and Fig. 1.2. During the experiments, dilute biomass species (usually 0.1% or less in molar ratio) mixed with carrier noble gas (helium or argon) will be fed into the reactor from a high-pressure reservoir. If a CW reactor is used, the flow field inside the reactor will reach a steady state. A mass controller is used to modulate the amount of gas coming into the system. The pressure upstream from the reactor is measured. Two electrodes are attached on the reactor to generate heat using an external current. The heating temperature on the reactor surface can be roughly measured using a thermal couple. When flow passes through

Figure 1.1: A pulsed reactor with infrared spectrometry diagnostic

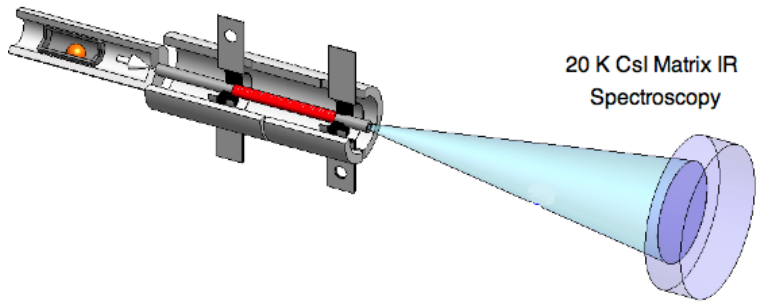

Figure 1.2: A CW reactor with photoionization mass spectrometry diagnostic

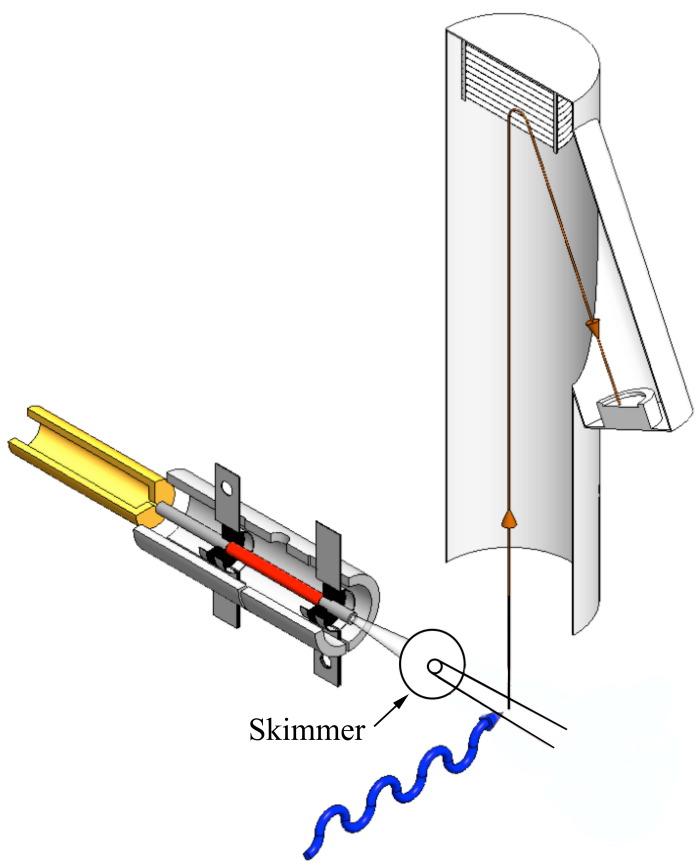

Figure 1.3: Skimmer used to separate source chamber and diagnostic chamber in PIMS system

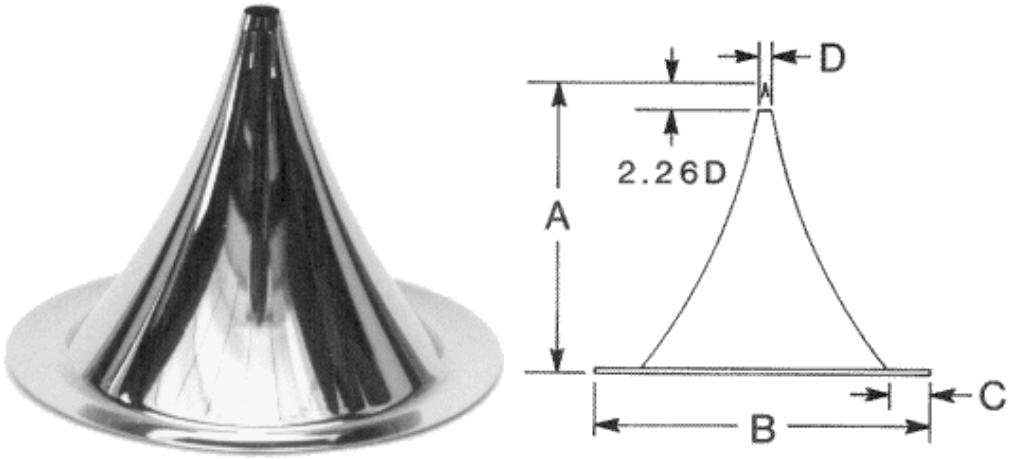

the reactor, pyrolysis reactions take place. Then reactants will be decomposed into products and expanded into the following vacuum chambers, which are often held at low pressure (around 10^{-5} torr).

Typically, the decomposed products from the pyrolysis process are analyzed by either infrared (IR) spectroscopy or photoionization mass spectrometry (PIMS). In a PIMS system, as shown in Figure 1.2, there are two vacuum chambers. The first chamber (held at about 10^{-4} torr by a mechanical pump) is called the source chamber and the second chamber (held at 10^{-7} torr by a diffusion pump) is called the diagnostic chamber. They are separated by a small-diameter skimmer (shown in Figure 1.3) to form a molecular beam. When the molecular beam reaches the end of the diagnostic chamber, a laser beam is used to ionize the molecules. The ions are then diagnosed by the time-of-flight.

1.2 Pyrolysis experiments

Our experimental facility has made the study of the initial decomposition reactions possible. It involves a small (1 mm i.d., 2-3 cm long) flow reactor and is equipped with advanced diagnostics. Based on the well known "Chen Nozzle" [24], the residence time in the reactor is very short, typically 50-150 microseconds, allowing for a study of the earliest kinetic processes. The diagnostics, matrix isolation/infrared spectroscopy (IR) and photoionization mass spectroscopy (PIMS), in combination allow us to identify all species present assuming the number of species is reasonably small. This includes radials as well as stable species. However, a major disadvantage of the system is a lack of understanding of the internal fluid dynamics. Without detailed knowledge of the velocity, temperature and density distributions within the reactor, it is not possible to extract reliable kinetic information.

Depending on the pumping capability the flow is either pulsed or run continuously. At present we pulse the flow in our labs (CU-Boulder and NREL), but run continuously at the Advanced Light Source (ALS). The reactor is electrically heated, either resistively using conducting materials (SiC or other metals) or via nichrome wire for non-conducting materials (alumina/quartz). Most of our

work has been with SiC which is tolerant of high temperatures and is inert on surface chemistry. We typically run a very dilute single reactant (less than 0.1% in an atmosphere of He, Ar or Ne) and observe its unimolecular decomposition. Because the residence times are so short, we generally collect only very early products. This is the first major advantage of the system.

The second advantage comes from the diagnostics. In matrix isolation/IR spectroscopy the exhaust from the reactor expands into a hard vacuum onto a CsI window held at a temperature low enough to freeze the carrier gas along with any other species present. The reactor is operated for a period of time until the frozen layer becomes sufficiently thick to allow detection by absorption spectroscopy, typically carried out with an FTIR spectrometer. Because the temperature is so low the resulting vibrational spectra are quite clean, usually allowing unambiguous identification. In the PIMS apparatus the products from the reactor are ionized with vacuum ultraviolet (VUV) photons and detected with a time-of-flight mass spectrometer. The underexpanded jet from the tube exit is skimmed and the resulting molecular beam intersected by a VUV light source (either 10.5 e.v. laser photons in our laboratory or energy tunable synchrotron radiation at ALS). We can also use multiphoton ionization for very precise species identification. Thus, the methods are complementary in the sense that we can detect all species (including organic and atomic radicals) with PIMS, and can identify organics using IR. To date, we have mostly worked with molecules that are of interest in biomass gasification. This includes 2-phenethyl phenyl ether [38], methoxyphenols [53, 55], furans [74, 76], and acetaldehyde [75, 73]. We have recently begun to look at the unimolecular decomposition of large fuel molecules, including JP-10, dicyclopentadiene and cyclohexene.

Based on the simple geometry and the known operating conditions of such systems we can speculate on the characteristics of the flow. If the mass flow rate is sufficiently high to maintain continuum flow inside the reactor, it is known that the following occurs. Because of friction and heating effects, the flow will accelerate and the pressure will drop. At the tube exit the flow will choke, i.e. the local flow velocity equals the local speed of sound. Downstream of the exit, an underexpanded, supersonic jet forms. The expansion within the jet is nearly isentropic and the pressure, density and temperature drop rapidly with downstream distance. Supersonic jets

have been used extensively in molecular studies because low temperatures translate into much simpler optical or ionization spectra. The other limit, that of low mass flow rate, is an entirely different process. Here the flow rarefies within the reactor and at the exit become effusive in nature. Therefore, as part of understanding the flow in general, a goal is to clearly define the appropriate operating conditions and their effects on flow both within and downstream of the reactor.

The small reactors we use in our experiments are variants of Peter Chen's nozzle [24, 25, 16, 23, 51, 84]. Tables 1.1-1.3 list the reactor geometries, skimmer and interaction size and distances, and flow conditions of the reactors we have used. Most of our experiments are carried out with SiC tubes which can be electrically heated to approximately 1800 K. The electrical current is supplied via small electrode clips attached to the reactor.

The overall experimental setup is illustrated in Fig. 1.4. As mentioned previously, we run CW at the Advanced Light and pulsed in Colorado. The flow rate is recorded with a unit of standard cubic centimeter per minute (sccm). For the CW cases we have run with carrier gas volumetric flow rates of 25 sccm to 300 sccm, although as our discussion indicates, we have now settled on running at the upper limit of this range to insure mostly continuum flow in the reactor and a well formed supersonic expansion downstream. During an experiment, the volumetric flow rate is controlled using a mass flow controller, and the pressure just upstream of the reactor and in the downstream chambers are measured. The upstream pressure typically ranges from 100 torr to 300 torr depending on the heating temperature and flow rate. For pulsed flow, the flow rate is determined by the time dependent geometry of the valve pintle and orifice and is not well known.

Table 1.1: Reactor geometry
(ALS-LBNL Advanced Light Source, SLS - Swiss Light Source)

Reactor	Experiment	Diameter (mm)	Length (mm)	Heated Length (mm)
Pulsed He SiC	118.2nm PIMS	1.0	38.3	18.7
Pulsed Ar SiC	Ar Matrix	1	27.4	10.6
Pulsed Ne SiC	Ne Matrix	1	38.3	18.7
CW He SiC	ALS PIMS	0.66	25.4	15
CW Ar SiC	SLS PIMS	1	30	15

Figure 1.4: Experimental arrangement of CW and pulsed reactors

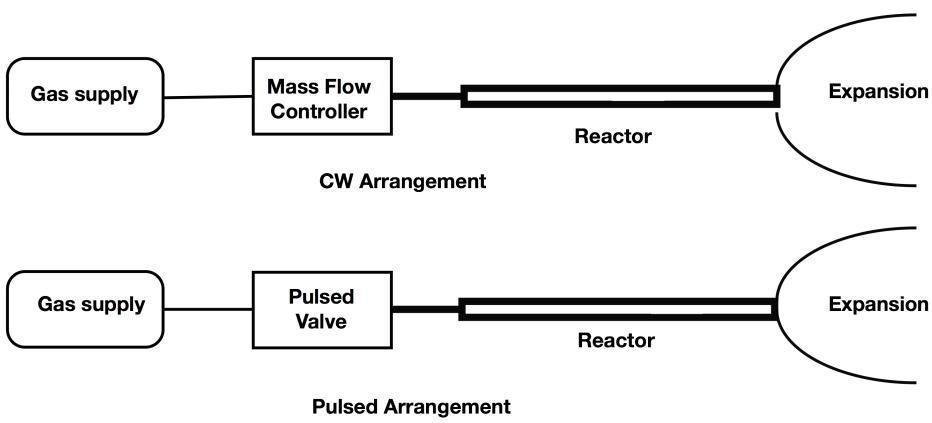

Table 1.2: Downstream geometry

Reactor	Experiment	Skimmer Entry Diameter (mm)	Skimmer Exit Diameter (mm)	Interaction Region Distance (mm)
Pulsed He SiC	118.2nm PIMS	1	10	178
Pulsed Ar SiC	Ar Matrix	N/A	N/A	42
Pulsed Ne SiC	Ne Matrix	N/A	N/A	45
CW He SiC	ALS PIMS	2	10	150
CW Ar SiC	SLS PIMS	2	5	260

Table 1.3: Operating conditions

Reactor	Experiment	Flow Rate (sccm)	Upstream Pressure (Torr)	Downstream Pressure (Torr)
Pulsed He SiC	118.2nm PIMS	N/A	1500-2000	10^{-6}
Pulsed Ar SiC	Ar Matrix	N/A	800	10^{-5}
Pulsed Ne SiC	Ne Matrix	N/A	800	10^{-8}
CW He SiC	ALS PIMS	280	100-300	10^{-6}
CW Ar SiC	SLS PIMS	280	50	10^{-6}

1.3 General flow considerations

The character of a given flow field is determined by the geometry and initial and boundary conditions. In general, the velocity field is obtained from the velocity distribution which is described by Boltzmann's equation:

$$\frac{\partial}{\partial t}[nf] + \mathbf{c} \cdot \frac{\partial}{\partial \mathbf{x}}[nf] = \left\{ \frac{\partial}{\partial t}[nf] \right\}_{collison} \tag{1.1}$$

Boltzmann's equation is an integral-differential equation and is difficult to solve. However, if the density throughout is large enough then the flow is said to be continuous and, in principle, is described by the Navier-Stokes equations which arise out of a limiting solution of Boltzmann's equation. The critical parameter for deciding whether the continuous limit holds is the Knudsen number, which is the ratio of the collision mean free path to a characteristic length. For a tube,

$$Kn = \frac{\lambda}{d} \tag{1.2}$$

Figure 1.5: Free jet transition to free molecular flow

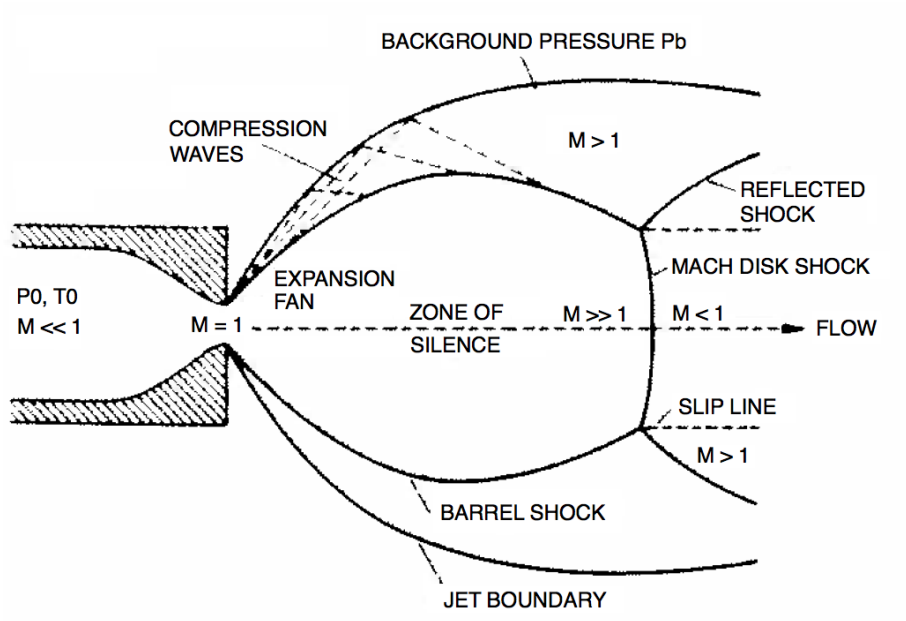

where λ is the mean free path and d the tube diameter. The Knudsen number is related to the familiar parameters of fluid mechanics, the Mach number M and the Reynolds number Re, i.e.

$$M = \frac{U}{a} \quad \text{and} \quad Re = \frac{Ud}{\mu} \tag{1.3}$$

where U is the local flow velocity, a is the local speed of sound and μ is the dynamic viscosity. One can show that

$$Kn = 1.26\sqrt{\gamma}\frac{Ma}{Re} \tag{1.4}$$

where γ is the ratio of specific heats. For monatomic gases, γ is approximately 1.6667.

Based on an appropriately defined Knudsen number, one may divide a flow into various regimes. One such division by Bird [10] is shown in Fig. 1.6. Here the continuum domain corresponds to small values of the Knudsen number. At the opposite limit of a large Knudsen number the flow becomes collisionless. A somewhat more refined division was given by Schaaf and Chambre [52] in which four flow regimes were defined: continuum flow, slip flow, transition flow, and free molecular flow. They are illustrated in Fig. 1.7. As we shall indicate, the Reynolds numbers for our flows range from approximately 100-1000, while the Mach number increases from a small value at the reactor inlet to unity near the exit. Based on Fig. 1.7 we should be concerned that some portion of the flow is in the slip regime. The slip regime corresponds to a range of Knudsen numbers based on the local velocity gradient from about 0.1 to 1. This does turn out to be the case for some operating conditions. Regardless, once the flow exits the reactor the density (and temperature and pressure) drops rapidly and transitions to free molecular flow within a diameter or two of the exit.

1.4 Discussion of numerical methods

As stated above, the flow field in the system is very complex. Since it contains both continuum and noncontinuum parts, different numerical methods should be applied in different areas.

Figure 1.6: Knudsen number and appropriate mathematical models (adapted from [10])

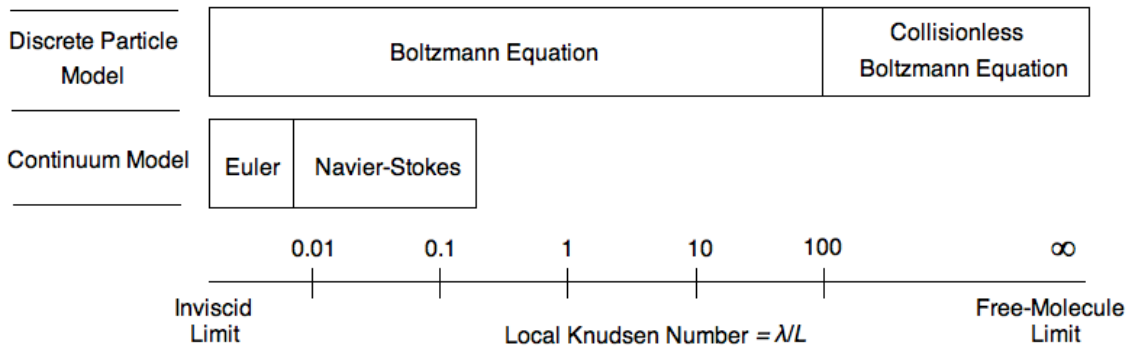

Figure 1.7: Regimes of gas dynamics (adapted from [52])

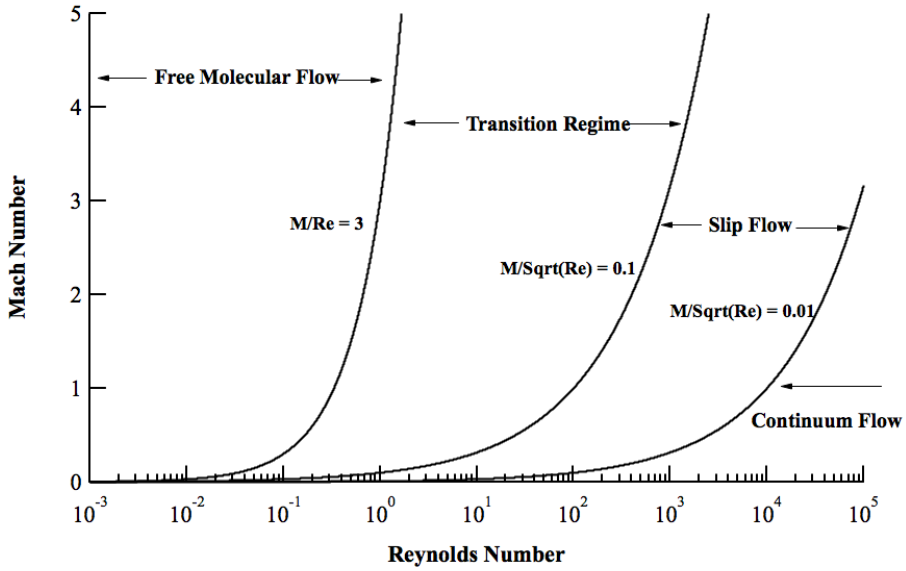

Computational fluid dynamics (CFD) [15] is considered as an appropriate tool for the continuum flow and direct simulation Monte Carlo (DSMC) [10] for the noncontinuum flow. Transition from continuum to noncontinuum varies with the operating conditions, e.g. flow rates, heating temperatures and reactor geometry. Thus we should use a hybrid CFD/DSMC [82, 56, 1] approach that can determine the transition location and communicate information between them.

1.4.1 Continuum flow and computational fluid dynamics (CFD)

Under almost all circumstances the flow field near the entry to the reactor is in the continuum domain. In this domain, the flow may be described by the Navier-Stokes equations (Appendix B). They were first derived in 1822 by Navier [46] based on molecular theory. They were later derived by Stokes using the more familiar methods outlined in modern fluid dynamics text books [6]. A rigorous derivation starts with the velocity distribution function. The Chapman-Enskog solution of the Boltzmann equation results in the macroscopic transport properties. For multicomponent, reacting, compressible flow, the conservations of mass, individual species, momentum and energy are required.

Once a problem has been formulated by providing the appropriate form of the above equations along with initial and boundary conditions, the problem of solving the equations remains. Except for particularly simple geometries and physical conditions, this is not readily possible using analytic methods. As a result, most problems are solved numerically. This is the domain of Computational Fluid Dynamics (CFD). The partial differential Navier-Stokes equations are replaced with discrete forms, either finite differences or volumes. Thus the problem becomes one of solving simultaneous algebraic equations. There are a variety of possible approaches and appropriate methods depending on the flow conditions.

1.4.2 Rarefied flow and direct simulation Monte Carlo (DSMC)

When the local Knudsen number begins to exceed 0.1, the Navier-Stokes equations no longer apply and particulate methods must be used to simulate the flow field. Direct Simulation Monte

Carlo (DSMC) is a discrete particle dynamics method first proposed by Bird [10]. To control computation costs, Bird introduced the idea of representative particles, where each particle carried by the simulation represents a large number of real molecules, typically several orders of magnitude. (The ratio of real to simulated particles is called the "scaling factor".) Thus, unlike molecular dynamics where particle trajectories are followed throughout collisions based on atomic forces, particle movement and collisions are carried out separately in time, with collisions being treated statistically. This requires time steps considerably less than the mean collision time be used when solving for particle motion. Particles are moved deterministically, then collisions are simulated probabilistically. A variety of physical collision models have been developed including the hard sphere (HS) model, the variable hard sphere (VHS) model, and the variable soft sphere (VHS) model. At regular user-selected intervals the flow is sampled to determine the mean flow properties including density, velocity, temperature and pressure. For stationary flows these properties are monitored until satisfactory levels of signal to noise ratios are achieved. One needs to carefully choose the time step, cell size and scaling factor in order to obtain accurate results and maintain reasonable computational cost at the same time.

1.4.3 Coupling of CFD/DSMC

Since the flow transitions from continuum to collisionless as it passes through the reactor and expands at the reactor exit, neither CFD nor DSMC is suitable for modeling the entire flow field. In this case, a hybrid method is required that matches CFD for the continuum portion of the flow field, and DSMC for the rarefied and collisionless portion. There are several approaches to couple CFD and DSMC, the two main approaches being zonally decoupled and state-based fully coupling. The zonally decoupled method is suitable for flow where there is a fairly clear separation between a subsonic continuum region and a supersonic, low density region. This is the present case as the downstream pressure is very low, and the reactor flow chokes at the exit and then rapidly expands in the vacuum chamber. Thus, the zonally decoupled method is chosen as our major coupling method.

1.5 Thesis organization

The remainder of the thesis is organized as following. In Chapter 2, the basic fluid dynamics is analyzed from a theoretical point of view. In Chapter 3, we carry out detailed simulations about the fluid dynamics inside the reactor using commercial CFD software. The impacts of different operating conditions on the fluid dynamics are analyzed. In Chapter 4, we introduce the CFD and DSMC codes written for the project. The structures and features are illustrated. Based on these two codes, we further introduced how to implement the hybrid CFD/DSMC algorithm. In Chapter 5, we show the simulation results downstream using our DSMC code and the DS2V code. Skimmer interferences on the molecular beam behavior are discussed. Finally, Chapter 6 summaries the contribution of this thesis and briefly examines possible avenues for future inquiry.

Chapter 2

Simple Flow Analysis

For certain simplifying assumptions, the Navier-Stokes equations can be solved directly for flow in a constant area tube. In this chapter we illustrate some features of the flow this way, while also pointing out deficiencies in the simple solution that ultimately require numerical simulations. For the expansion flow downstream of the reactor, one can also reach some conclusions based on simple isentropic theory and by utilizing experimental correlations for the flow properties.

2.1 Continuous flow inside the reactor

The reactor has a very simple geometry, involving a straight pipe with a constant diameter. Assuming that the flow within the tube lies entirely within the continuum regime, it can be described by the Navier-Stokes equations. An important non-dimensional relation is the Reynolds number, defined as:

$$Re = \frac{\rho U d}{\mu} \tag{2.1}$$

Here ρ is the mass density, U is the average gas velocity in the tube, D is the tube diameter, and μ is the dynamics viscosity. It is well known that if the Reynolds number is less than about 2300 the flow is laminar. A special limit of a laminar flow, Poiseuille flow, has a similar scenario where the density is constant and the velocity is unchanging with distance along the tube. This is called a fully developed flow. For Poiseuille flow the average velocity is related to the axial pressure gradient by:

$$U = -\frac{dP}{dz}\frac{r_0^2}{8\mu} \tag{2.2}$$

and the radial velocity distribution becomes

$$U = -\frac{dP}{dz}\frac{d^2}{4\mu}\left[1 - \left(\frac{r}{r_0}\right)^2\right] \tag{2.3}$$

where r_0 is the tube radius. Referring to such a flow as fully developed indicates that entrance effects are not important, and thus flow conditions are described by the above equations. Note that for a fully developed, constant density flow the pressure gradient is equal to the inlet pressure minus the outlet pressure divided by tube length.

While these results are not exact in our case, some important conclusions can be reached. First, the velocity in the tube is directly proportional to the pressure gradient and inversely proportional to the viscosity. Alternatively, if we solve for the pressure gradient, it is directly proportional to the viscosity and inversely proportional to the velocity. Since operationally we fix the volumetric flow rate at the inlet and thus the average velocity, the pressure drop across the tube will change as we heat the tubde due to the temperature dependency of the viscosity. It is the case that the viscosities of both helium and argon are proportional to temperature to about the 0.7 power (see Appendix A). In addition, carrier gases with different viscosities will result in different pressure gradients.

At the inlet of the tube flow, if the upstream plenum is large enough, the flow presents as uniform in velocity, pressure and temperature. Because of the no-slip condition at the tube walls, the velocity there is by necessity zero. As a result, boundary layers develop along the walls and the flow evolves along the axial direction until the boundary layers merge at the centerline. Eventually, the flow becomes fully developed and is described by the above equations. There are correlations for the so-called entrance length, or the distance to the point where the flow becomes fully developed. For a laminar flow the accepted correlation is:

$$\frac{L_e}{d} \simeq 0.06\ Re \tag{2.4}$$

The Reynolds number in our flows range from 70-150. At the upper extreme one would have $L_e/d \simeq 9$. For a 1 mm tube, the entry length would thus be about nine millimeters, almost a centimeter. Therefore, while the simple solutions are useful in guiding our understanding they are not sufficient for providing the level of accuracy needed for quantification.

We have not yet addressed the temperature distribution, which is obviously important given the strong non-linear dependence of reaction rate constants on temperature. Like momentum, there are simple solutions to the energy equation if we assume a steady-state, laminar, incompressible, fully developed flow. Furthermore, if we assume that the heat flux from the wall does not vary with axial distance, then one can show that the rate of temperature change in the tube is a constant:

$$\frac{\partial T}{\partial z} = \text{ const} \tag{2.5}$$

This is not true in our case, but the assumption is useful. Solving the heat equation under these assumptions results in the following expression for the temperature with respect to the centerline temperature:

$$T(r) - T_{r=0} = \frac{1}{\alpha}\frac{\partial T}{\partial z}\frac{u_0 r_0^2}{4}\left[\left(\frac{r}{r_0}\right)^2 - \frac{1}{4}\left(\frac{r}{r_0}\right)^4\right] \tag{2.6}$$

Here $\alpha = k/\rho c_p$ is the thermal diffusivity. Therefore, if the centerline temperature is less than the wall temperature, which it will be at the entrance and for some distance downstream, there is a parabolic temperature distribution. However, at some point the temperature across the tube will reach the wall temperature and from then on will be constant. The distance over which this takes place is called the thermal entry length. One correlation available is given as:

$$\frac{L_{e_{Th}}}{d} = 0.033\ RePr \tag{2.7}$$

where $Pr = \frac{c_p \mu}{k}$ is the Prandtl number which for helium is around 0.683. For a Reynolds number of 150, the thermal entry length is about 1.3 mm so we would expect the flow to fairly rapidly approach the wall temperature and be constant from then on. For argon, however, the Reynolds/Prandtl product is about 230 times that of helium. Thus, for argon one would not expect the flow on the interior of the tube to reach the wall temperature.

Finally we come to the crux of the matter: how will these distributions affect the rate at which reactions take place. Consider a simple unimolecular reaction A $\rightarrow$ Products. In this case the rate equation for the disappearance of A is:

$$\frac{d[\mathrm{A}]}{dt} = -k(T)[\mathrm{A}] \tag{2.8}$$

where $k(T)$ is the temperature-dependent reaction rate constant. If the temperature is constant then the concentration of A will decrease exponentially. If the velocity within the tube were constant throughout then the concentration at the end of the tube would simply be:

$$[\mathrm{A}]_L = [\mathrm{A}]_0 e^{-k\tau_{res}} \tag{2.9}$$

where $\tau_{res} = L/U$ is the residence time. However, the velocity within the tube varies as described above and thus is not constant. Consequencely there is a distribution of residence times. Furthermore, while the thermal entry length is short, it is finite. Therefore, neither of the above assumptions hold.

For fully developed, constant density laminar pipe flow, one can show [27] that the age, or residence time distribution E, in the absence of diffusion is of the form τ/t^2 where τ is the residence time based on the average velocity. Diffusion will modify this distribution. For the case with a constant temperature but including diffusion Wehner and Wilhelm [78] showed (see Levenspiel [43]) that the average exit concentration for a first order reaction is then:

$$\frac{C_L}{C_0} = \frac{4a\exp(\tau_D/2)}{(1+a)^2\exp(a\tau_D/2) - (1-a)^2\exp(-a\tau_D/2)} \tag{2.10}$$

where

$$a = \sqrt{1 + 4k\tau/\tau_D} \quad \text{and} \quad \tau_D = \frac{\bar{u}L}{D} \tag{2.11}$$

and D is the effective diffusion coefficient defined as:

$$D = D_{molecular} + \frac{\bar{u}^2 d^2}{192 D_{molecular}} \tag{2.12}$$

where $D_{molecular}$ is the molecular diffusion coefficient.

However, since the basic assumptions for the residence time distribution are not satisfied, a more complete analysis is required. The consequence is that numerical methods are required to accurately describe the flow field.

2.2 Role of wall reactions: the Peclet number

One question that is often raised is whether wall reactions play an important role given that the reactors are constructed from silicon carbide. Of course, one must work to eliminate this possibility by careful experimentation, however it appears that the nature of the flow field minimizes the effect of any wall reactions.

One can show that the characteristic time for flow in the reactor or residence time is $\tau_{res} = L/u$ and the characteristic time for radial diffusion is $\tau_{diff} = R^2/D$. As an example, consider the diffusion of acetaldehyde. Fig. 2.1 compares the characteristic times for acetaldehyde in helium and argon carrier gases as a function of temperature. As can be seen, except at the highest temperatures, the residence time in the reactor is less than the characteristic radial diffusion times. (Here the residence times are obtained from CFD solutions as described in Chapter 3.)

The ratio of these two times is the Peclet Number:

$$Pe = \frac{\tau_{res}}{\tau_{diff}} = \frac{Lu}{D} \tag{2.13}$$

In the limit of small Peclet numbers the residence time is too short for diffusion to take place. In this case, one can expect that only the flow directly adjacent to the wall would be affected by

Figure 2.1: Comparison of residence and diffusion times for acetaldehyde in helium and argon

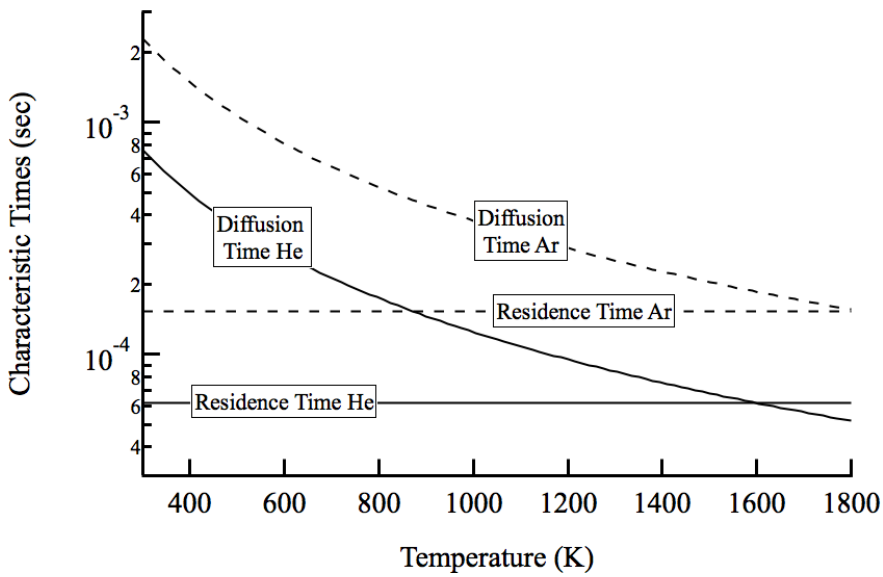

wall reactions. Conversely for large Peclet numbers, the flow is diffusion dominated. This means that the flow is well mixed in the radial direction. Thus, the wall reaction would have a greater effect on the body of the flow. However, the situation is more complex in that the heterogeneous and homogeneous chemistry can play a role. For example, if the surface chemistry were to produce light radicals, they would diffuse faster and could drive gas phase reactions in the body of the flow. Again, careful experimental calibration and simulation must determine the importance of heterogeneous reactions.

2.3 Role of secondary radical reactions

An advantage of a supersonic high temperature micro-reactor over more conventional pyrolysis tubes is the short residence time, which helps to minimize rapid, secondary radical reactions. Many radicals react with little or no activation energy and radical/radical reactions are consequently very fast. Radical/radical reactions can have second-order rate constants, k_{II}, on the order of 2×10^{-10} cm^3/sec. For radical/radical reactions, such as CH_3 + HCO $\rightarrow$ CH_4 + CO, the destruction rate for the radicals is quadratic in [R], the radical concentration. The half-life of the radicals, $\tau_{1/2}$, can be estimated as

$$\tau_{1/2} = \frac{1}{2k_{II}[R]_0} \tag{2.14}$$

If the partial pressure of the radical in the micro-reactor is roughly 1 mTorr, then $\tau_{1/2}$ is about 200 μsec at a temperature of 1200 K. Consequently, a transit time of 100 μsec (or less) through the micro-reactor would minimize many interfering secondary radical reactions. As we shall see, because of the variation in temperature and pressure within the reactor, the effective residence time for reaction is likely to be a few tenths of microseconds. Therefore, if the initial reactant concentration is small enough, secondary reactions are unimportant. Of course, in practice there is a tradeoff between signal and minimizing secondary reactions.

2.4 Rarefied flow in the vacuum chamber

Upon exiting the reactor, the flow enters a first vacuum chamber at about $10^{-6} - 10^{-4}$ torr. Therefore, an underexpanded jet is formed. In the continuum limit the centerline flow is isentropic until a strong shock wave (Mach disk) is formed (see Fig. 1.5). However, in our case, the vacuum chamber is always held at very low pressure so that the flow rapidly transitions into a free molecular, or collisionless, flow [4]. When using matrix isolation diagnostics the flow impinges directly onto the matrix window in the first vacuum chamber. For PIMS, a skimmer separates the first chamber from the time-of-flight spectrometer that is further pumped to 10^{-7} torr. This type of flow was studied extensively in the 1960's and 1970's. A review of the literature on underexpanded jets and molecular beams relating to mass spectrometry is given by Miller [45].

We first assume that the expansion will follow an isentropic process and remain on a continuum at least for a certain distance. Then in the continuum region of the expansion, the simple one-dimensional isentropic flow relations [60] give the following:

$$\left(\frac{T}{T_0}\right) = \left(1 + \frac{\gamma - 1}{2} M^2\right)^{-1} \tag{2.15}$$

$$\left(\frac{P}{P_0}\right) = \left(1 + \frac{\gamma - 1}{2} M^2\right)^{-\frac{\gamma}{\gamma-1}} \tag{2.16}$$

$$\left(\frac{n}{n_0}\right) = \left(1 + \frac{\gamma - 1}{2} M^2\right)^{-\frac{1}{\gamma-1}} \tag{2.17}$$

where M is the Mach number defined as

$$M \equiv \frac{V}{a} = \frac{V}{\sqrt{\gamma R T}} \tag{2.18}$$

and a is the local speed of sound. P_0 and T_0 are the total or stagnation pressure and temperature, which are the values that P and T would take if the flow were isentropically decelerated to zero velocity. For a sharp-edged orifice, these would be P and T in the upstream chamber. However, in our case, we can only estimate their values using the isentropic relations.

By applying the First Law of Thermodynamics where h_0 is the total enthalpy

$$h_0 = h + \frac{V^2}{2} \tag{2.19}$$

and introducing the specific heat at constant pressure, one can show that:

$$V = \sqrt{\frac{2R}{W}\left(\frac{\gamma}{\gamma - 1}\right)(T_0 - T)} \tag{2.20}$$

If $T_0 \gg T$, then the velocity approaches an asymptotic limit of

$$V_\infty = \sqrt{\frac{2R}{W}\left(\frac{\gamma}{\gamma - 1}\right)T_0} \tag{2.21}$$

Exploiting these relationships requires that the Mach number be known as a function of distance from the reactor exit. We use a correlation from Anderson [3],

$$M = 1.0 + A\left(\frac{x}{d}\right)^2 + B\left(\frac{x}{d}\right)^3 \tag{2.22}$$

for $0 > \left(\frac{x}{d}\right) > 1.0$, and

$$M = \left(\frac{x}{d}\right)^{\gamma-1}\left[C_1 + \frac{C_2}{\left(\frac{x}{d}\right)} + \frac{C_2}{\left(\frac{x}{d}\right)}^2 + \frac{C_3}{\left(\frac{x}{d}\right)}^3\right] \tag{2.23}$$

for $\left(\frac{x}{d}\right) > 0.5$. The empirical constants are given in Miller [45]. Note that the Mach number is not a function of the thermodynamic state.

The above relations are valid for the continuum flow upstream of the Mach disk. An empirical relation for the location of the Mach disk given by Bier and Schmidt [9] is:

$$\frac{x_M}{d} \cong 0.67\left(\frac{P_0}{P_b}\right)^{1/2} \tag{2.24}$$

where P_b is the pressure in the vacuum chamber into which the expansion flows. This continuously expanding region is sometimes also referred to as the "zone of silence". For the typical pressure ratios seen in PIMS machines (10^4-10^6), this expression predicts a distance of 10 cm which is far from the flow exit. In fact, for a low enough P_b it is unlikely that a Mach disk forms as the transition to a

free molecular flow takes place at distances much closer to the reactor exit. Thus, an important issue is whether these continuum relations properly describe the flow field as it undergoes the transition to free molecular flow. It is well known, for example, that once the collision frequency drops below a certain value, both translational and internal modes are unable to exchange energy and the flow "freezes". Therefore, the isentropic expression for temperature will break down. Fig. 2.2 from Miller [45] illustrates this situation including the results of numerical solutions to translational energy rate equations for the kinetic energy both parallel and perpendicular to the flow axis. As can be seen, the parallel temperature freezes first, while the perpendicular temperature takes a longer distance to freeze.

Figure 2.2: Illustration of the supersonic expansion and skimmer sampling (adapted from [45])

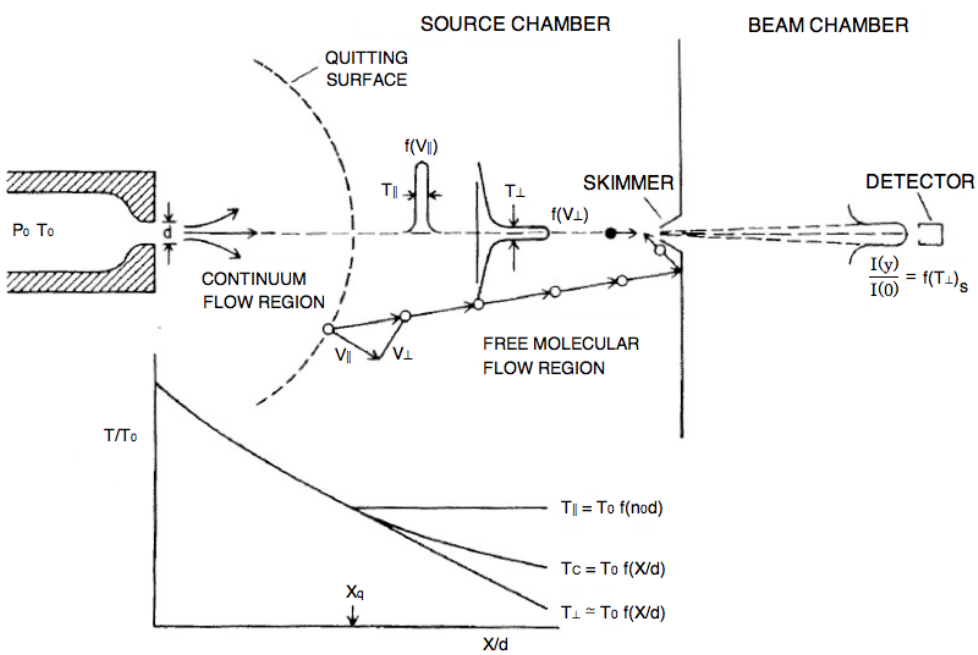

While the transition to a free molecular flow takes place over a finite distance in reality, for simple characterization, many authors have proposed a "quitting surface" model, sometimes also referred to as the "last collision surface" [7] based on a Knudsen or collision number analysis. Miller [45] recommends using the following correlation for the limiting parallel speed ratio based on Beijerinck and Verster's [7] results:

$$S_{\parallel,\infty} = \sqrt{\gamma/2} M_{\parallel,\infty} = A \left[\sqrt{2} n_0 d \left(\frac{53 C_6}{k T_0} \right)^{1/3} \right]^B = A \left[K n_0{}^{-1} \right]^B \tag{2.25}$$

Here $A = 0.527$ and $B = 0.545$ when monatomic gas is used.

For the purposes of this discussion, the most important consequence is that all reactions are rapidly quenched. As an example, the expansion of a helium gas from a T_{wall} =1500 K reactor is studied. Fig. 2.3 shows a comparison between the temperature calculated using a DSMC simulation and the empirical expressions in Miller [45]. The starting temperature at $x = 0$ is about 1200 K due to the cooling effect of gas acceleration near the reactor end. While the simulated value does not exactly agree with the isentropic calculation, both show that the temperature drops rapidly downstream, roughly by half within one reactor diameter. This temperature quenching implies that any chemical reaction can only take place within the reactor and will quickly cease in the expansion.

Combining Eqn. 2.25 with the relationship between the Mach number and the distance results in the quitting surface location. In the example discussed below $M_{\parallel,\infty} = 19.96$ and the quitting surface is located 1.53 cm downstream of the tube exit. Beijerinck and Verster (1981) [7] actually recommend a correlation based on the parameter

$$\Xi = 3.189 \left(\frac{\gamma - 1}{\gamma} \right)^{1/2} z_{ref} n_0 (C_6/k t_0)^{1/3} \tag{2.26}$$

Ξ is related to the Kndusen number and z_{ref} is a scaling length which for argon is 0.403 d. C_6 is the long range van der Waals attractive potential parameter. The quitting distance correlation is:

$$z_F = z_{ref} (1.875 \Xi / N_F)^{3/(\gamma+2)} \tag{2.27}$$

$$x_q \approx d \left(\frac{M_\infty}{C_1} \right)^{1/(\gamma-1)} \tag{2.28}$$

where N_F is a collision number that Beijerinck and Verster [7] set to 2.14. For the same example of the helium gas from a T_{wall} =1500 K reactor, this correlation results in a quitting surface located

Figure 2.3: Temperature as a function of downstream distance from reactor exit

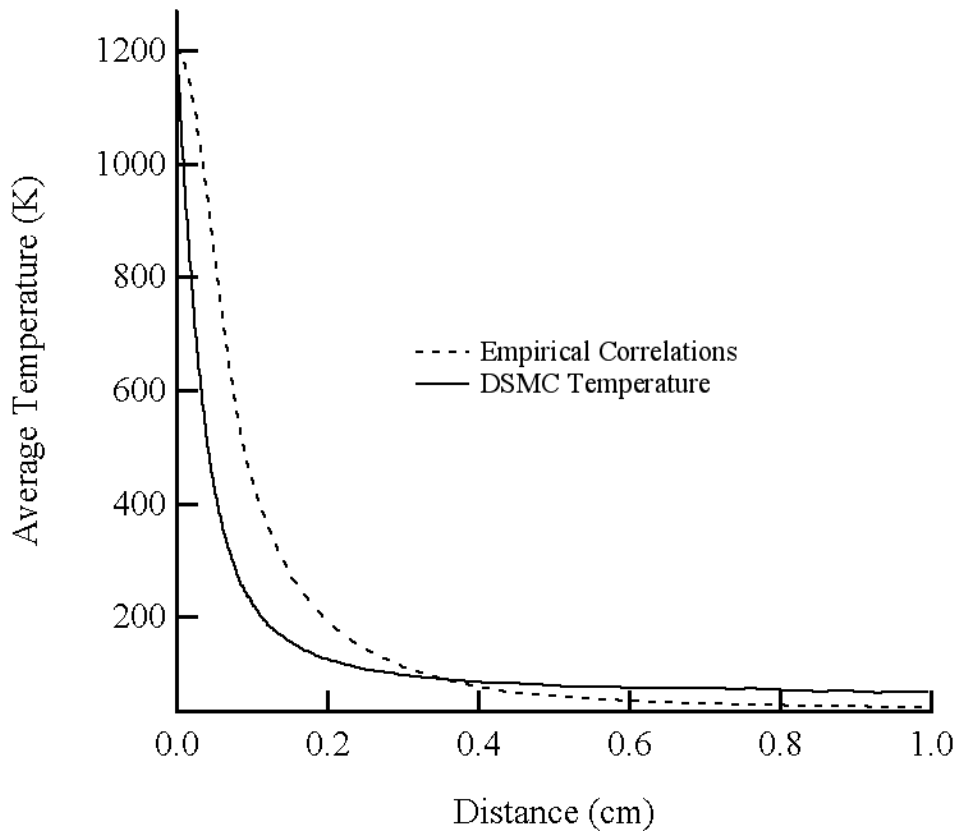

about 1.88 cm downstream of the tube exit.

Fig. 2.2 illustrates what is known about the centerline velocity distributions downstream of the quitting surface. The parallel temperature distribution remains Gaussian-like with constant width (i.e. temperature). However, the perpendicular distribution displays the characteristics of a double Gaussian. The narrow peak represents the collisionless velocity distribution. This portion of the distribution continues to narrow with downstream distance, falling like $1/x^2$. This is primarily a geometric effect as the flow at this point behaves as if it originates from a point source. The broader base is due to collisions between molecules traveling in the axial direction that transfer energy orthogonal to the beam. This effect has been studied by Beijerinck and Verster [7] who referred to it as a "blistering" of the distribution function. In Fig. 2.2, the curve labeled T_c represents an average temperature for the total perpendicular distribution, while $T_\perp$ represents the narrow collisionless core. They estimate that the broad base is 5 to 10 times wider than the narrow core. To be conservative, we use the larger value.

Figure 2.4: Knudsen numbers as a function of downstream distance

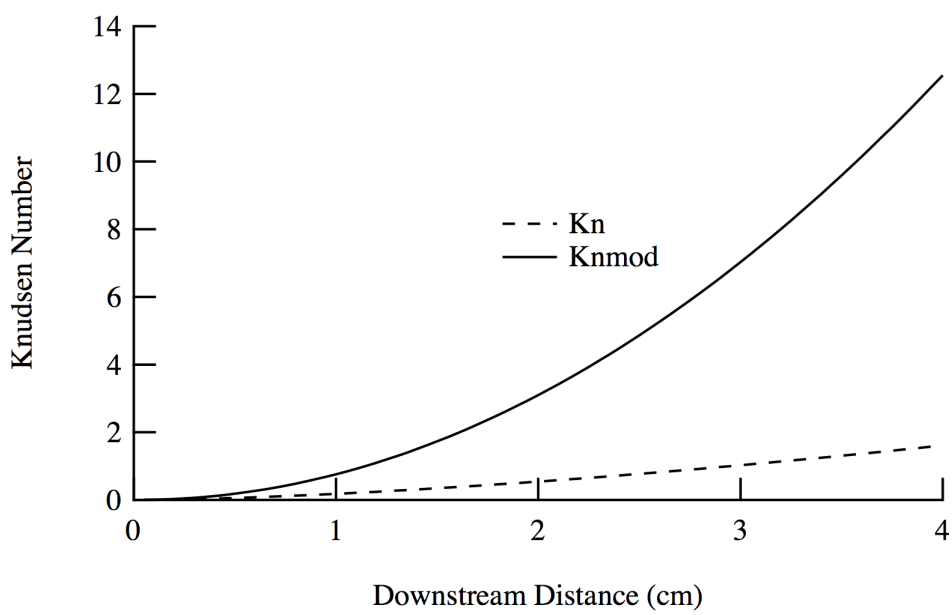

Using the above facts, we can then estimate the centerline expansion/beam properties as a function of downstream distance. As mentioned above, the collisionless perpendicular temperature

falls like $1/x^2$. Bird [12] carried out DSMC studies of the behavior of skimmers in sampling supersonic beams. He showed that for sufficiently large values of a modified Knudsen number (Kn based on T_0 and the skimmer diameter), that the skimmer has little effect on the upstream flow and that it will behave in the idealized way. That is, the exit flow rate will equal the flow rate that strikes the entry port with no loss due to molecule-molecule or molecule-wall collisions and the velocity distribution of the incoming molecules will not be disturbed. A reasonable lower limit to the modified Knudsen number is 5-8 depending on the collision cross sections. Since the density downstream of the quitting surface also drops by $1/x^2$ [12] the Knudsen number can be easily calculated. Furthermore, the centerline beam property relations are unaffected by the skimmer. Fig. 2.4 shows the distribution of the local and modified Knudsen numbers [12]. For example, a skimmer placed at a modified Knudsen number of 5 would be located about 2.5 cm downstream of the nozzle exit. Clearly larger distances will suffer no skimmer collisional effects. Starting at the quitting surface, and assuming the skimmer is located sufficiently far downstream, the temperature and centerline number density can be estimated by the analytical solutions.

Chapter 3

Reactor Simulations with CFD Method

In the CFD simulations we solve the 2D axisymmetric Navier-Stokes equations along with the heat equation for the reactor walls. The geometry and mesh are shown in Fig. 3.1. We include part of the upstream feed tubing, the connecting transition section, and the reactor. Simulations have been performed using helium or argon as the carrier gases, and the properties of these two gases along with those of the wall material, SiC, are given in Appendix A.

To complete the solution, appropriate boundary conditions must be provided. These include the outer wall temperature between the electrodes, the mass flow rate, the inlet or outlet pressure, and some statement regarding the boundary conditions for velocity and temperature between the gas and solid walls such as the no-slip condition or a slip relation. (When solving the species conservation equation we specify a zero flux at the walls.) When conducting experiments, we specify the volumetric flow rate and the outer wall temperature of the reactor. As the pressure in the downstream plenum is very low, the flow will choke at the exit. The inlet pressure is adjusted to accommodate the flow rate. The downstream pressure boundary condition requires special care. Because of the low pressure in the plenum, the continuum flow condition is likely to be violated. Therefore, we specify a larger pressure than experimentally observed, but one low enough to ensure that the flow chokes at the tube exit and that the bulk of the flow at the exit is in or close to continuum. (One can test this proposition by calculating and monitoring the local Knudsen number based on the tube diameter.) Finally, for the walls we also specify an outer radiation boundary condition since the tube is mounted in the plenum and thus there are only radiative heat

losses.

The conservation equations are second order in space. Thus, one can specify the inlet and outlet pressures or the mass flow rate and one pressure but not all three. This provides a form of validation for the simulations. We specify the pressures and then iterate on the inlet pressure to match the measured mass flow rate. If the inlet pressure obtained from the simulation matches the experimental value that is a good indication that the solution is valid.

As mentioned above, if the local Knudsen number near the wall is sufficiently large, then velocity and/or temperature slip can occur. In our simulations, we apply the slip conditions using Maxwell's model [44]:

$$\Delta u = \left(\frac{2-\alpha_v}{\alpha_v}\right) Kn \frac{\partial u}{\partial n} \tag{3.1}$$

$$\Delta T = 2\left(\frac{2-\alpha_T}{\alpha_T}\right) Kn \frac{\partial T}{\partial n} \tag{3.2}$$

Here, α_v and α_T stand for the momentum and thermal accommodation coefficients respectively, which are determined empirically [37, 42, 59]. In the results presented here α_v was fixed at 0.5 and α_T used for helium are altered for different cases as listed in Table 3.1. The local Knudsen number for Maxwell's model is computed based on the half cell size of the volume element next to the wall, while the mean free path is obtained as:

$$\lambda = \frac{k_B T}{\sqrt{2}\pi\sigma^2 p} \tag{3.3}$$

where T and p are the cell center gas temperature and pressure and σ is the molecular diameter of the carrier gas. (Note that the Knudsen number based on the computation cell size will be much larger than that based on the tube diameter.) We have observed that at room temperature, the flow is entirely in the continuum domain and the continuum boundary conditions apply. However, at the higher wall temperatures there are noticeable discrepancies if the slip is not accounted for.

To explore the effect of operating conditions and carrier gas on the flow field we have carried

Figure 3.1: Modeled geometry (CFD models half height)

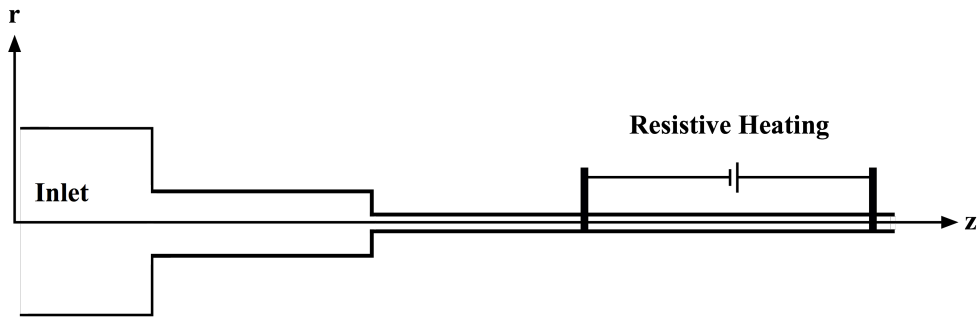

Table 3.1: Thermal accommodation coefficients of helium for different T_{wall}

	1300K	1400K	1500K	1600K
α_T	0.03	0.032	0.055	0.063

Table 3.2: Reactors for parametric study

	Total length	Diameter	Heating length
Reactor #1	2.5 cm	0.66 mm	1.5 cm
Reactor #2	2.5 cm	1.00 mm	1.5 cm
Reactor #3	3.5 cm	1.00 mm	2.0 cm

out a series of simulations by varying carrier gas, wall temperature, volumetric flow rate, and reactor diameter and length. The various geometry combinations are shown in Table 3.2.

3.1 Impact of carrier gas

We start by comparing the flow fields using different carrier gases, i.e. helium and argon. For this comparison we set the volumetric flow rate at 280 sccm. As is commonly the case, the flow rate of an experiment involving a high vacuum is limited by pumping capacity, and pumps are rated in terms of volumetric flow rate. Therefore, we usually run at the pumping limit, which at the ALS is about 280 sccm.

Helium and argon are different in two respects. The first, obviously, is the difference in molecular weight of approximately a factor of ten, the consequence of which is that the mass flow rate of argon is a factor of ten greater than for helium at a fixed volumetric rate. The second major difference is that the thermal conductivity of helium is much larger than that for argon, as illustrated in Fig. A.1 of Appendix A. Their viscosities, on the other hand, are not very different, with argon's slightly larger (see Fig. A.2).

In the first examples, the wall temperature is set to 1500 K and the simulations are for the geometry of Reactor #1. Figs. 3.2a and 3.2b are plots of the centerline temperature and pressure as a function of axial distance through the reactor while the centerline velocity and Mach number are shown in Fig. 3.3.

As the flow enters the reactor section, the gas temperature begins to increase. For helium, the increase is fairly rapid, while for argon it is slower. The difference is due to their thermal conductivities and convective heat transfer rates. The gas velocity increases as a result of the

Figure 3.2: Centerline pressure and temperature distributions with $T_{wall} = 1500$K

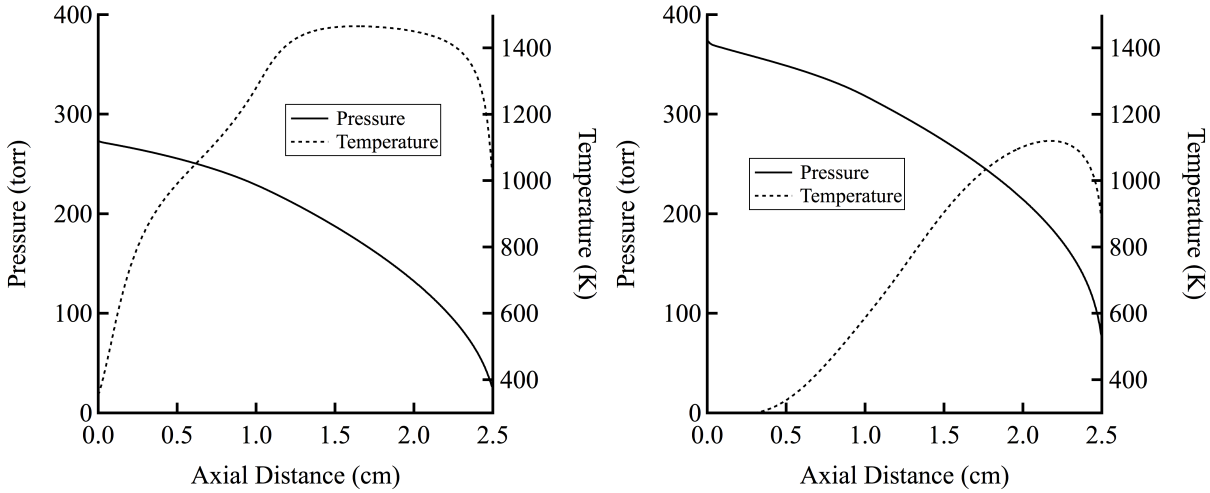

(a) helium (b) argon

Figure 3.3: Centerline velocity and Mach number distribution with $T_{wall} = 1500$K

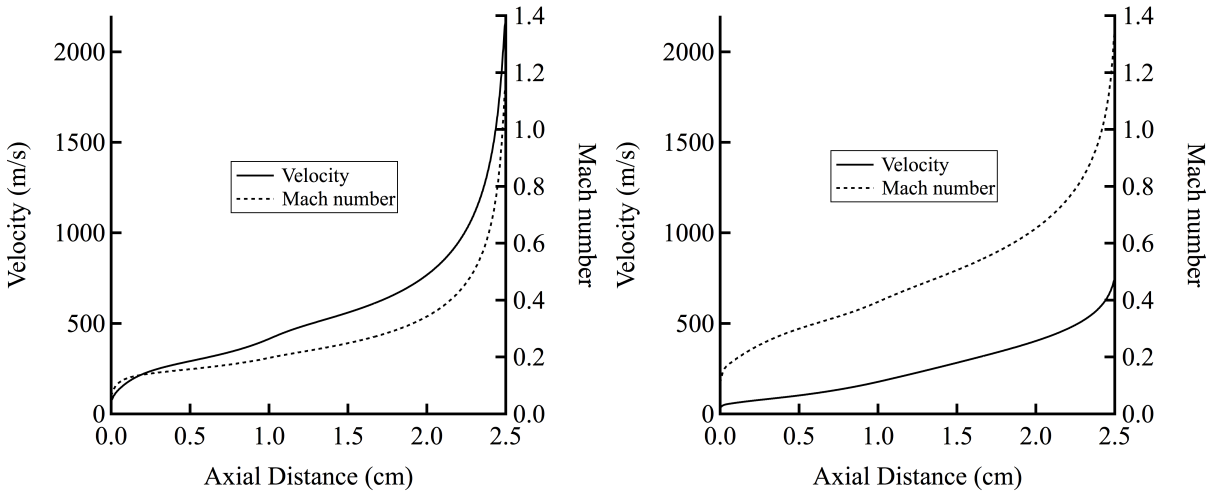

(a) helium (b) argon

density dropping due to wall heat transfer, friction, and the drop in pressure, and reaches the sonic point at the reactor exit (see Fig. 3.3). The gas pressure decreases as would be expected. For simple incompressible constant density flow, the pressure would vary linearly with distance downstream, but here we see a somewhat non-linear variation with the gradient increasing with distance as the velocity, and thus velocity gradient at the wall, increases.

Figure 3.4: Centerline Knudsen number distribution with $T_{wall} = 1500$K

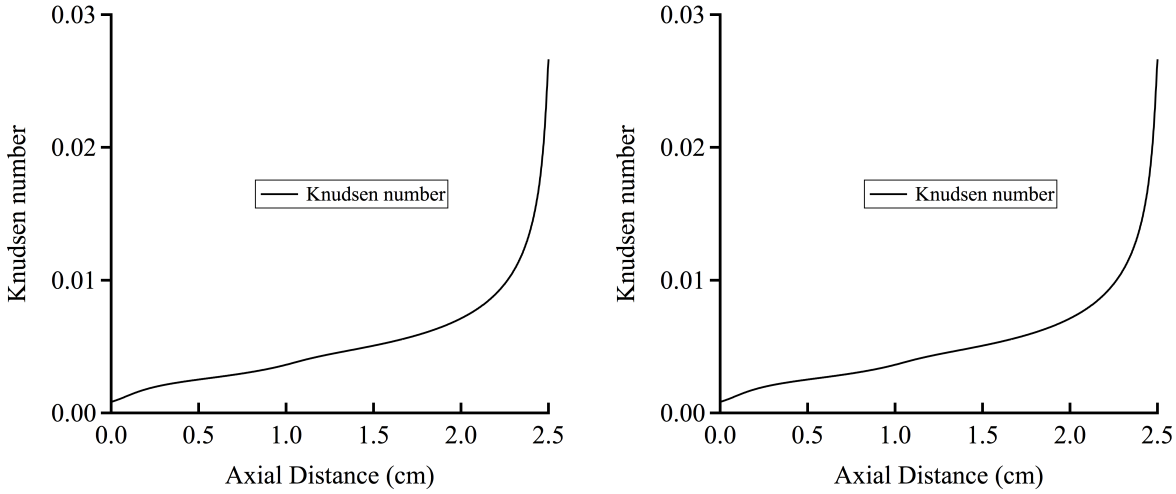

(a) helium

(b) argon

One can see from the centerline variation of the Knudsen number that it does increase sharply near the end of the reactor (see Fig. 3.4a and 3.4b), leading to the conclusion that there is likely a slip in both temperature and velocity at the wall. This was expected due to the fact that we are unable to recover the proper inlet pressure without applying the slip boundary conditions.

Radial profiles of temperature and axial velocity at increasing axial locations are shown in Fig. 3.5 and Fig. 3.6. As the flow enters the reactor at about 300 K and is heated by the walls, the centerline temperature is less than the wall temperature. Likewise, the velocity is a maximum at the centerline due to the no-slip condition holding the axial velocity adjacent to the wall at zero. Near the end of the reactor where the Knudsen number increases beyond about 0.03, a small amount of slip occurs for both temperature and velocity.

Figure 3.5: Radial velocities with T_{wall} = 1500K

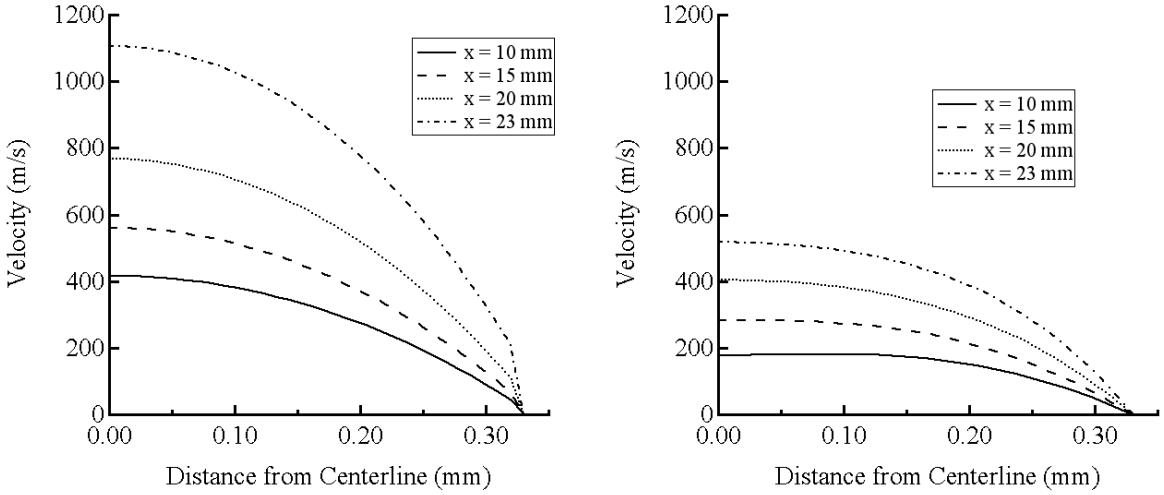

(a) helium (b) argon

Figure 3.6: Radial temperatures with T_{wall} = 1500K

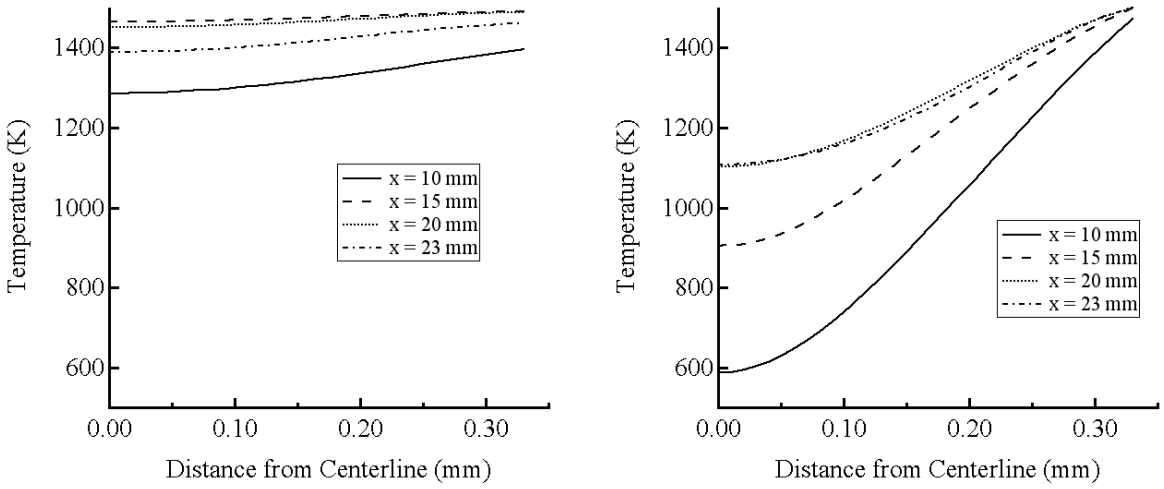

(a) helium (b) argon

3.2 Impact of wall temperature

To explore the effect of wall temperature on the flow field we have performed simulations at temperatures of 1300, 1400, 1500 and 1600 K with helium as the carrier gas. (Again the flow rate is fixed at 280 sccm and the geometry is Reactor #1.) Centerline pressure and temperature distributions are shown in Fig. 3.7, velocity in Fig. 3.8 and Mach number and Knudsen number in Fig. 3.9 and Fig. 3.10. The centerline gas temperature increases with increasing wall temperature, as would be expected. Interestingly, the centerline velocity, Mach number and Knudsen number are not a strong function of temperature because of the strong temperature dependency of the viscosity which causes the pressure drop to increase in compensation.

Figure 3.7: Centerline pressure and temperature distributions as a function of wall temperature

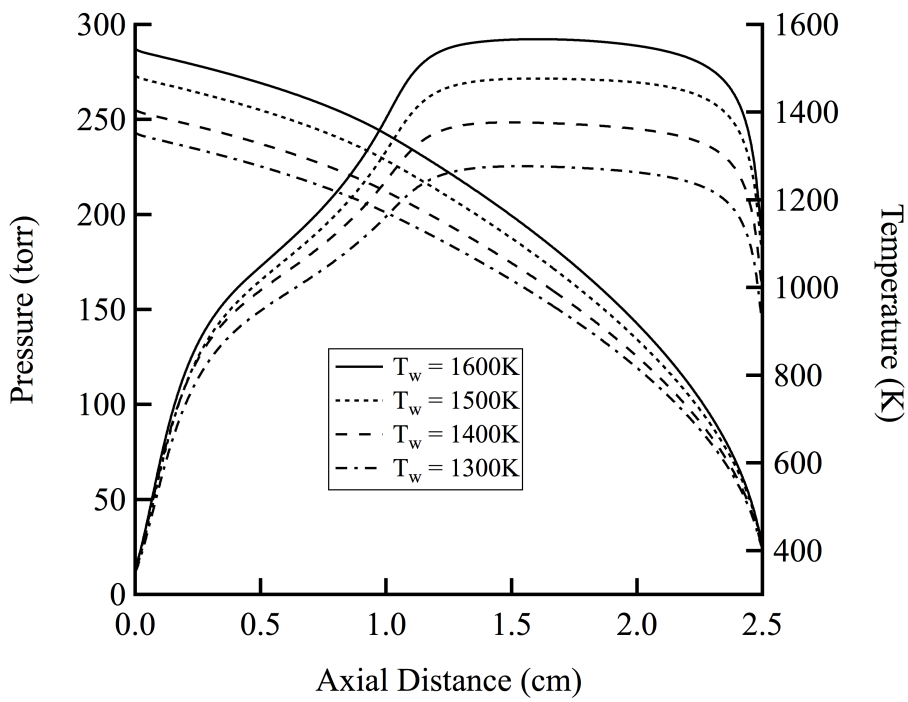

3.3 Impact of flow rate

Simulations were run (helium only) with flow rates of 100, 200, and 280 sccm at a wall temperature of 1500K. (Currently, pumping capacity limits the flow rates to values not exceeding

Figure 3.8: Centerline velocity distributions as a function of wall temperature

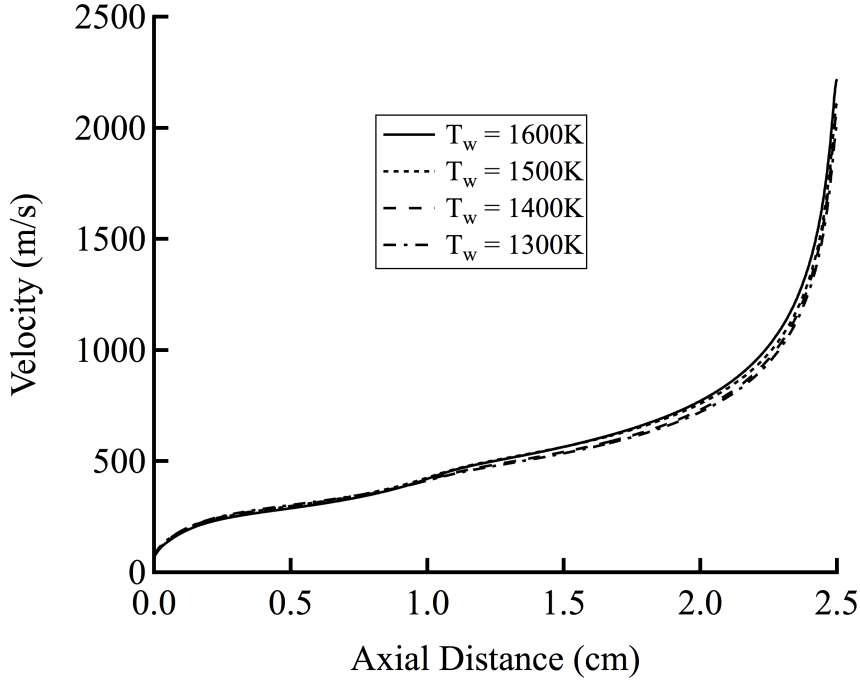

Figure 3.9: Centerline Mach number distributions as a function of wall temperature

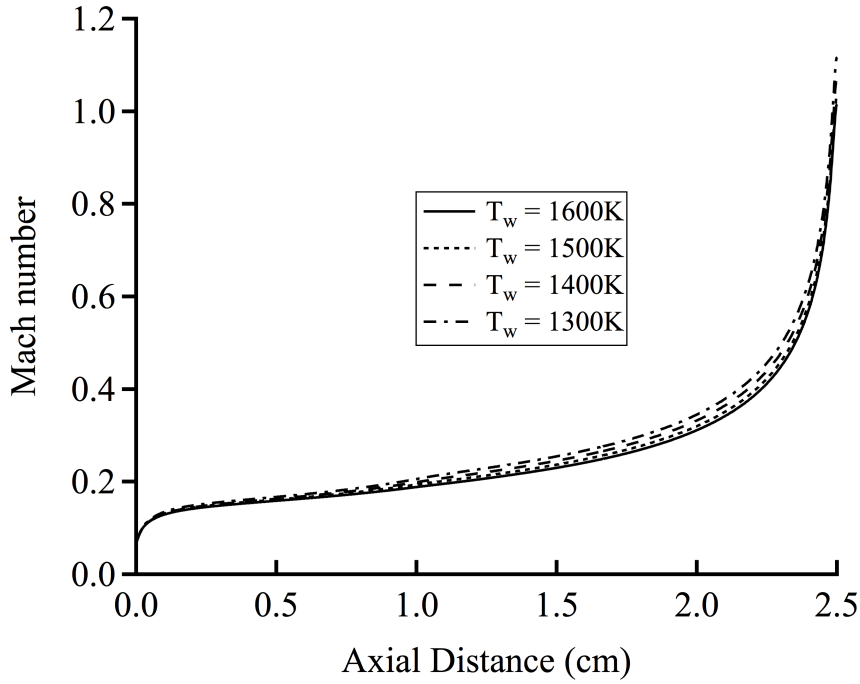

Figure 3.10: Knudsen number distributions as a function of wall temperature

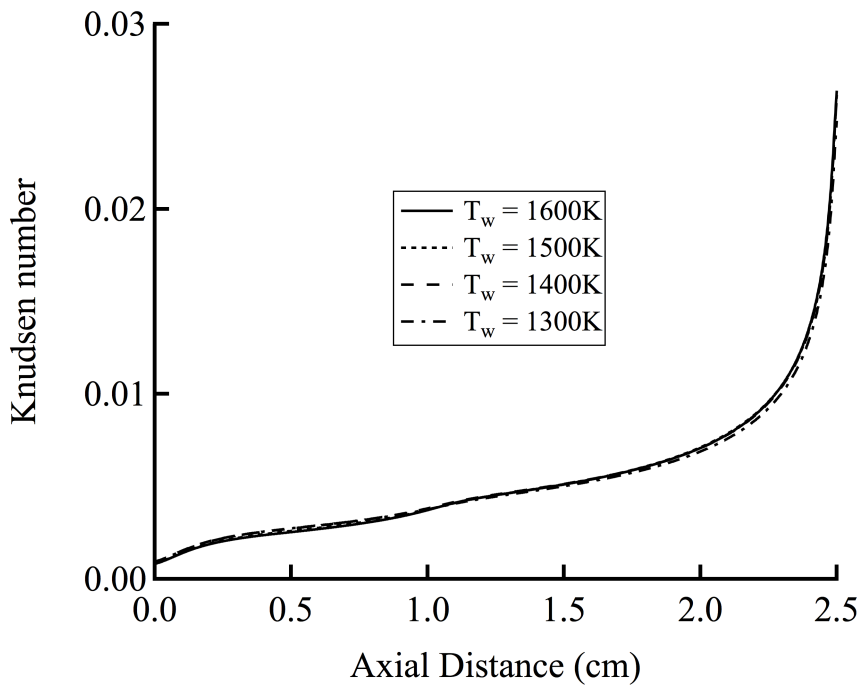

280 sccm.) The geometry is that of reactor #1. Centerline pressures and temperatures are compared in Fig. 3.11. Centerline velocities and Mach numbers are shown in Fig. 3.12 and Fig. 3.13.

Figure 3.11: Centerline pressure and temperature distributions as a function of flow rate

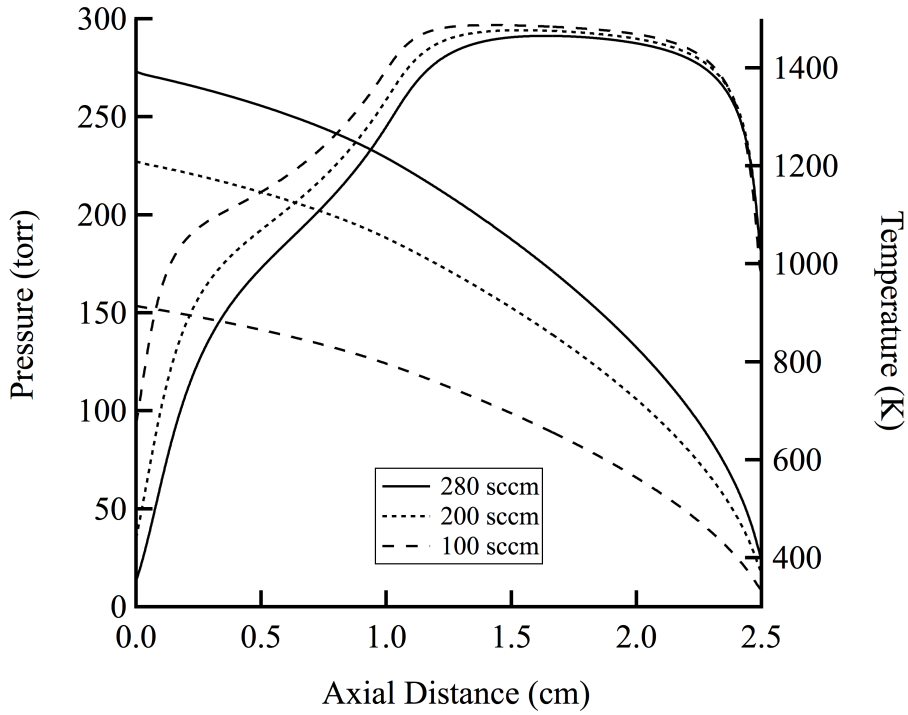

As would be expected, both the velocity and pressure drop increase with increasing flow rate. The centerline temperature grows more slowly with increasing flow rate because the thermal entry length is directly proportional to Reynolds number as shown in Eqn. 2.7. At all three flow rates the flow reaches the sonic condition near the end of the reactor. However, for the two lower flow rates the large Knudsen numbers indicate an early transition to rarefied flow. Indeed, the CFD simulation is breaking down and is less reliable for these flow rates.

3.4 Impact of reactor diameter

The effect of the reactor diameter will depend on how the particular operating conditions are selected in each case. The mass flow rate in a quasi one-dimensional flow is equal to:

Figure 3.12: Centerline velocity distributions as a function of flow rate

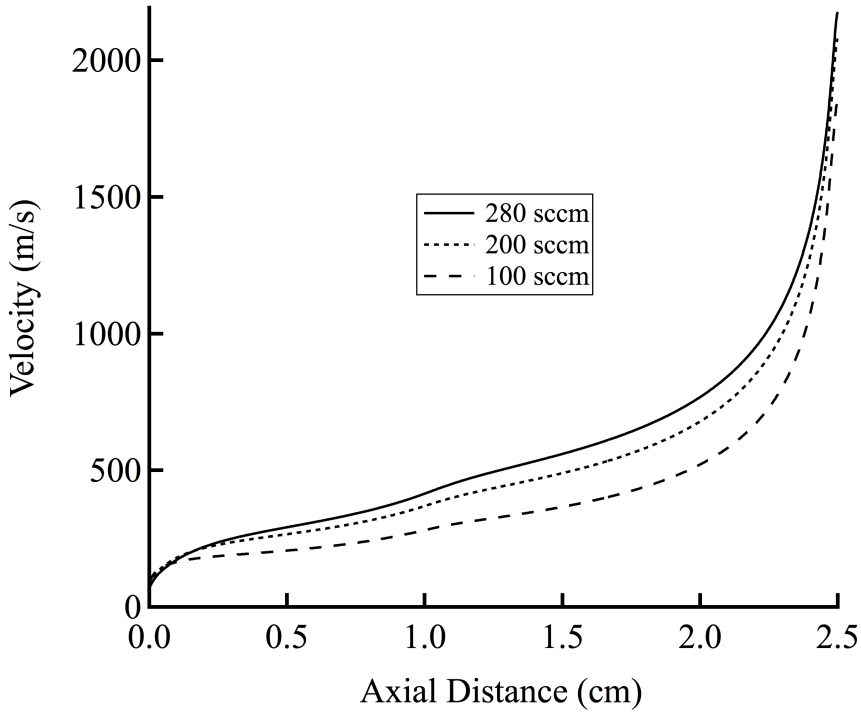

Figure 3.13: Centerline Mach number distributions as a function of flow rate

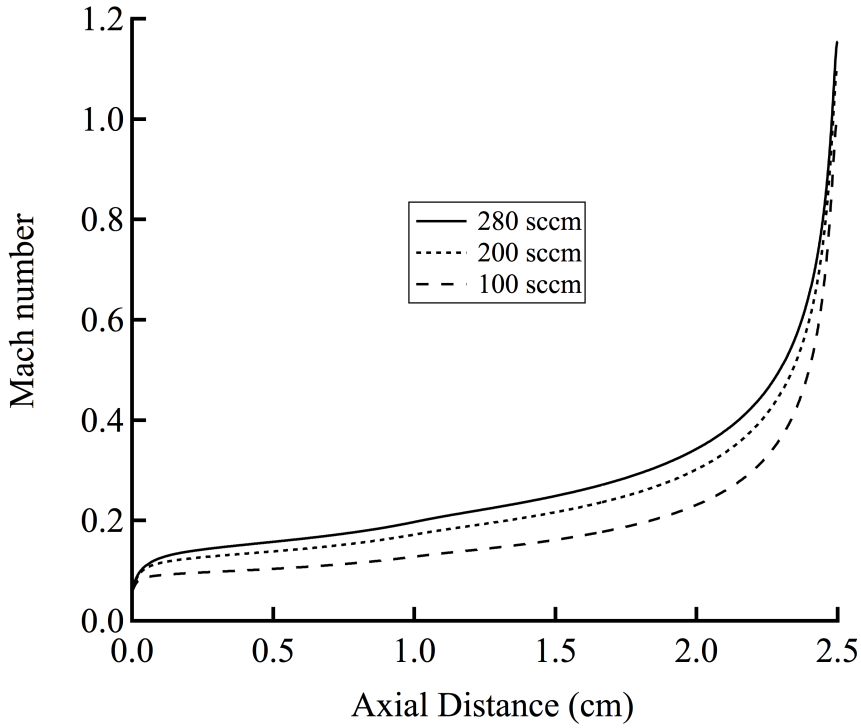

Figure 3.14: Knudsen number distributions as a function of flow rate

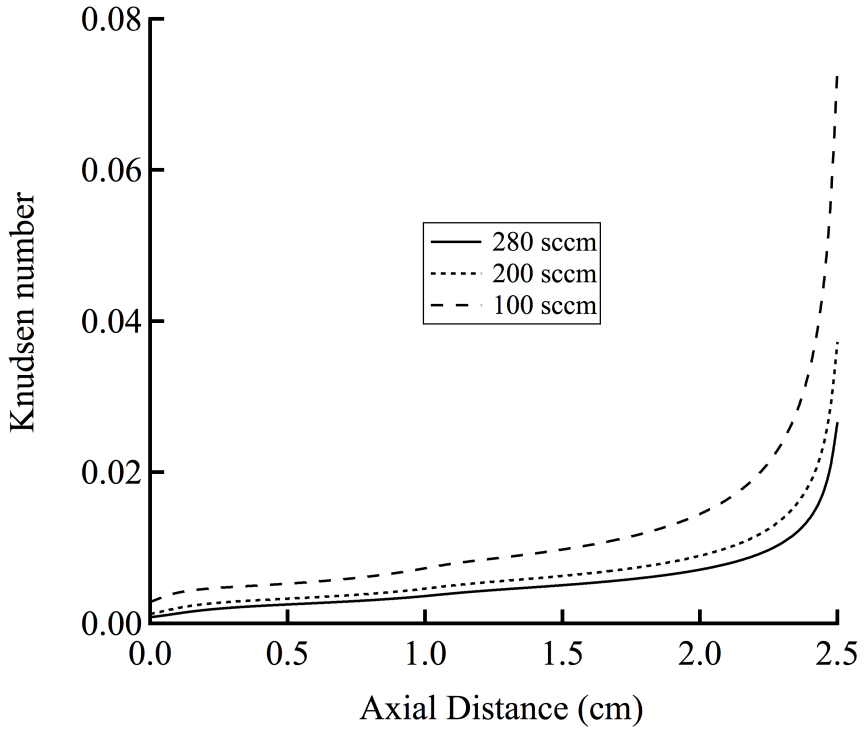

$$\dot{m} = \rho V A \tag{3.4}$$

where ρ is the mass density, V is the average velocity and A is the cross-sectional area. The entering density will be determined by the pressure and temperature, the area is given for a particular geometry, and thus the velocity will be determined by the mass flow rate. If, in working with different reactors, we hold the volumetric flow rate fixed, that means the mass flow rate is fixed. Nominally, one would think that average velocity would change inversely to the change in cross-sectional area and velocities would be higher in the smaller diameter reactor. However, because the diameter is smaller, the gradient of velocity near the wall will be greater than in the larger reactor, and the pressure drop is thus larger. Since the exit pressure of our reactor is essentially zero (actually a very small number), the increased pressure drop results in a larger inlet pressure for the smaller diameter. The consequence of this somewhat involved argument is that for a fixed mass flow rate, the average velocity is roughly independent of diameter.

To demonstrate these points we ran simulations for reactors #1 and #2. The carrier gas was helium, the flow rate 280 sccm, and the diameters 0.66 mm and 1 mm respectively. The centerline pressure and temperature distributions are shown in Fig. 3.15, the velocity in Fig. 3.16, Mach number in Fig. 3.17, and Knudsen number in Fig. 3.18. As can be seen, the pressure drop across the small diameter reactor is much larger, but the centerline velocities are approximately the same. What is different are the Knudsen number distributions. For the larger reactor the Knudsen number exceeds 0.01 much earlier, indicating that rarefaction effects are more important.

3.5 Impact of reactor length

To explore the effect of reactor length we ran simulations for reactors #2 and #3 in Table 3.2. The simulations were run for helium at 280 sccm and $T_{wall} = 1500$ K. The centerline pressure and temperature distributions are shown in Fig. 3.19, the centerline velocity, Mach number and Knudsen number in Fig. 3.20, Fig. 3.21 and Fig. 3.22 respectively.

Figure 3.15: Centerline pressure and temperature distributions with different reactor diameters

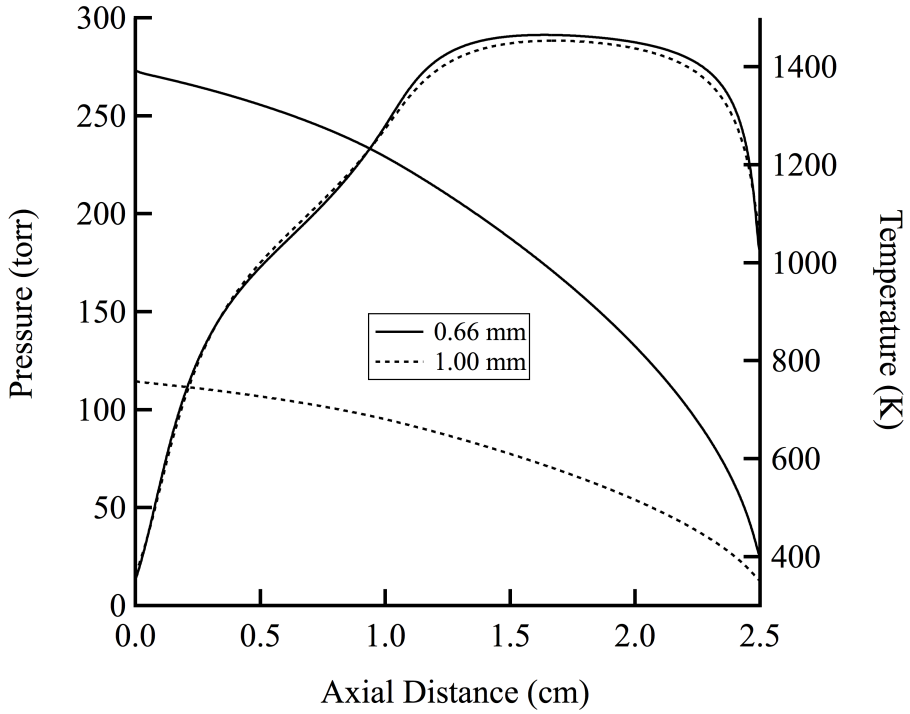

Figure 3.16: Centerline velocity distributions with different reactor diameters

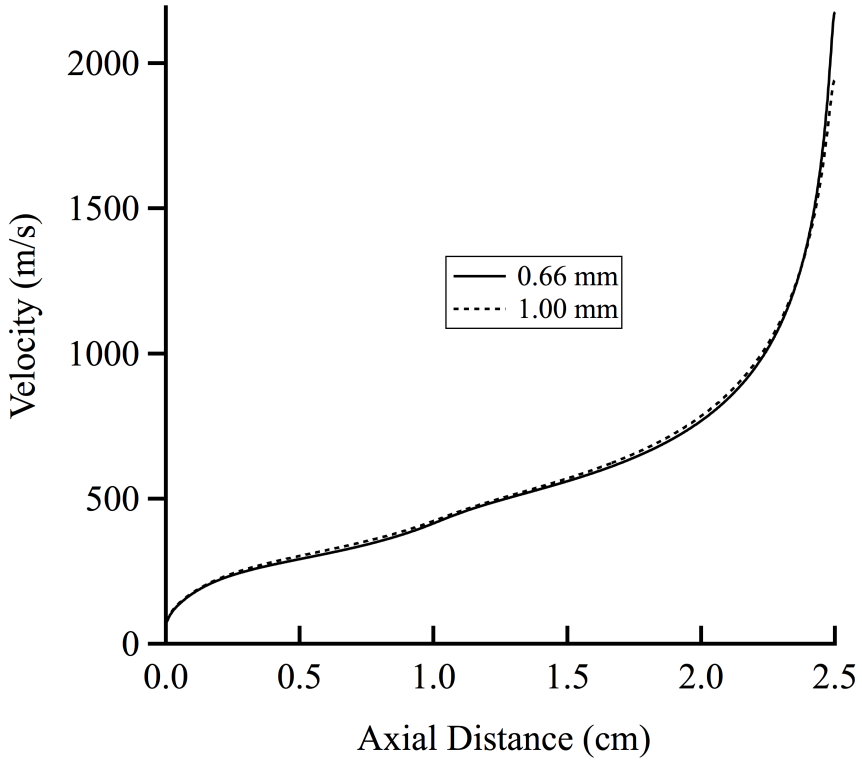

Figure 3.17: Centerline Mach number distributions with different reactor diameters

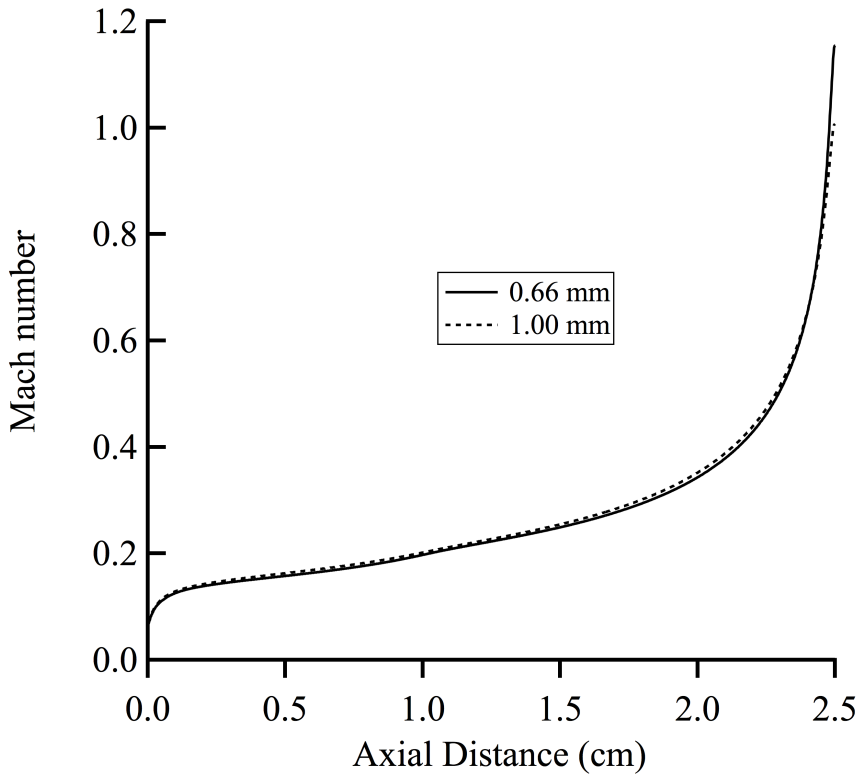

Figure 3.18: Centerline Knudsen number distributions with different reactor diameters

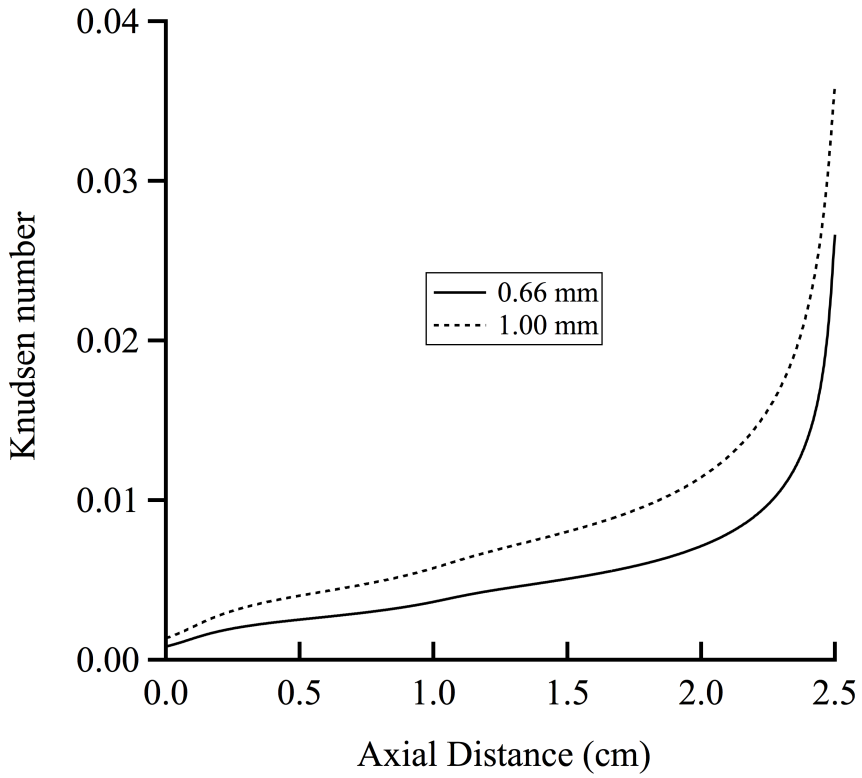

For the longer reactor, the distance between the electrodes with electrical heating is larger and located further from the inlet. Thus, while the general shape of the centerline temperature profiles are similar, there is a delay in heating, and the distance over which the temperature is at its maximum is longer. The overall pressure drop is larger as would be expected. The rise in velocity, Mach number and Knudsen number are delayed, also because the heating takes place further downstream.

Figure 3.19: Centerline pressure and temperature distributions with different reactor lengths

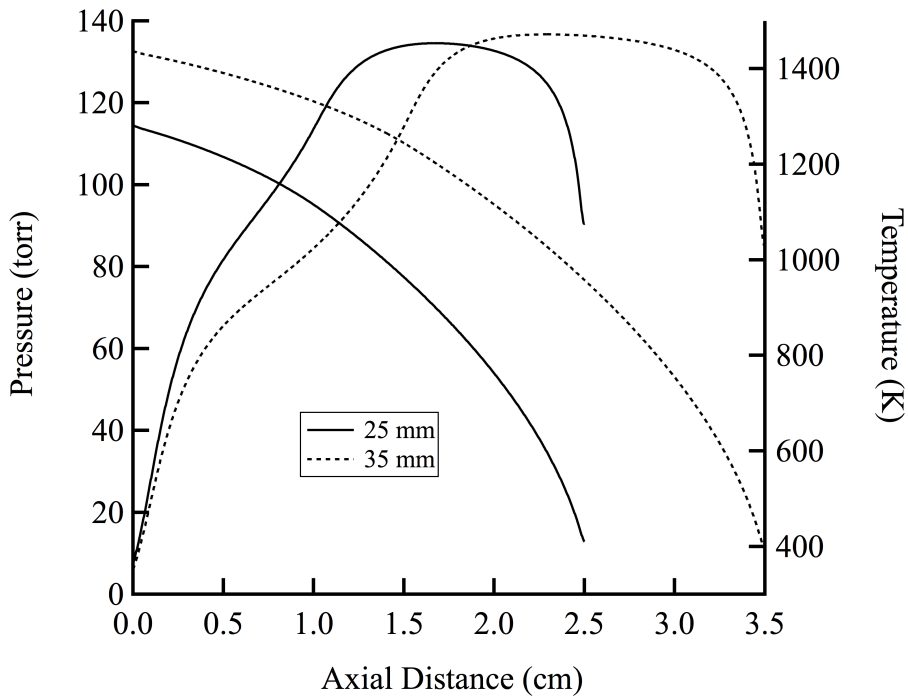

3.6 Reacting flow simulation

As one of the goals of this project, we want to extract kinetic information from the experiment. The usual way to interpret flow reactor experiments is to hypothesize a reaction mechanism and compare the experimental concentrations with slow simulations based on the mechanism, adjusting rates (as informed by the relevant literature and theory) to best match the data. We can certainly do that with our reactor, now that our simulations are validated. However, it would be especially

Figure 3.20: Centerline velocity distributions with different reactor lengths

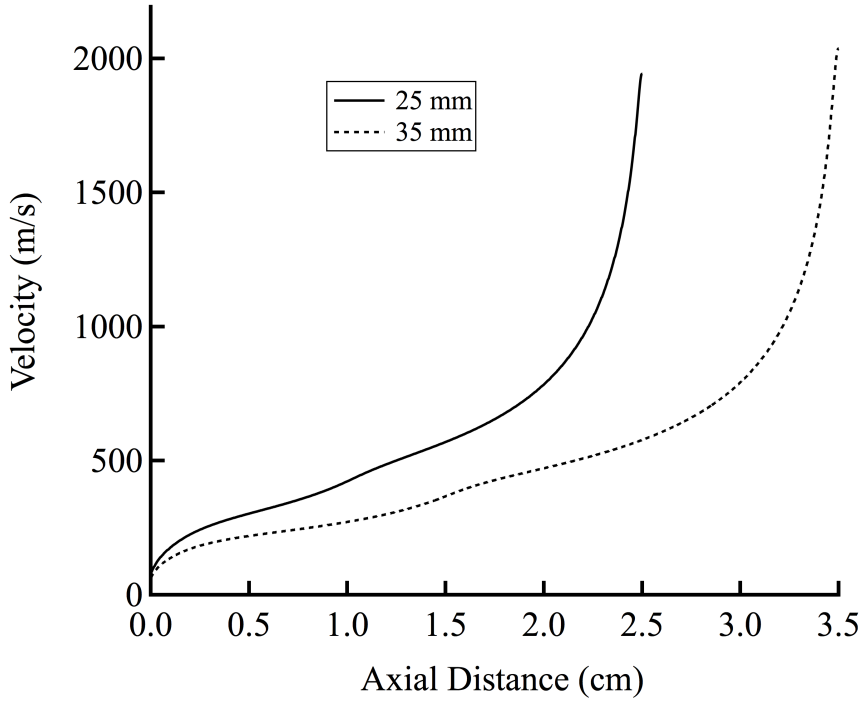

Figure 3.21: Centerline Mach number distributions with different reactor lengths

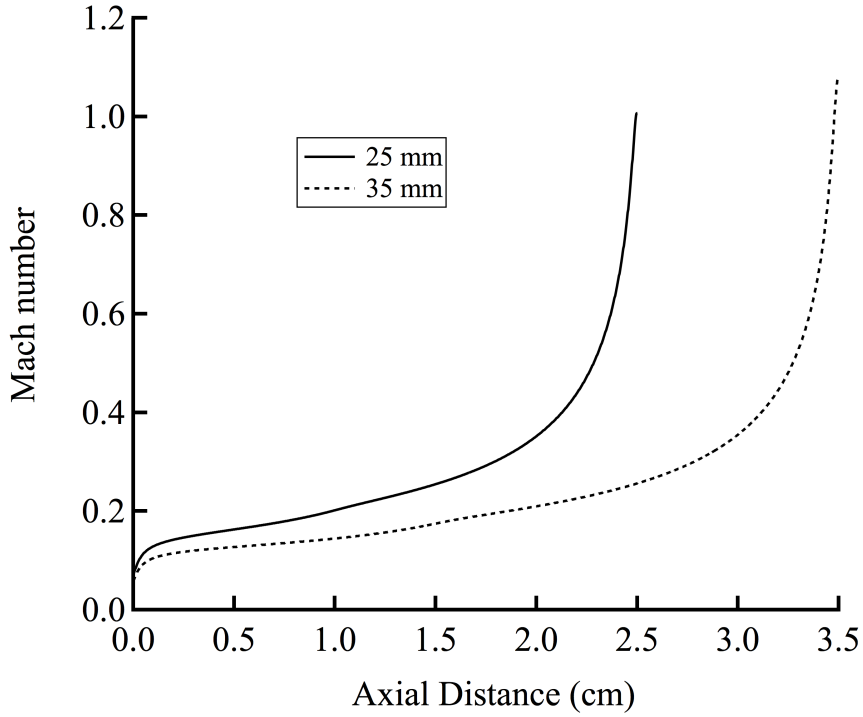

Figure 3.22: Centerline Knudsen number distributions with different reactor lengths

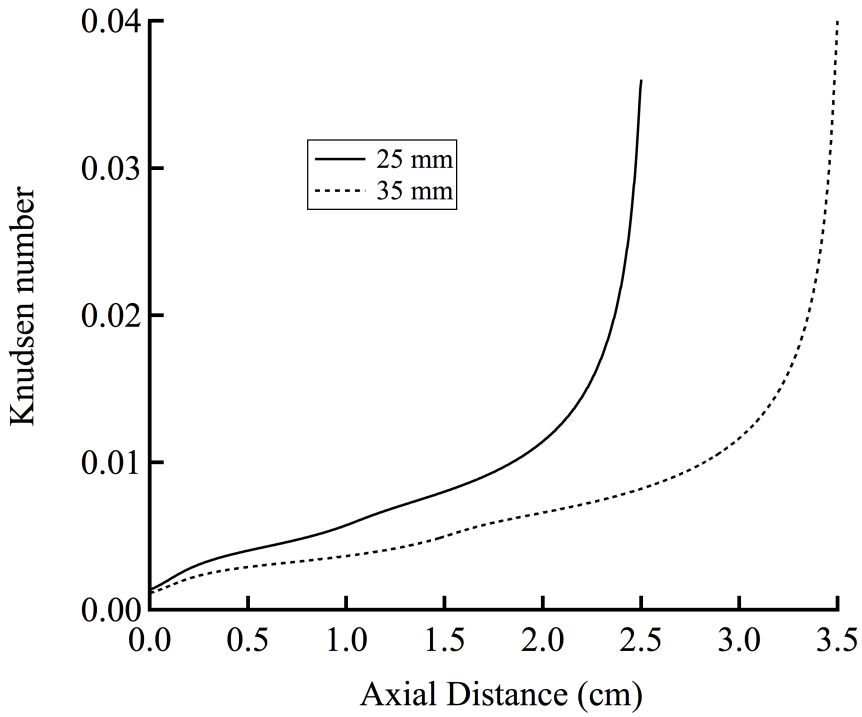

helpful if we could do so without running full CFD simulations for each case.

We start by recognizing that the simpler the reaction mechanism being studied, the easier it is to extract both mechanism and kinetic information from the data. In most cases we are studying unimolecular decomposition of large organics. For example, consider the decomposition of furan. As described by Urness et al. [70] furan dissociates via two carbene channels:

$$\text{Furan} + \text{M} \rightarrow \alpha\text{-carbene} \rightarrow \text{products} \tag{3.5}$$

$$\text{Furan} + \text{M} \rightarrow \beta\text{-carbene} \rightarrow \text{products} \tag{3.6}$$

The identity of the channels is determined by analyzing the carbene products. If there are no significant binary reactions, then the mechanism is unambiguous. To minimize binary reactions we start with very small concentrations of the reactant. To ensure this is the case we systematically lower the inlet concentration while observing the products. By also measuring the percent conversion of the reactant, we recover kinetic information.

Were the temperature and pressure in the reactor constant, using conversion data to recover rates would be straightforward. For example,

$$\frac{d[A]}{dt} = -k_{uni}[A] \tag{3.7}$$

thus,

$$\frac{[A]}{[A]_0} = -k_{uni}\tau \quad \text{or} \quad k_{uni} = -\frac{1}{\tau}\frac{[A]}{[A]_0} \tag{3.8}$$

where τ is the residence time in the reactor. However, because of the nature of the flow field, the actual species concentration equation is of the form given by Eqn. B.2. This equation has (assuming a steady flow) an additional term that describes the effect of diffusion. Furthermore, the pressure and temperature in the reactor is most definitely not uniform.

3.6.1 Cyclohexene decomposition in helium

To explore these effects, consider the thermal dissociation of cyclohexene. We use cyclohexene as a "Chemical Thermometer" [67] because its unimolecular rate is fairly well known and the

dissociation products are stable molecules that do not react further during our short residence time. (For these calculations we used RRKM rates determined using the Multiwell program.) Fig. 3.23 shows the distribution of cyclohexene mole fraction along the centerline, half the distance to the wall and along the wall as a function of downstream distance in the reactor for a 1500 K wall temperature. Because the temperature is highest along the wall, reaction proceeds more rapidly there, with reaction along the centerline proceeding more slowly. In all cases detailed examination of the simulation results show reaction along the wall proceeding at a faster rate than along the centerline. At 1500 K the decomposition of cyclohexene is fairly fast, and the cyclohexene is fully consumed by the end of the reactor. At lower temperatures this is not the case. Centerline profiles for wall temperatures of 1200, 1300, 1400 and 1500 K are plotted in Fig. 3.24.

Figure 3.23: Mole fraction of cyclohexene: T_{wall} = 1500K, 280 sccm, reactor #1, He

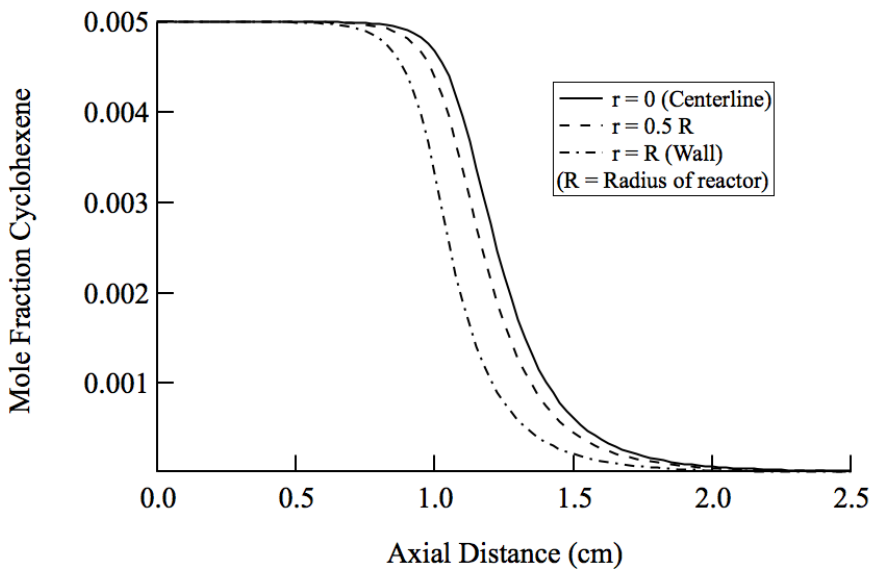

In spite of the different rates of reaction from the centerline to the wall, mole fraction profiles at the reactor exit are fairly uniform. Fig. 3.25 shows the mole fraction as a function of the radius at the end of the reactor for wall temperatures of 1200, 1300, 1400 and 1500K.

Fig. 3.26 shows the percent conversion at the exit as a function of wall temperature. The percent conversion depends roughly linearly on the wall temperature which is somewhat counter

Figure 3.24: Mole fraction of cyclohexene: T_{wall} = 1200-1500K, 280 sccm, reactor #1, He

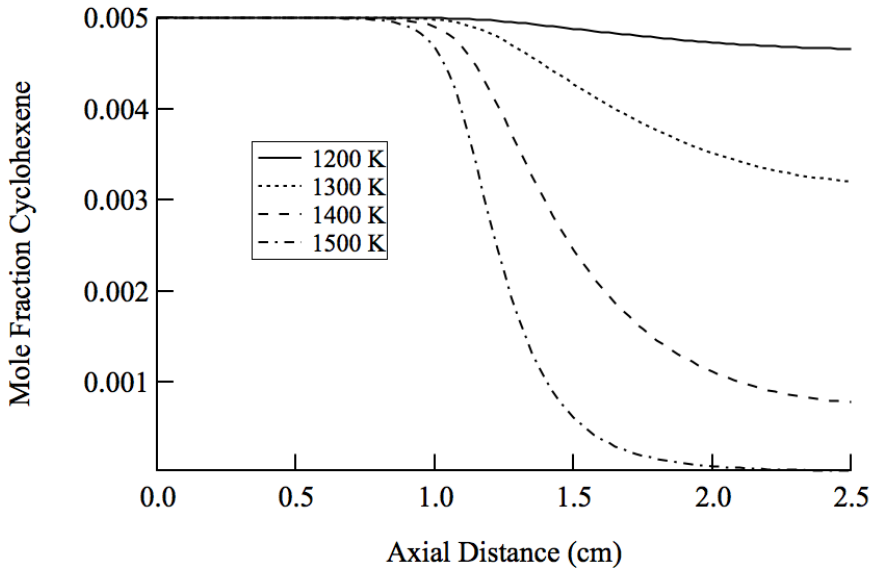

Figure 3.25: Radial mole fraction of cyclohexene at reactor exit: 280 sccm, reactor #1, He

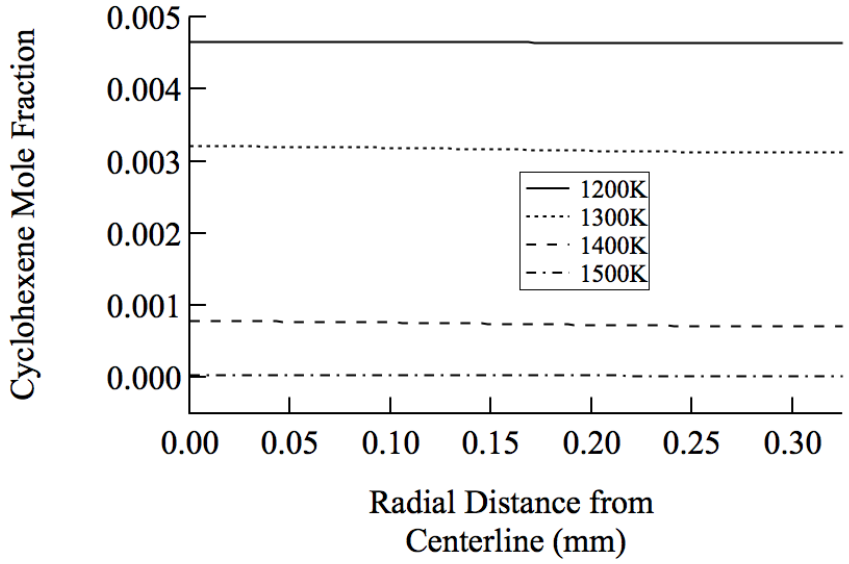

Figure 3.26: Percent conversion of cyclohexene vs. temperature: T_{wall} = 1200-1500K, 280 sccm, reactor #1, He

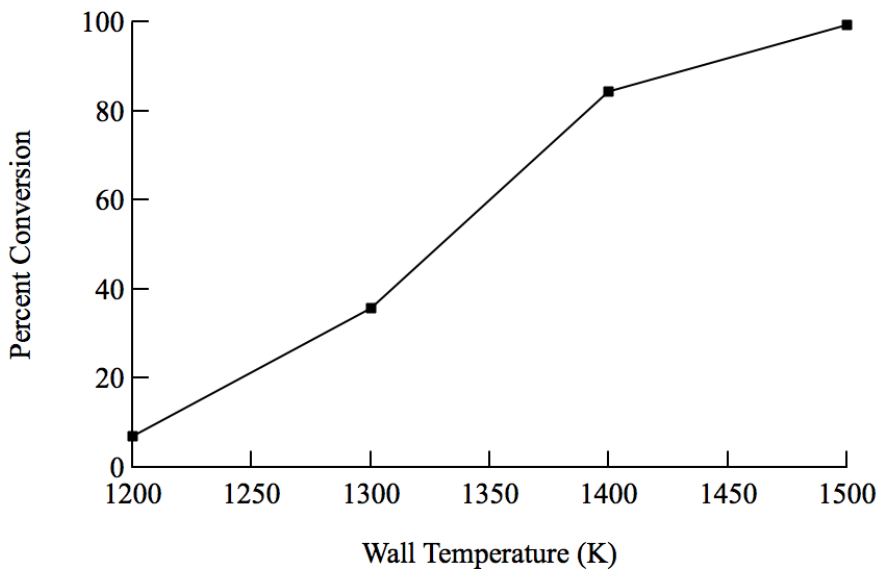

intuitive. However, as we shall see, the reality is that the higher the temperature, the less time the reaction rate (= product of k_{uni} and concentration of the reactant) is near its peak value and this softens the expected exponential effect of temperature on k_{uni}. Fig. 3.27 shows the product of pressure and temperature through the reactor. k_{uni} is a function of both temperature and pressure, and the concentration is directly proportional to pressure. While the temperature continues to rise through the reactor, the pressure declines sharply. The consequence are the reaction rates shown in Fig. 3.28.

Figure 3.27: Pressure/Temperature product vs. distance: T_{wall} = 1200-1500K, 280 sccm, reactor #1, He

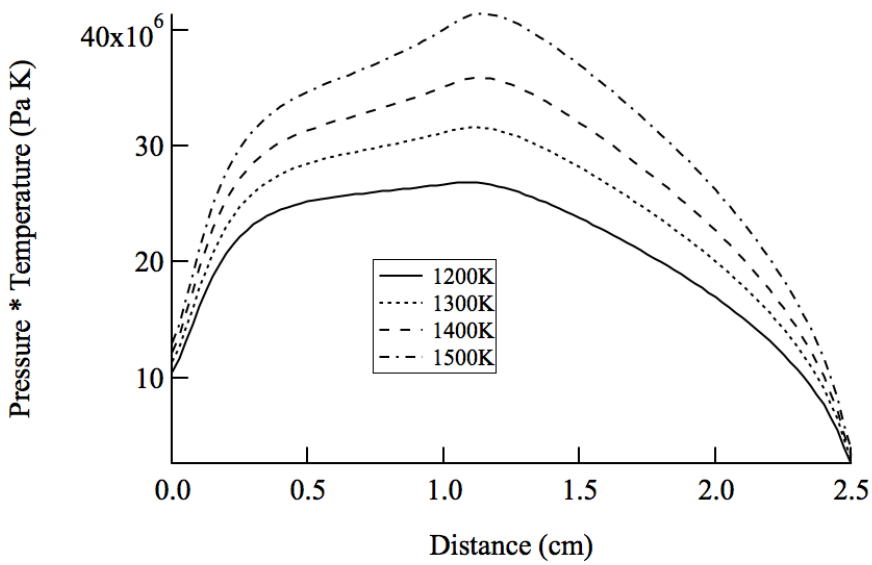

Given the above, can we find a way to simplify data analysis given the reactor operating conditions and measured conversion rate? Fig. 3.29 plots the centerline reaction rate constant as a function of axial distance for temperature ranging from 1200-1500K. Interestingly the rate constant varies somewhat slowly over the region where most of the reaction occurs. This suggests that one might be able to characterize this region with average values of the temperature and pressure and residence time. To explore this possibility, we used the cyclohexene conversion rates predicted by the full CFD simulations, extracted an average value for the rate constant using the estimated value of residence time and Eqn. 3.8, and then compared the "measured" rate constant with the RRKM

Figure 3.28: Cyclohexene decomposition rate vs. distance: T_{wall} = 1200-1500K, 280 sccm, reactor #1, He

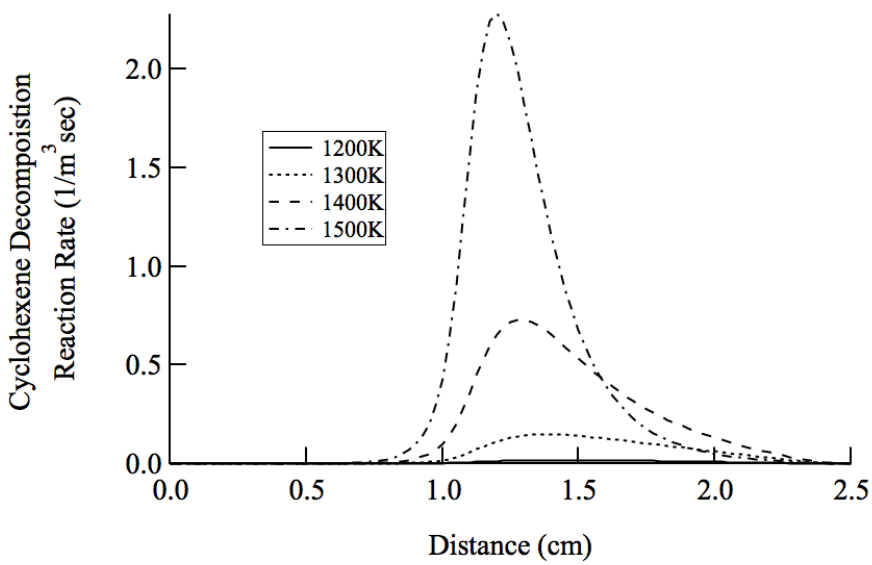

values at the estimated average temperature and pressure.

Figure 3.29: Cyclohexene decomposition rate constant vs. distance: T_{wall} = 1200-1500K, 280 sccm, reactor #1, He

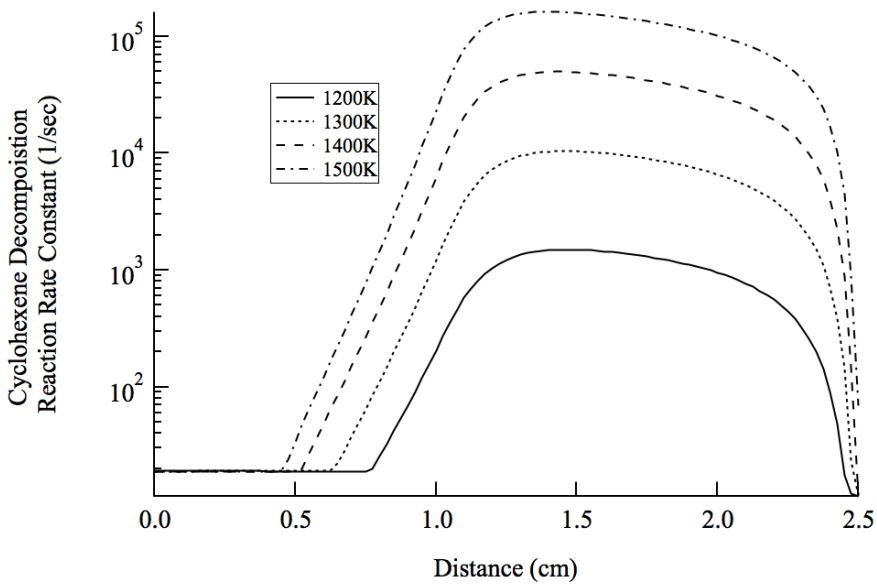

The result of this simple "experiment" is shown in Fig. 3.30 where we plot the "experimental" value of the rate constant determined by using Eqn. 3.8 versus the effective temperature with the pressure set at 35 kPa which is a rough average for the region where reaction occurs. For cyclohexene the sensitivity of the rate constant to pressure is quite small, roughly a 25% change in k_{uni} for a 10 kPa change in the pressure.

3.6.2 Cyclohexene decomposition in argon and neon

The above analysis is for helium as the carrier gas. As mentioned above, helium is used in PIMS experiments because of pumping considerations, whereas argon and neon are used in matrix/IR experiments because of the difficulty in freezing helium. For argon and neon, the flow picture is somewhat different than for helium. In Section 3.1 it was shown that for equal volumetric flow rates argon does not heat as rapidly as helium and the radial temperature profiles are much more pronounced in the high temperature portion of the reactor. In addition, the pressures are somewhat higher throughout the reactor. The consequence is a quite different situation regarding

Figure 3.30: Comparison of "experimental" rate constant from CFD simulations with rate constants calculated at the effective temperature and pressure: T_{wall} = 1200-1500K, 280 sccm, reactor #1, He

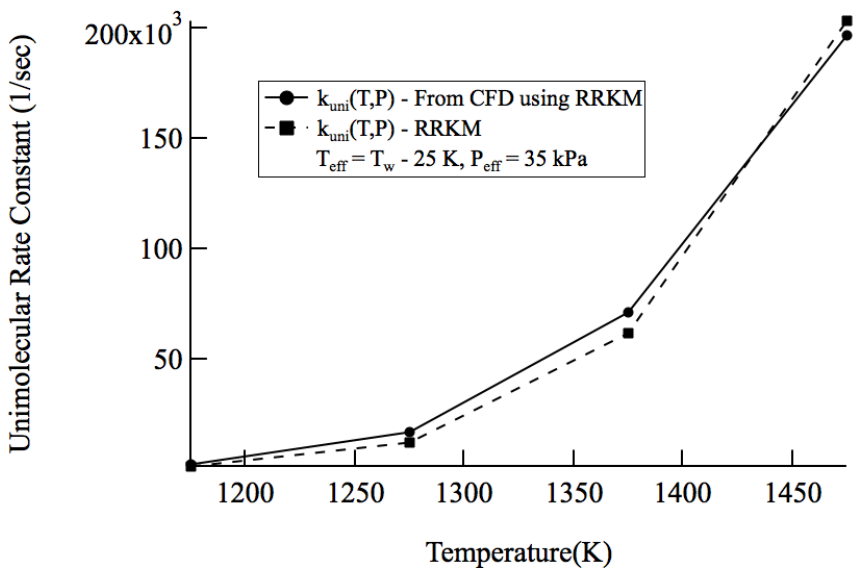

where and when reactions take place. Essentially, for the argon carrier gas, most of the reaction takes place next to the wall and the overall rate of reaction is less than the rate for a helium carrier gas. Neon behavior is intermediate to that of helium and argon. This is illustrated in Fig. 3.31, which shows the mole faction of cyclohexene for the three carrier gases and similar operating conditions. Unlike helium, when using argon or neon as the carrier gas, the product of pressure and temperature along the centerline peaks much further downstream (see Fig. 3.32 for argon) as does the the overall rate of reaction (see Fig. 3.33 also for argon). The consequence is that higher wall temperatures are required for argon and neon to produce the same product set as helium.

Figure 3.31: Mole fraction of cyclohexene vs. distance: T_{wall} = 1500K, 280 sccm, reactor #1, Ar

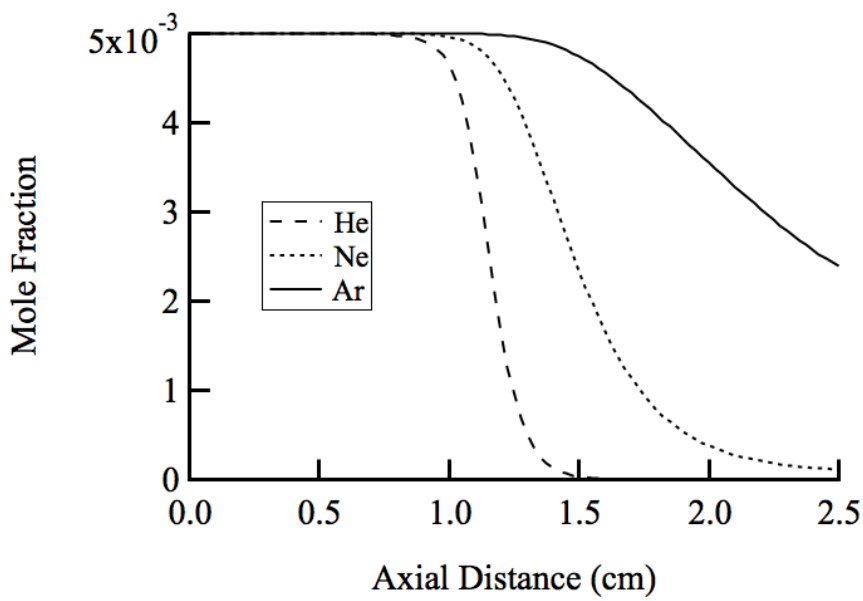

Figure 3.32: Pressure/Temperature product vs. distance: T_{wall} = 1200-1500K, 280 sccm, reactor #1, Ar

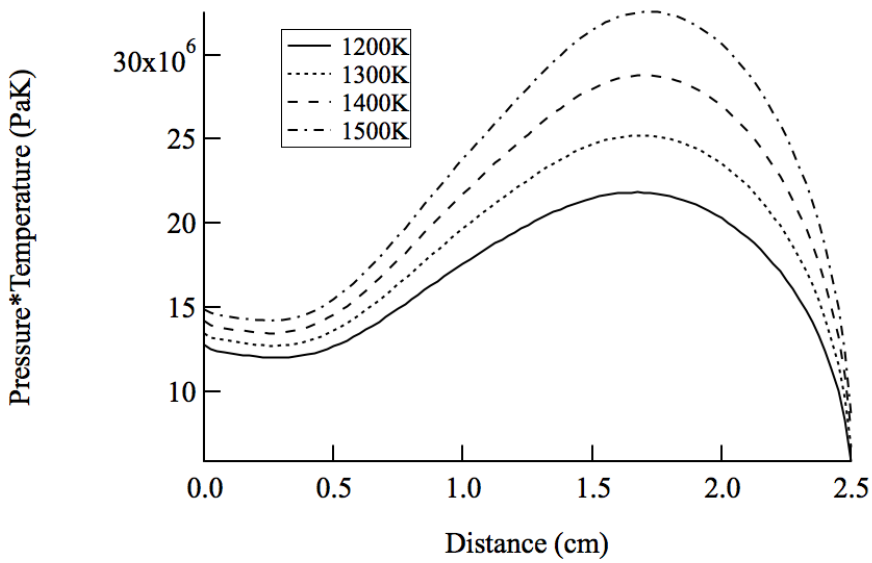

Figure 3.33: Cyclohexene decomposition rate vs. distance: T_{wall} = 1200-1500K, 280 sccm, reactor #1, Ar

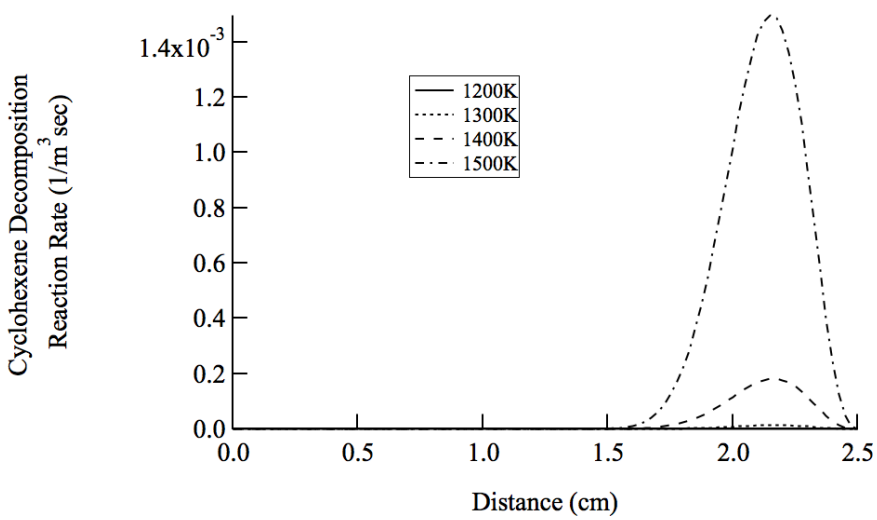

Chapter 4

Development of CFD and DSMC Codes

4.1 CFD solver

4.1.1 Finite volume method (FVM)

The results presented in Chapter 3 indicate that the nonequilibrium phenomenon will occur near the reactor exit when high heating temperatures and low mass flow rates ($\dot{V} < 200$ sccm for helium) are applied. Under these conditions, a pure CFD code cannot correctly capture rarefied gas dynamics in the downstream vacuum chamber. If these incorrect solutions are transferred back to the upstream domain, one would obtain an unphysical flow field solution. We need to apply the DSMC method to solve the non-equilibrium phenomenon. However, commercial CFD codes limit their accessibility and thus cannot be freely coupled with other codes. This is the major reason why we developed our own CFD code.

Our goal for the CFD code was to reproduce the results obtained by the ANSYS Fluent platform. The code is originated from two open sources: one is the "Struct2D" code developed by Blazek [15] and the other is the "OpenCFD-EC" code initiated by Li [83] in the Chinese Academy of Science (CAS). Modifications have been made specifically for our project including non-dimensionalization, boundary conditions, and input/output methods. In this chapter, several of the most important features of our CFD code are introduced. For completeness, a conversion of the two-dimensional (2D) structured code to its two dimensional axisymmetric (2DA) counterpart is given in Appendix C. A typical CFD program is illustrated in Fig. 4.1.

Figure 4.1: Computing cycle of typical CFD programs

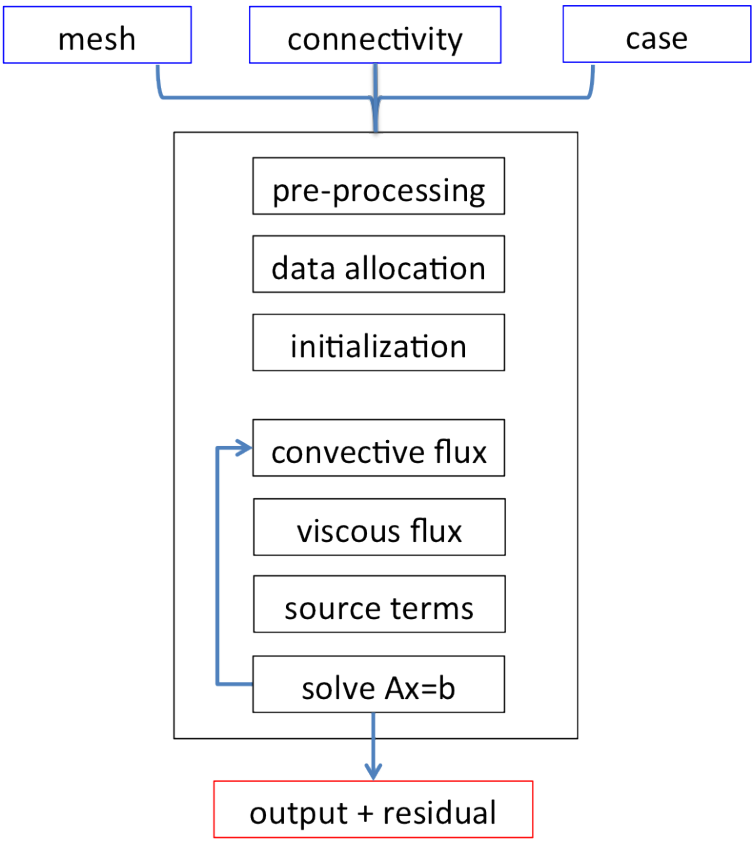

4.1.2 Multi-block data structure

The pyrolysis reactor system has a fairly simple geometry. Based on the fluid physics, it can be generally divided into three sections: (1) the feeding tube section; (2) the reactor section; and (3) the downstream section. Since each section has a distinct feature, a multi-block structured code is appropriate for the simulation where different numerical schemes can be applied in different sections. Here, we borrow the idea of the multi-block data structure from Blazek [15].

Figure 4.2: Three-block structure of the pyrolysis reactor

Our code is a 2D finite volume method (FVM) code and solves the compressible flow conservation equations using a density-based method, for example the Roe type flux or the HLLC type flux. A typical geometry in the CFD code is constructed by several blocks. Fig. 4.2 shows an example of a three-block structure used in the reactor simulation. Structured grids are used and the CFD cell is indexed as (i, j). Different blocks are linked with each other through the description on a connectivity file. To fulfill this multi-block feature, three new data types are defined. They are message type data, block type data and mesh type data.

Figure 4.3: Message data type for CFD code

```
type bcmsg_type
   integer :: f_no
   integer :: face     ! face: face direction
   integer :: ist, iend
   integer :: jst, jend
   integer :: neighb
   integer :: subface  ! subface: f_no in neighb block
   integer :: orient
end type bcmsg_type
```

The structure of the message type data is shown in Fig. 4.3. It defines a kind of variable associated with the faces of a block. Each block is constructed with four sides and on each side

there can be one or multiple faces. The faces are identified with an integer variable, f_{no}. The position of a face on a block is defined by its bounding nodes, $(ist, iend)$ and $(jst, jend)$, on that block. Each face has to be specified with a connectivity attribute, $neighb$. This attribute indicates either a boundary condition applied on the face or another block connected through the face. If the face is connected with another block, then it also needs to know the face number of the block and how information is transferred, which are specified by the integer variables, subface and orient.

Figure 4.4: Block data type for CFD code

```
type block_type
   integer :: Block_no,nx,ny,subface
   ! (x,y) :  coordinate of nodes (vertex)
   real(dp), pointer, dimension(:,:)   :: x,y
   ! (x1,y1): coordinate of cell center
   real(dp), pointer, dimension(:,:)   :: x1,y1
   real(dp), pointer, dimension(:,:)   :: vol,si,sj
   real(dp), pointer, dimension(:,:)   :: ni1,ni2,nj1,nj2

   real(dp), pointer, dimension(:,:,:) :: U,Un
   real(dp), pointer, dimension(:,:,:) :: Res      !
   real(dp), pointer, dimension(:,:)   :: dt       !
   real(dp), pointer, dimension(:,:,:) :: QF       !
   real(dp), pointer, dimension(:,:,:) :: deltU    !
   real(dp), pointer, dimension(:,:,:) :: dU       !
   real(dp), pointer, dimension(:,:)   :: Amu, Amu_t

   real(dp), pointer, dimension(:,:) :: Lci,Lcj,Lvi,Lvj
   real(dp), pointer, dimension(:,:) :: d2w

   type(bcmsg_type), pointer, dimension(:) :: bc_msg
end type block_type
```

The block type data (See Fig. 4.4) defines a kind of variable which contains geometrical quantities (location of nodes, cell-centers, and volume) and physical variables (conservative solution, residual and spectral radii) of all the cells on one block. It also records the index of the block, $Block_{no}$, the number of cells or nodes along I and J directions, nx and ny, and the number of faces around it, $subface$. A message type variable, bc_{msg}, is used to record the boundary and connectivity information of the faces on the block. Since the number of cells and faces on a block are not known before computation starts, these variables are defined with a pointer attribute.

The mesh type data (See Fig. 4.5) defines a kind of variable which stores all the blocks used in the computation, $Block$, the total number of blocks and cells in the mesh, Num_{Block} and Num_{Cell}.

Figure 4.5: Mesh data type for CFD code

```
type mesh_type
   integer :: Mesh_no
   integer :: Num_Block
   integer :: Num_Cell
   integer :: Kstep
   integer :: Nvar
   integer :: Iflag_turbulence
   integer :: Iflag_Scheme
   integer :: IFlag_flux
   integer :: IFlag_Reconst
   real(dp):: Res_max(6),Res_rms(6),time
   type(block_type),pointer,dimension(:) :: Block
end type mesh_type
```

It also records the number of conservation equations, N_{var}, time step index and size, K_{step} and time, and numerical scheme choices associated with the whole computation. The multi-block data structure is considered suitable for our problem since we realize that there will be different flow features in our system and they should be treated separately. For example, it is considered that the flow field of the reactor section is most important and high order of accuracy is desired. Thus, we can separate the reactor section as a special block and apply high order numerical schemes in it while maintaining low order schemes in the other blocks.

4.1.3 Time integration methods

The CFD solver provides both explicit (backward Euler or three-stage Runge-Kutta) and implicit (LU-SGS) time-marching methods. Since we are solving a steady state problem, an implicit method can allow us to use larger CFL numbers and increase the computational speed. Thus, the LU-SGS method is used in our project.

4.1.4 Pressure boundary condition

When the inlet pressure is given while the mass flow rate or inlet velocity is unknown, one should use a pressure inlet boundary condition. In this boundary condition, one has to provide the following information: total pressure, p_0, total temperature, T_0, and an estimated static pressure,

p_s. For a compressible flow, we apply isentropic relations of an ideal gas for the total pressure, static pressure, and velocity at a pressure inlet boundary [62, 29]:

$$\frac{p_0}{p_s} = \left(1 + \frac{\gamma - 1}{2} M^2\right)^{\frac{\gamma}{\gamma-1}} \tag{4.1}$$

where

$$M \equiv \frac{v}{c} = \frac{v}{\sqrt{\gamma R T_s}} \tag{4.2}$$

Here c stands for the speed of sound, and $\gamma = c_p/c_v$. Through the above two equations, the velocity magnitude on an inlet boundary cell can be determined. The components of the velocity shall be derived from the face directions.

Density at the inlet is deduced from the ideal gas law:

$$\rho = \frac{p_s}{R T_s} \tag{4.3}$$

Static temperature at the inlet, T_s, is computed from the input total temperature and the local Mach number:

$$\frac{T_0}{T_s} = 1 + \frac{\gamma - 1}{2} M^2 \tag{4.4}$$

At the outlet of the reactor, a static pressure p is required. In our study, a low value is given for the back pressure. When the flow is locally supersonic, the specified pressure will not be used and static exit pressure will be extrapolated from the flow inside.

4.1.5 Density based method

Our CFD code is a cell-centered FVM code. This means that during the calculation, all conservative variables, $\{\rho, \rho u, \rho v, \rho E\}$, will be stored at the center of the cells. Convective fluxes such as HLLC, Steger-Warming, Van-Leer and Roe are implemented [66]. Reconstruction schemes such as MUSCL, NND, and WENO are given for higher order accuracy solutions. In order to deal with compressible flow and solve shock structures that might happen downstream of the reactor, and to directly compare the results with ANSYS Fluent simulations, Roe's method and 2nd order upwind discretization are used for our problem.

4.2 DSMC solver

From Sec. 2.4, we know the Boltzmann equation is a mathematical description, which can be applied to flow conditions with all regimes. It is a deterministic approach but very hard to directly solve due to the complex integral-differential term on the right hand side of the equation. In practice, we often choose to use DSMC for non-equilibrium flows.

4.2.1 DSMC basics

The DSMC method is based on the assumption that a small number of representative "simulated particles" can accurately capture the bulk macroscopic dynamics and thermodynamics of a complete system of gas atoms and molecules. This assumption holds for the case of a dilute gas which is a good approximation of a real gas when the ratio of the mean atomistic spacing δ to atomistic collision cross-section d is such that $\delta/d > 1$. Empirical results show that in order to capture the fluid physics at least 25 "simulated particles" are needed in one typical DSMC sampling cell [13, 65], which is on the order of the size of a local mean free path.

The number of real molecules represented by one "simulated particle" is called the scaling factor, which usually is a large number. In a typical DSMC simulation, the physical domain will be split into a number of different computational cells. The particles within the domain are advanced in discrete time steps. The cell size Δx_{DSMC} and the time step size Δt_{DSMC} have great impacts on the accuracy of the simulation [2, 35, 36]. Commonly, the following requirement should be met:

$$\Delta x_{DSMC} < 1/3\ \lambda \quad \text{and} \quad \Delta t_{DSMC} < 1/3\ \tau \tag{4.5}$$

where λ is the local mean free path and τ is the mean collision time.

The above requirement comes from the assumption of DSMC's no-time-counter (NTC) scheme, where the movement and collision of particles are separately treated. It has been proven that, in the limit of $\Delta x_{DSMC}, \Delta t_{DSMC} \to 0$, the DSMC simulation will proceed to the correct solutions to the Boltzmann equation [77].

4.2.2 DSMC components

A typical DSMC program is shown in Fig. 4.6. The flow is initiated by specifying a distribution of particles throughout the physical domain. The positions of these particles are randomly set while their thermal velocities are usually sampled from a Maxwellian distribution. Then the boundary flows are specified with the following information: number flux, temperature and bulk velocity. The program evolves through three major steps during one Δt_{DSMC}: Move, Index, and Collide.

In the Move step, particles follow simple translational movements both within the flow domain and along the stream boundaries. Particles within the flow domain have a flight time of a full discrete time step Δt_{DSMC}. Particles coming from the stream boundary have a random fraction of the full time step, i.e. $\mathscr{R} \cdot \Delta t_{DSMC}$, where $\mathscr{R}$ is a uniform random number from (0,1):

$$x_i(t + \Delta t_{DSMC}) = x_i(t) + \mathbf{v}_i(t)\Delta t_{DSMC} \tag{4.6}$$

After the movement, the particle position x_i is immediately checked to determine whether it will have an interaction with the domain boundaries. If the particle hits on a wall boundary, then it reflects back to the domain following the user specification (either specular or diffuse). In a specular reflection, the velocity of the particle normal to the wall is reversed while the tangential component remains the same. In a diffuse reflection, the reflection velocities are sampled from a biased Maxwellian distribution based on the wall temperature.

In the Index step, particles are sorted into cells and sub-cells in order to process collisions. The particles are arranged in a cross-reference array which keeps their tracks by recording their cell and subcell. If a particle travels out of the flow domain, its information will be deleted from the array. Indexing of the particles helps identify them in the moving and collision steps.

In the Collide step, binary collisions are modeled in a probabilistic way by using Bird's NTC scheme. Particle pairs within a cell are randomly selected to undergo binary collisions. The probability of a collision event depends on the relative velocity and collision cross-section of the pair. The cross-section is computed using an appropriate collision model, which typically includes

Figure 4.6: Computing cycle of typical DSMC programs

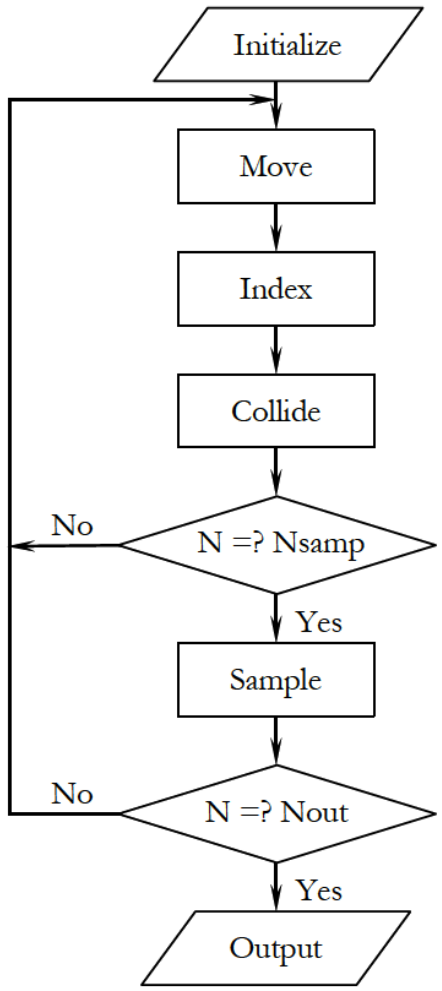

hard sphere (HS) model, variable hard sphere (VHS) model and variable soft sphere (VSS) model. In our study, we use VHS model for the collisions.

As mentioned above, collision is a probabilistic step because collision pairs are randomly selected among simulated particles. During a time step Δt_{DSMC}, within a cell of volume V_c, the total number of molecule pairs, which will be selected to collide, is [10]:

$$N_{selected} = \frac{N_c(N_c - 1)\pi d^2 v_r^{max} \Delta t_{DSMC}}{2V_c} \tag{4.7}$$

Here N_c stands for the number of particles per cell and v_r^{max} is the maximum relative speed in the cell. An acceptance-rejection scheme [10] is often used to select the collision partners between particle i and j according to the following steps:

a. Randomly select a pair of particles i and j for collision;

b. Calculate the relative speed v_r between the particle pair;

c. If the product of the cross-sectional area and this relative speed is greater than or equal to the product of the maximum recorded value and a random number $\mathscr{R}$, i.e. $\sigma v_r \geq \sigma v_r^{max} \cdot \mathscr{R}$, then this collision event will be accepted. Here v_r^{max} is the maximum relative speed recorded in the cell, and σ is the cross sectional area of the particle pair;

d. If the selected collision pair is accepted, we compute post-collision velocities v_i' and v_j';

e. If the pair is rejected, return to step **a**.

For a steady problem, the flow field is assumed to reach a steady state after a sufficient number of Move-Index-Collide iterations. At a certain frequency, particles within a cell are gathered to sample out the macroscopic data, i.e. density, velocity and temperature.

4.2.3 Multi-block data structure

We notice that, in the supersonic expansion zone downstream of the reactor, the flow number density varies greatly along the axial and radial distance. It would be wise if the mesh can adapt

the local flow density, i.e. finer mesh is applied near the exit while coarser mesh is adequate for the region far away. Thus, we borrow the idea of a multi-block data structure from CFD and implement it in DSMC. Fig. 4.7 shows the block type variable.

Message connectivity information is not necessary since the storage of particles' information is independent from the geometry. In each block, cells can be set with a uniform size or exponential growth. With the block data type, the mesh setting becomes very flexible since different cell sizes and numbers can be applied. Fig. 4.8 shows an example used in the study.

4.2.4 Macroscopic stream boundary

Local thermodynamic equilibrium is assumed on the stream boundary. The standard flux boundary [10] introduces particles through an emission surface. The flight time for those boundary entering particles is a random fraction of the time step Δt_{DSMC}. To better connect with the upstream CFD solutions, we use a macroscopic state boundary [49]. In this type of boundary, the user is asked to provide the macroscopic states. A layer of reservoir cells are created along the boundary. The flow density is used to set up the number of particles within the cell. The positions of the particles are randomly allocated within the reservoir cells. The thermal velocities of the particles are sampled from a Maxwellian distribution based on the temperature and then added into the macroscopic velocity to form the complete set of velocities. The difference between the two stream boundaries is illustrated in Fig. 4.9.

4.2.5 Species weighting factor

In a typical pyrolysis experiment, several products might be generated. We are very interested in the distributions of these species, especially the number density distribution in the vacuum chamber. To simulate this, the DSMC code must have multispecies functionality. Although the biomass species are usually the ones of greatest interest, they normally constitute very small fractions compared with the carrier gas. Their typical mole fractions are about 0.1% or less. This small number makes the DSMC simulation very difficult. The reason is that as a statistical approach, a

Figure 4.7: Block data type for DSMC code

```
type block_type
   integer :: pre_tot_cell
   integer :: pre_tot_subcell
   integer :: pre_tot_surf

   integer :: num_surf
   integer :: num_surf_elem
   integer :: num_cell
   integer :: num_subcell
   integer :: block_id
   integer :: num_buffer_cells

   ! boundaries
   integer :: IB(4)
   real(dp):: CB(4)
   real(dp):: CW, CH, FW, FH
   integer :: LFLX, LFLY

   real(dp):: CWRX, CWRY
   real(dp):: APX, RPX
   real(dp):: APY, RPY

   ! # of cells in x and y
   integer :: NCX, NCY
   integer :: IFCX, IFCY

   integer, dimension(:),  pointer :: isurf
   integer, dimension(:,:),pointer :: LIMS
   real(dp),dimension(:),  pointer :: tsurf, wsurf
   real(dp),dimension(:),  pointer :: ALPI, ALPN, ALPT

   real(dp), dimension(:,:,:), pointer :: AME
   real(dp), dimension(:,:,:), pointer :: AMR

   integer :: num_jet

   integer, dimension(:),     pointer :: IJET
   integer, dimension(:,:),   pointer :: LIMJ
   real(dp),dimension(:),     pointer :: TMPJ, FNDJ
   real(dp),dimension(:),     pointer :: FVJ,  WJ
   real(dp),dimension(:,:),   pointer :: FSPJ
   real(dp),dimension(:,:,:), pointer :: AMEJ, AMRJ
end type block_type
```

Figure 4.8: Downstream multiblock mesh for DSMC simulation

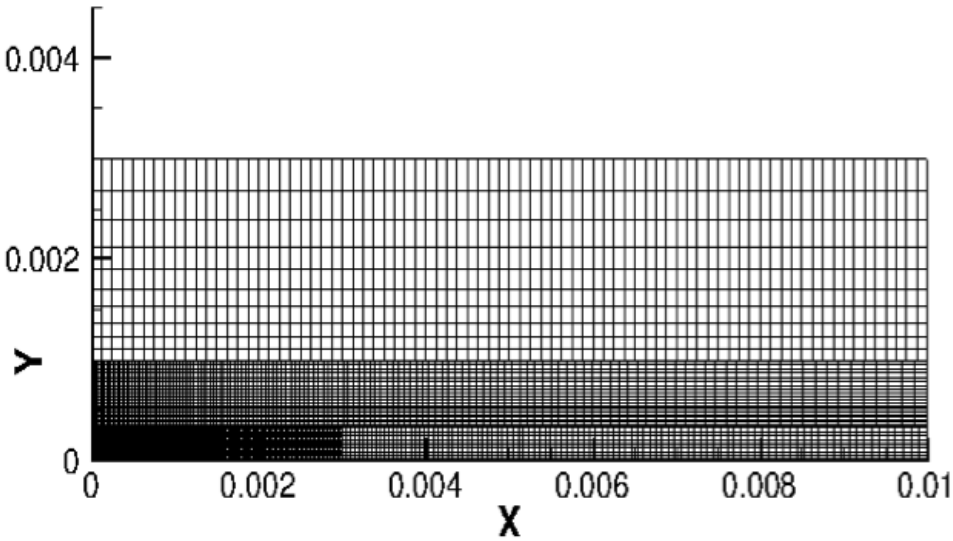

Figure 4.9: Standard and reservoir boundary conditions for DSMC (left: standard stream boundaries; right: reservoir boundary using local thermodynamics states)

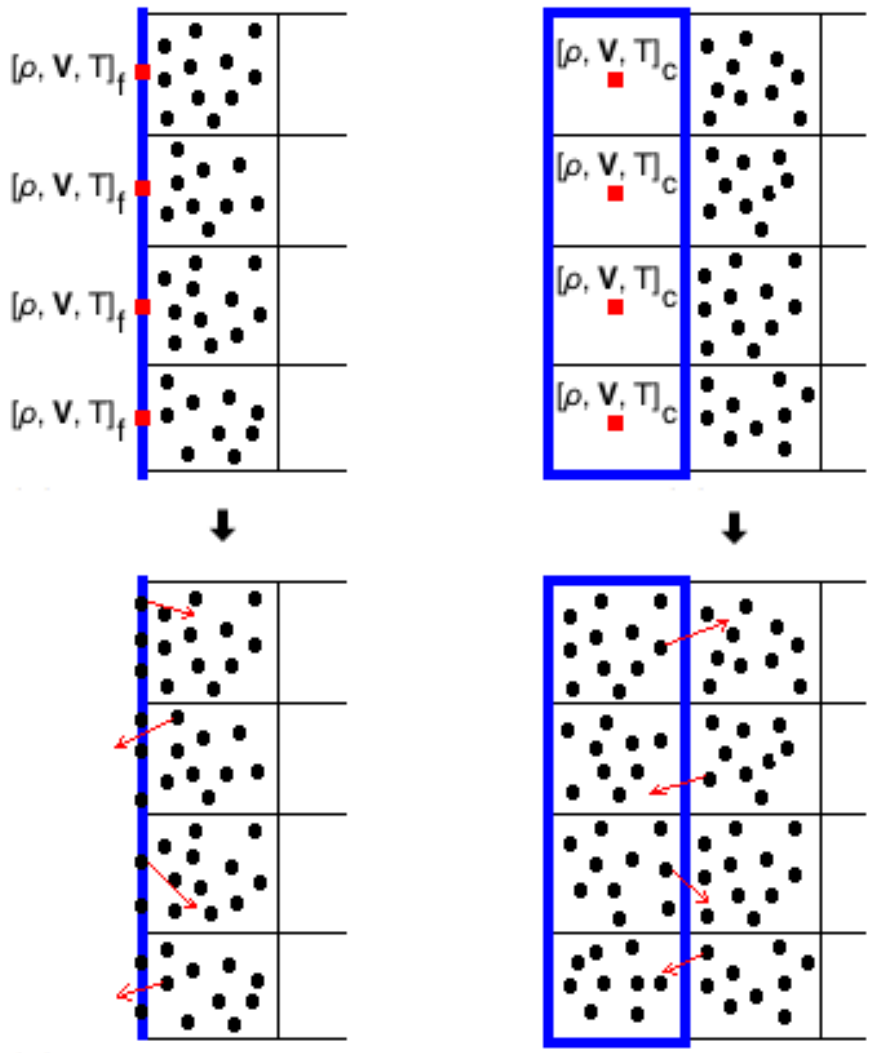

sufficiently large number of simulated particles are needed to gather accurate information within a cell. Bird suggests at least 25 simulated particles per sampling cell for each species [13]. For a mixture of 1% "seeded" argon in a 99% helium carrier gas, if a single scaling factor or weight is employed for both species, at least 25 argon molecules per cell and 2475 helium molecules are needed. Apparently, the number of helium molecules is much more than required and leads to a very heavy computational cost. In order to avoid this, we implement the species-dependent weighting scheme invented by Bird [11].

In the species-dependent method, the scaling factors or weights of different species are allowed to change. They will roughly scale with the mole fractions of each species. Thus species with different number densities will have roughly the same particles in each cell. For instance, in a gas mixture with a total number density n, the number of particles for species i will be:

$$N_i = \frac{nV}{W_i} \tag{4.8}$$

where V is the cell volume and W_i is the particle weights for species i.

The variable weights bring a problem during collision events. Consider the number of collisions between particles of species a and b, $(N_c)_{a,b}$ within a cell. Based on the NTC scheme [10], this number becomes:

$$(N_c)_{a,b} = \frac{n_a N_b \Delta t (\sigma g)_{max}}{P_{a,b} + (W_b/W_a) P_{b,a}} \tag{4.9}$$

Here W_a and W_b are the particle weights of species a and b, respectively. Probability $P_{a,b}$ represents the chance of property change when species a collides with species b. Assuming species a is the carrier gas, then their particle weights have the relation of $W_a > W_b$ and the probabilities are:

$$P_{a,b} = W_b/W_a \quad \text{and} \quad P_{b,a} = 1 \tag{4.10}$$

As one can find out, when a and b are the same species, the above equations resolve to the normal NTC collision formula.

This species-dependent weighting scheme solves the problem of excessive simulated molecules. However, it fails to conserve the momentum and energy during the collision. As one can see from

Eqn. 4.10, for species with higher weights, the probability of properties change in a collision is given by the ratio of particle weights, which is not physically correct. To circumvent this, Boyd invented the conservative weighting scheme using the split-merge method [17].

The split-collide-merge method is illustrated in Fig. 4.10. First, before the collision between a carrier gas particle and a seeded gas particle happens, the carrier species particle (W_1) will be split into a particle with weight (W_2) and a particle with weight of ($W_1 - W_2$). Then collision is performed between the split carrier gas particle with weight (W_2) and the seeded species particle with weight (W_2). After the collision, the two split carrier gas particles are merged and thus linear momentum of the system is exactly conserved.

Unfortunately, the total energy of the system is not conserved and is continuously lost. If the pre-collision velocity of the carrier gas particle is (u_1, v_1, w_1) and the post-collision velocity is (u_1', v_1', w_1'), one can determine that the energy loss during a collision is:

$$\Delta E = \frac{1}{2} W_1 m_1 \phi (1 - \phi)[(u_1 - u_1')^2 + (v_1 - v_1')^2 + (w_1 - w_1')^2] \tag{4.11}$$

which is always greater than zero. This energy loss between the carrier gas particle and the seeded gas particle is kept tracked and summed up in each cell. Boyd suggested that in the subsequent collision between two carrier gas species particles, the energy loss sum is added back into the system by increasing the relative velocity. Apparently, this adding process is not physically correct. But through this process, energy is "systematically" conserved [17].

4.3 Hybrid CFD/DSMC methods

A hybrid method is to couple CFD and DSMC and separately solve the continuum and rarefied flows coexisting in a domain. Its application varies among microscopic scale fluid dynamics, such as micronozzle trusters [41] to vacuum flow scenarios such as chemical vapor deposition systems [40]. Whenever a transition from continuum to rarefied exits, a hybrid method is needed. A hybrid method usually comprises three stages: (1) decide a split boundary to separate continuum and rarefied domains; (2) solve the continuum domain with the CFD method and the rarefied

Figure 4.10: Split-merge method in conservative collision scheme (adapted from [81])

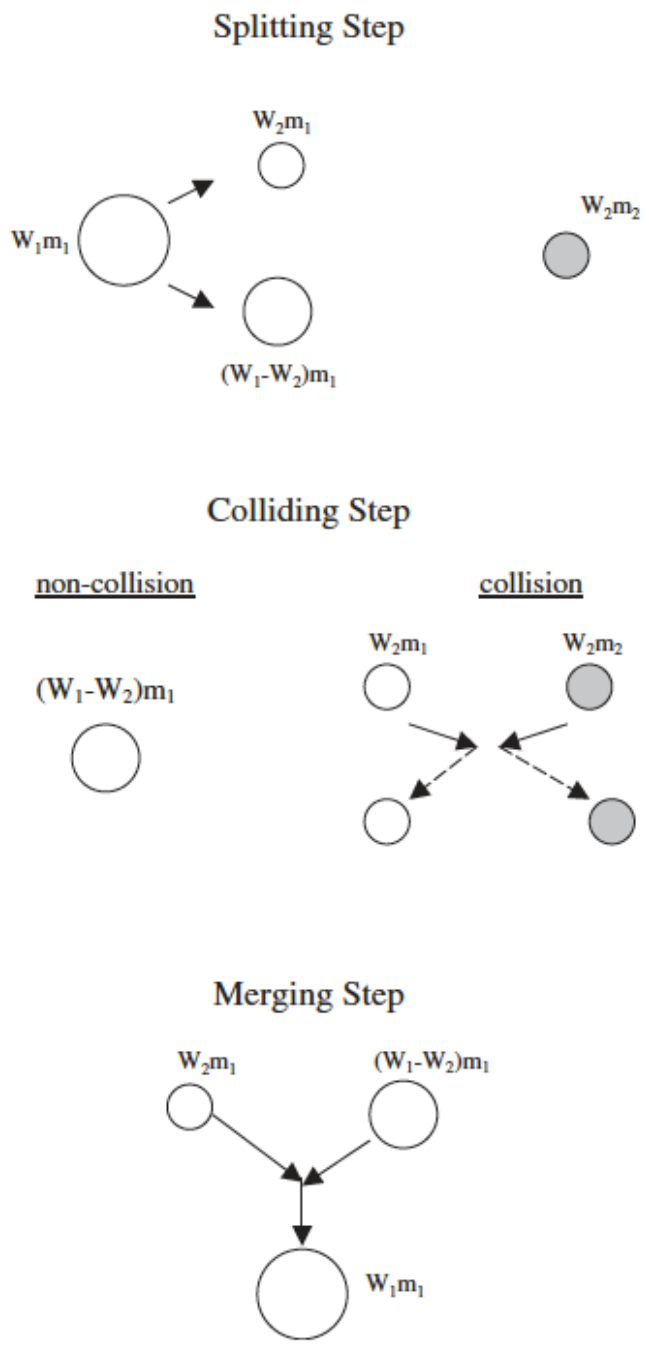

domain with the DSMC method; (3) exchange information between the CFD and DSMC domains. Depending on how the information transfer is conveyed, one can generally separate the coupling into two categories.

4.3.1 Zonally-decoupled CFD/DSMC method

The first category is called the zonally-decoupled method [80], in which an artificial split boundary is placed between the CFD and the DSMC regions. In order to use this method, two requirements need to be satisfied. First, the flow properties along this split boundary should be in thermal equilibrium ($Kn < 0.05$) so that the velocity distribution is adequately defined by a Maxwell-Boltzmann distribution. Second, the flow velocity normal to the split boundary should be supersonic. Under this condition, macroscopic flow properties along the split boundary are considered to be independent of the downstream conditions so that information only needs to be transferred one way from the CFD region to the DSMC region [80, 33]. The upstream and the downstream flow fields are then separately solved by the CFD and DSMC methods. To apply the macroscopic properties to the DSMC domain, one can use either the standard flux boundary or the macroscopic stream boundary introduced above .

4.3.2 Fully coupled CFD/DSMC method

If the flow on the split boundary is subsonic, subsonic information from the rarefied flow region will travel back to the continuum flow region and the zonally-decoupled method is no longer justified. Instead, a fully coupled CFD/DSMC method should be used. In this method, one needs to compute a breakdown parameter, Kn_L, to split the continuum and rarefied domains:

$$Kn_L = \frac{\lambda}{L} \tag{4.12}$$

Here L stands for a local characteristic length since a general characteristic length L is not appropriate for cases with large flow property variations. Bird [10] first proposed a local characteristic

length based on the density gradient:

$$L = \frac{\rho}{\Delta\rho} \tag{4.13}$$

Boyd [18] extended the local characteristic length by also including gradients of $\|V\|$ and translational temperature T. The final local characteristic length is the minimum of the three. This yields the maximum local Knudsen number which is then used to split the flow domain. $Kn_L = 0.05$ is used as a common standard. If $Kn_L \leq 0.05$, the flow is regarded as a continuum flow and the CFD method is applied on this domain. If $Kn_L > 0.05$, the DSMC method is used.

Information transfer in the fully coupled CFD/DSMC method is carried out in two directions. The solution from one domain is used as the boundary condition for the other domain. From CFD to DSMC, macroscopic information is converted to microscopic information using a state-based method or flux-based method. From DSMC to CFD, microscopic information is averaged to macroscopic information through sampling and transferred back as the boundary condition for the CFD domain. Very often, an overlap layer is applied between the CFD and DSMC domains. The width of this overlap region usually spans about two to three CFD cells. It is used to control the statistical error coming from the averaging of the microscopic properties and to suppress the fluctuation of the particle information coming from the CFD boundary [57, 56, 58].

After reaching the steady state in both the continuum and the rarefied regions, one will recompute the local Knudsen number and update the CFD and DSMC domains. This cycle continues until the split boundary and flow field reaches a steady state.

4.3.3 Hybrid code structure

As stated above, a comprehensive hybrid code should be able to compute the breakdown parameter and properly transfer the information between the CFD region and the DSMC region. Currently for our problem, we mainly use the zonally-decoupled CFD/DSMC method. The organization of the code is shown in Fig. 4.11. During the computation, the CFD module will be used to compute the continuum flow in the reactor section. Then based on the outlet condition, the mesh and boundary condition files for the downstream DSMC module will be generated. The DSMC

solver will compute the rarefied flow in the downstream chamber.

Figure 4.11: Code structure for hybrid CFD/DSMC

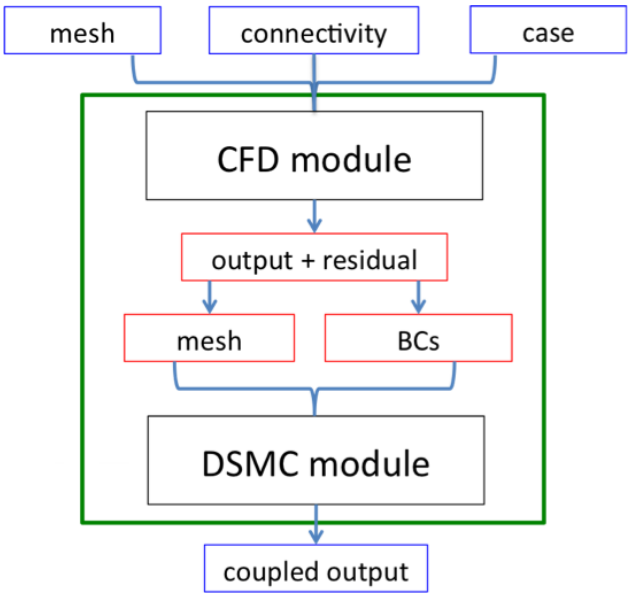

Chapter 5

Downstream Vacuum Simulations with DSMC Method

As introduced in Sec. 2.4 of Chapter 2, the reactor is placed in a vacuum chamber with pressure held below 10^{-4} torr for further diagnostics. With a sufficiently high mass flow rate, the exhausting gas from the reactor will form an underexpanded supersonic jet in the vacuum chamber. However, if the mass flow rate is low, the continuous condition of the flow within the reactor may be deteriorated. The limiting condition of this deterioration is a fully effusive source. Anderson et al. [4] compared the supersonic source with the effusive source. The difference between the two is illustrated in Fig. 5.1.

Compared with the effusive beam, the supersonic molecular beam has advantages in terms of higher flow rate per unit area in the axial direction, more focused spatial distribution due to higher mean velocity, and higher energy intensity. However, it also requires a stronger pumping capacity especially for cases with CW reactors. This definitely increases the cost on the facilities. In the experiment, we always want to minimize the cost on pumping requirements and at the same time maximize the diagnostic signals and maintain the continuum property of the flow within the reactor. This requires knowing the distribution of the flow properties within this expansion. Understanding the expansion physics can be very helpful in the design aspect of this "nozzle-beam" system.

A useful indicator to judge the continuous condition of the flow is the Knudsen number Kn_e at the reactor exit. The diameter of the tubular reactor D can be used as an appropriate characteristic length. Based on the local mean free path λ_e, we shall have:

Figure 5.1: Comparison of effusive oven beam and supersonic nozzle beam (adapted from [4])

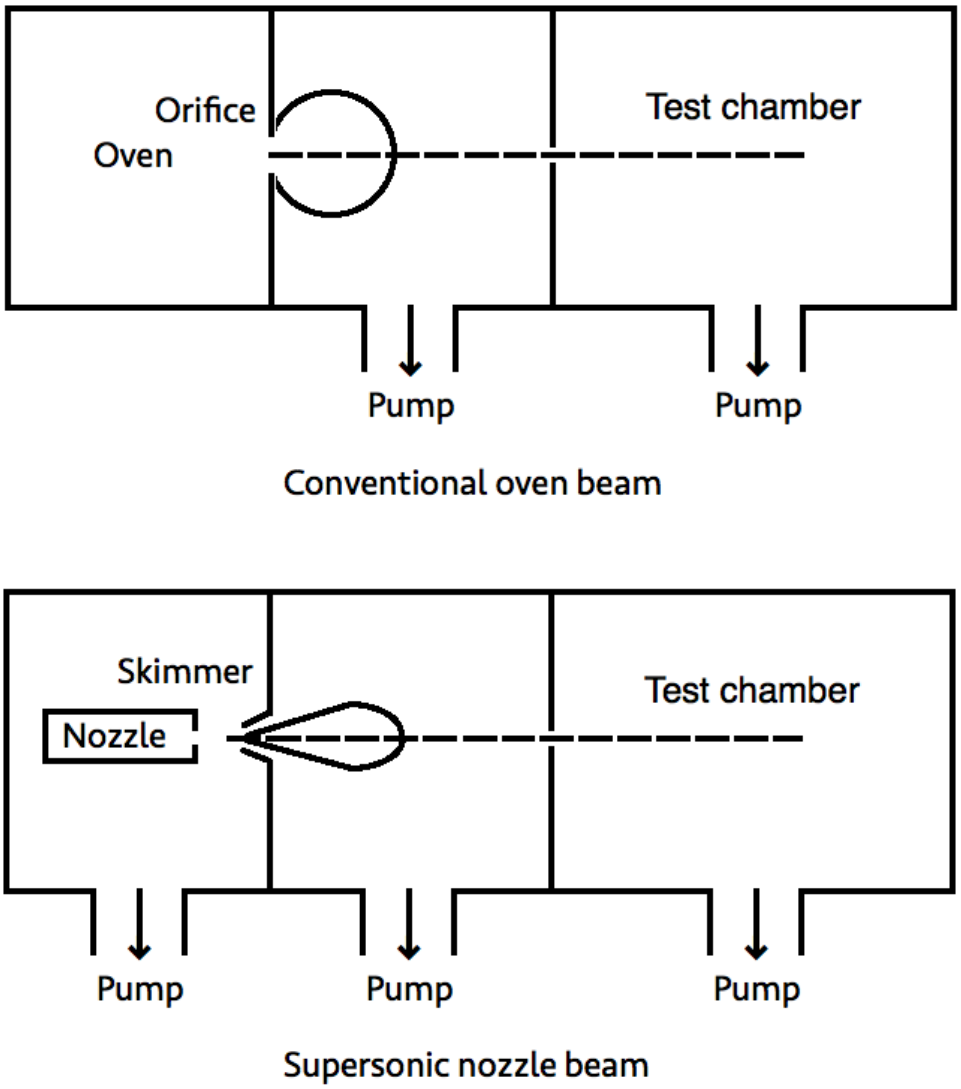

$$Kn_e = \frac{\lambda_e}{D} \tag{5.1}$$

When $Kn_e \leq 0.01$, the flow condition at the reactor exit is considered to be a continuum flow. Under the low background pressure, flow exhaust will end up being a supersonic underexpanded jet. When $Kn_e > 0.01$, the expansion starts showing some effusive features. For instance, the expansion is less focused on the axis and the terminal velocity is lower. Gas expansion physics from a reservoir into a vacuum is comprehensively studied by Miller et al. [45]. Similar physics about the supersonic sources are found in the studies of chemical vapor depositions [22, 20] or nozzle plume flows [32, 72].

5.1 Supersonic jet expansion

5.1.1 Important properties

We have introduced the expansion physics along with the continuous supersonic jet expansion structure (see Fig. 1.5) in Chapter 2. The idea of the "quitting surface" model is also explained to describe the transition process and coarsely predict the transition position. Some of the most important properties during this process include:

a. Temperature. In itself, temperature represents the velocity distribution of the molecules. Temperature will drop rapidly in a short distance due to flow acceleration in the expansion. Of course, further downstream there will not be enough collision frequency to maintain thermodynamic equilibrium and the original definition of temperature loses its meaning. As a way of interpreting the physics, we are interested in the behavior of temperature dropping and how the collision affects it. As stated in Chapter 2, one can separate the velocity distribution into perpendicular $f(v_\perp)$ and parallel $f(v_\parallel)$ directions and a comparison between the simulation and the theoretical prediction has already been shown.

b. Velocity. The mean velocity of the flow will accelerate rapidly and reach an asymptotic limit called "terminal speed" v_∞. It is interesting to see how the simulations and the

theoretical predictions will differ. Another factor to look at is the velocity distribution of the beam molecules. The supersonic nozzle beam has the advantage of generating high intensities and focused velocity distributions. As the Mach number of the gas expansion gets higher, the axial velocity distribution will become narrower, i.e. more focused.

c. **Number density**. The number density distribution is crucial to us in the sense that all the measurements on the diagnostic spot are based on this parameter. In the real experiment, we are always interested in the intensity of the "seeded products". For a mixture gas, there is a phenomenon called "species enrichment". That is, the fractions of these "seeded products" in the beam become more abundant than in the reactor section due to the Mach number focusing effect of heavier molecular mass. The species fraction ratio in the mixture beam inversely scales with the molecular mass. An example is given by [4], where in a mixture of 1% nitrogen in hydrogen in the supersonic jet, under ideal conditions, the beam would contain about 14% nitrogen.

The operating conditions and carrier gas are always modulated during the real experiments. Estimated values from the empirical relations will not be able to accurately capture the expansion physics. Thus we need to carry out numerical simulations. As previously mentioned in Chapter 1, the DSMC method is chosen.

5.1.2 DSMC simulations of the expansion region

The concept of DSMC is illustrated in Chapter 4 as part of a larger picture of the coding. The results are presented here. Simulations are carried out using a modified code of Bird's axisymmetric program named DSMC2A [10]. The modeled geometry is 1 cm long with a radius of 0.3 cm. To investigate the flow field variations under different conditions, we have run and compared three simulations with the inlet stream properties taken from the CFD results of Reactor #1 (Table 3.2) in Chapter 3. The conditions are listed in Table 5.1 with different wall temperatures and carrier gases. Multiblock mesh is used to adapt the density variation in the vacuum. Fig. 5.2 shows an

example of the mesh used in helium exhaust with $T_{wall} = 1500$ K. Of course, different computational parameters should be carefully picked up under different conditions. Time step and minimum cell size (at the stream inlet) are listed in Table 5.1. Vacuum boundaries are used on the bounding edges. Particles leaving the domain are deleted from the program.

Table 5.1: Modeled cases of downstream expansion

	Carrier gas	T_{wall}	Δt_{DSMC}	Δx_{min}
Case #1	helium	300 K	1×10^{-8} sec	1×10^{-5} m
Case #2	helium	1500 K	5×10^{-9} sec	1×10^{-5} m
Case #3	argon	1500 K	1×10^{-9} sec	1×10^{-6} m

Contour plots of the distributions of the Mach number, Knudsen number, and log10 of the number density of Case #1 are shown in Figs. 5.3 to 5.5. Quantitative analysis are made by plotting the centerline profiles. We are mostly interested in the centerline distributions of density, temperature, velocity and Mach number. A comparison between the three cases can tell us the difference and the impacts of the upstream flow conditions. They are plotted in Figs. 5.6 to 5.9.

As can be seen, the static temperatures drop extremely rapidly to very low values within one to two reactor diameters. This is one of the advantages of the supersonic beam source as the reactions are quenched due to the cooling and can thus be ignored in the expansion region. The number density is plotted with log10 format. As we can see, the droppings generally follow the same slope. This is the geometric decreasing of $1/x^2$ introduced in Chapter 2. On the other hand, the velocity, and thus the Mach number, increases rapidly, with the velocity reaching an asymptotic limit which is also named "terminal velocity", v_∞. The absolute value of the terminal velocity depends on the carrier gas and its thermodynamic properties. Apparently, lighter and hotter species will lead to a higher terminal velocity. As shown in Fig. 5.8, the terminal velocity for the case of 1500 K helium can reach as high as 3800 m/s. This value agrees well with the theoretical prediction given by Eqn. 2.21 and is validated (see Fig. 5.10) in the experiment using a delay line imaging technique.

Figure 5.2: Geometry and multi-block mesh of the DSMC model

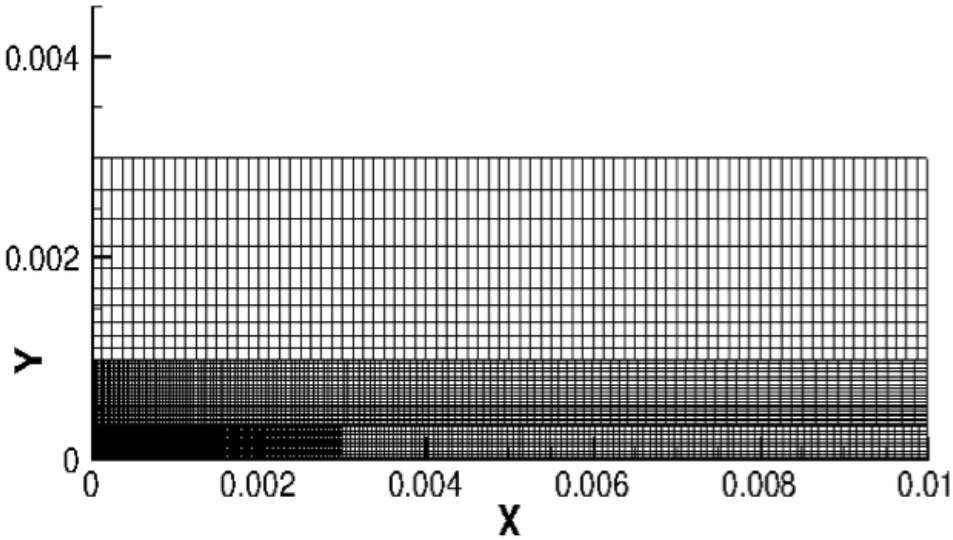

Figure 5.3: Mach number contour in a supersonic underexpanded jet

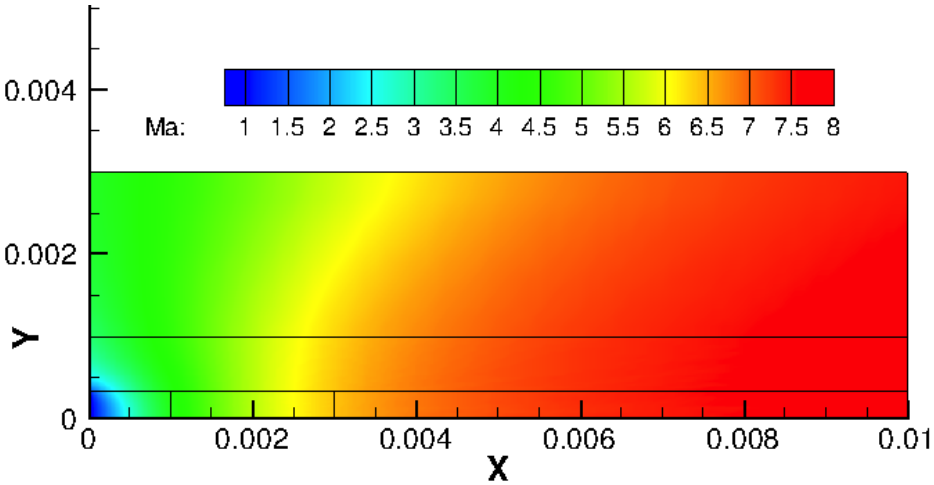

Figure 5.4: Knudsen number contour of a supersonic underexpanded jet

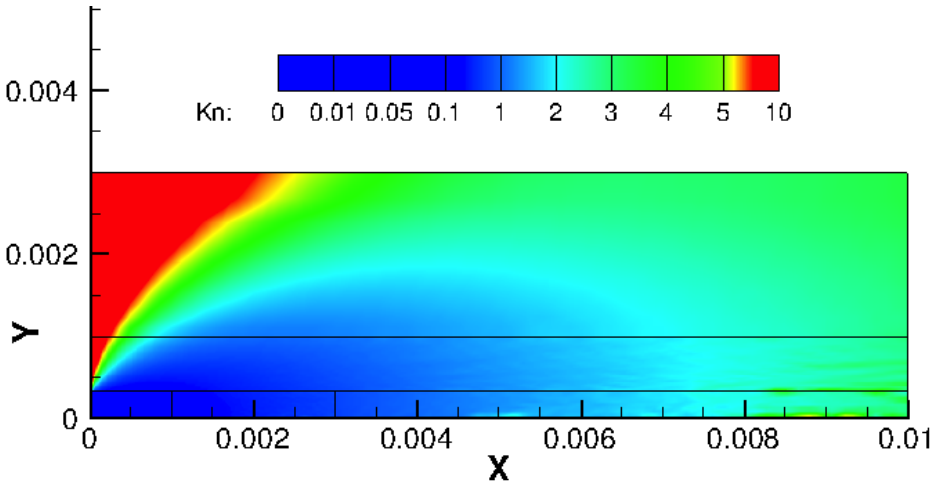

Figure 5.5: Log10 of number density contour in a supersonic underexpanded jet

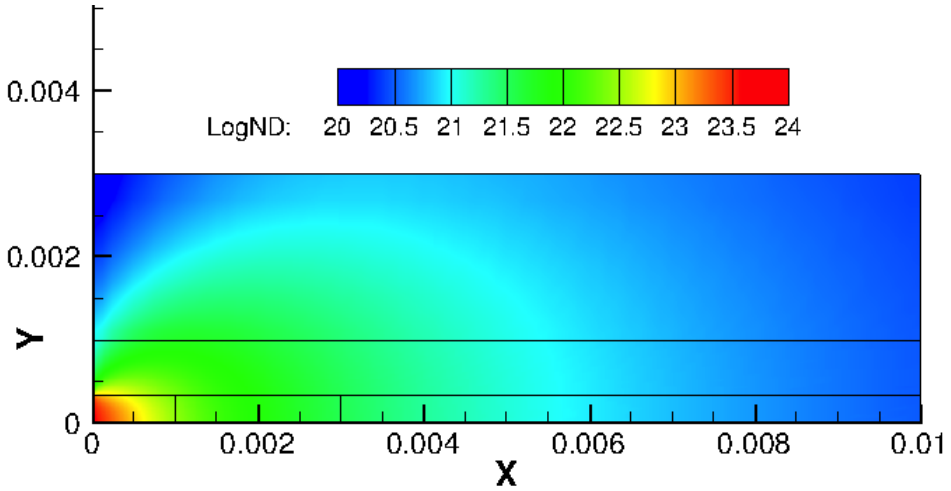

Figure 5.6: Downstream centerline number density in log10 format

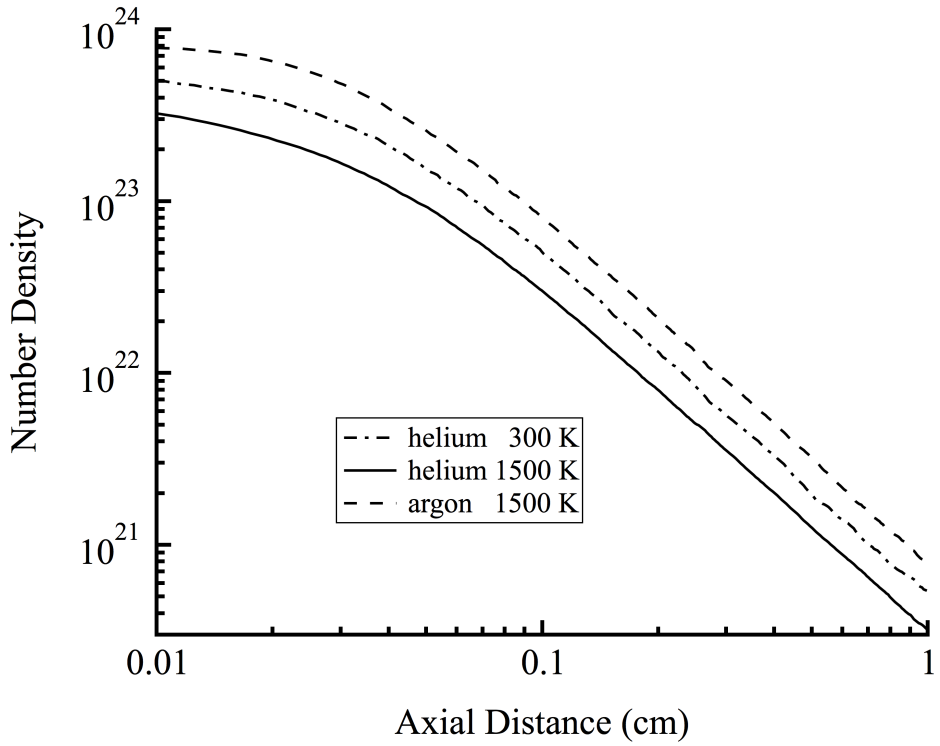

Figure 5.7: Downstream centerline temperature

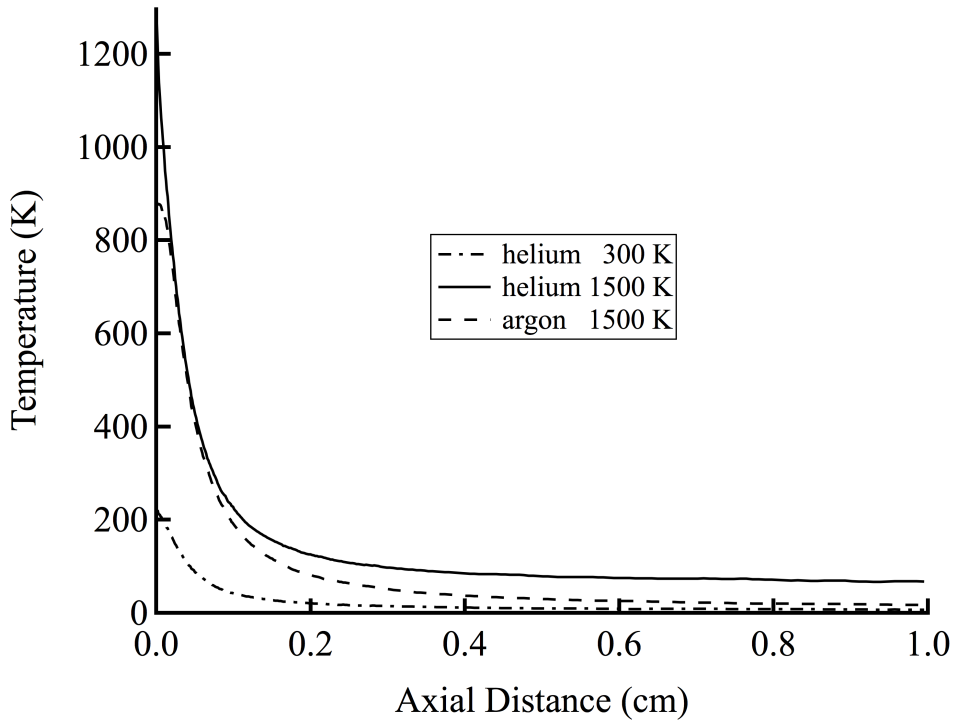

Figure 5.8: Downstream centerline velocity

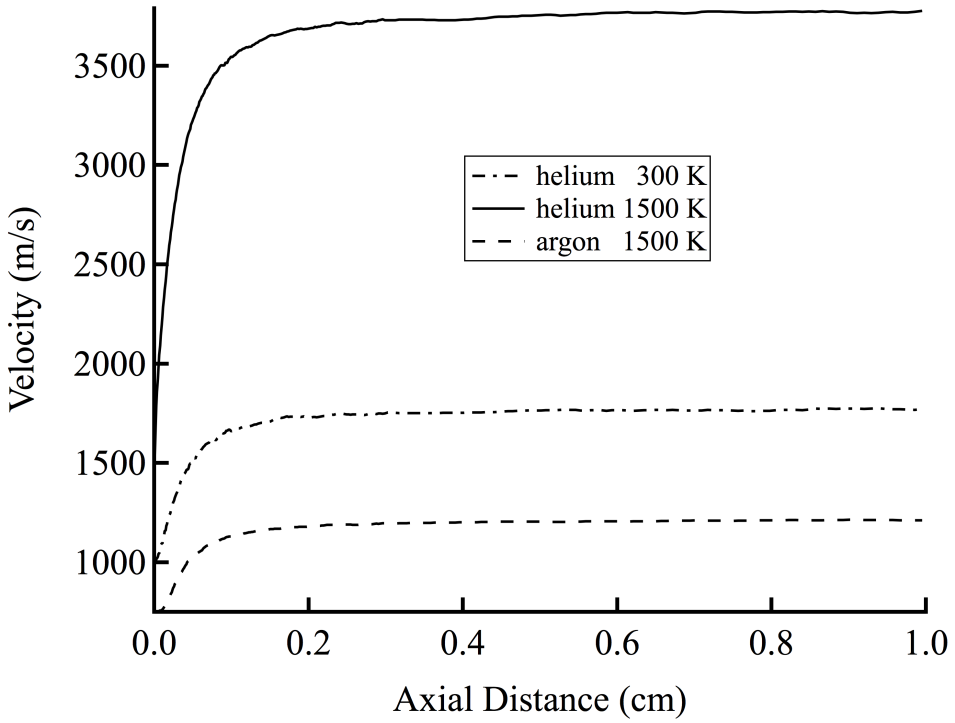

Figure 5.9: Downstream centerline Mach number

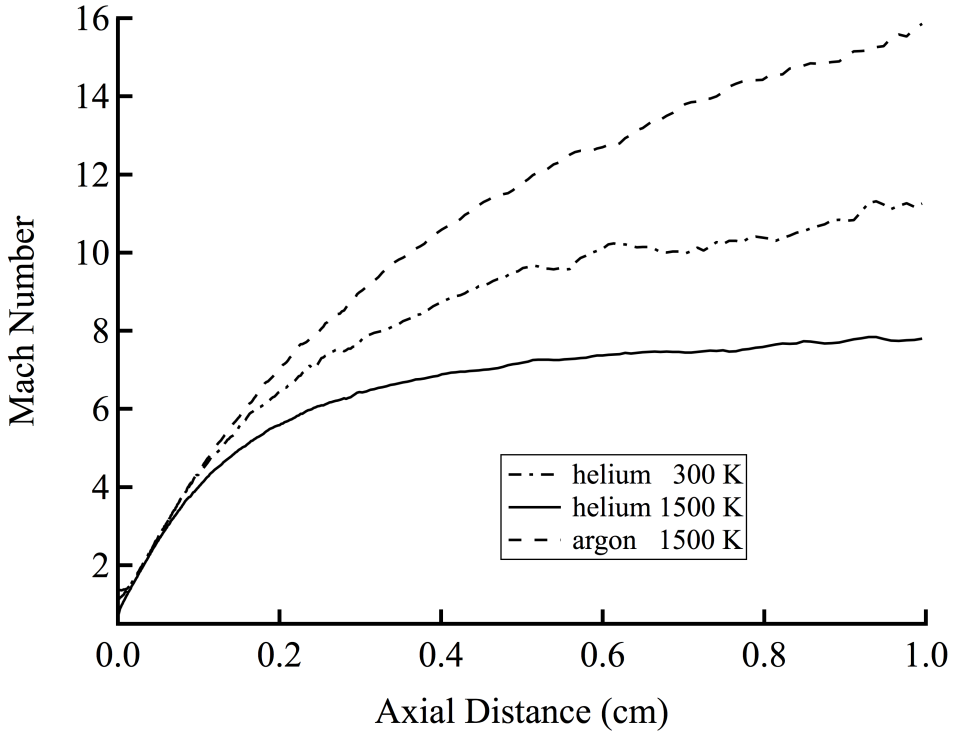

Figure 5.10: Terminal velocity validation by experiment

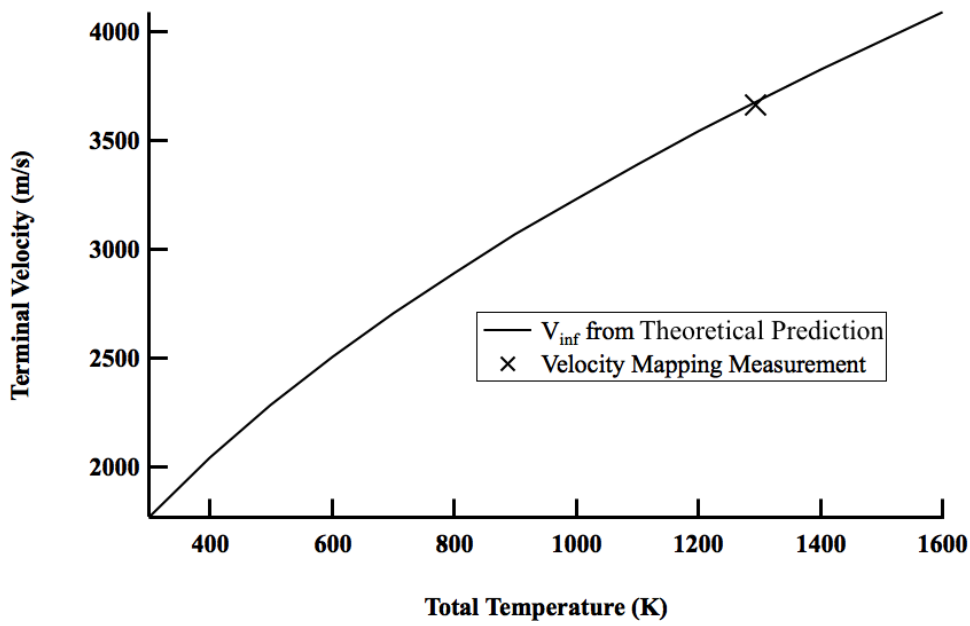

5.2 Ideal molecular beam performance

In the PIMS system, the downstream jet expansion is filtered by a skimmer. A molecular beam is formed after the skimmer and flows into the diagnostic chamber. Of course, one would always want to analyze an unperturbed beam source in order to keep the velocity distribution of the molecules upstream and prevent interference from the skimmer. Clearly molecules hitting the skimmer are likely to bounce back to the jet source and perturb the beam. Previous work [4, 11] has shown that strong skimmer interference can perturb the original beam properties particularly when the skimmer is put too close to the reactor. Cases include normal shock wave ahead of the skimmer entrance [4], and attached shock on the outside of the skimmer [45] or inside the skimmer [12]. To analyze these effects, a schematic plot is drawn in Fig. 5.11. Some of the important parameters include the distance between nozzle exit and skimmer entry l_s, the quitting surface radius l_1, the reactor diameter D, the skimmer radius r_s, and the distance from the skimmer to the diagnostic spot x. Here and below, we denote properties at the "quitting surface" with subscript '1' and properties at the skimmer with 's'.

Figure 5.11: Important parameters impacting beam performance (adapted from [4])

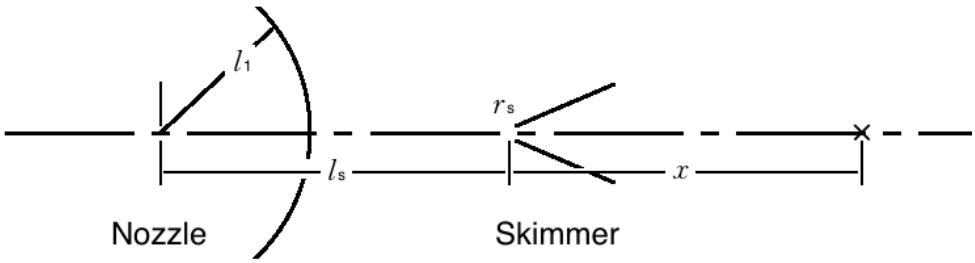

In the experiment, the position of the skimmer is a very important parameter. One would like the skimmer to be put in a position such that the flow passing through is in the free molecular region. This can be judged by computing the Knudsen number Kn_s at the skimmer entry based on the skimmer diameter. Another important parameter often used in analytical solutions is the "speed ratio" s, which is defined as the ratio of the axial velocity U to the most probable speed

$\sqrt{2RT}$:

$$s = \frac{U}{\sqrt{2RT}} \tag{5.2}$$

where R is the gas constant and T is the local translational temperature. We would assume the gas is in translational equilibrium within a certain distance downstream.

One often measures the beam intensity or flux, I, on the centerline in the experiment. If the source beam is ideally effusive, then the intensity at the spot location is given as [4]:

$$I_{effusive} = n_s \frac{\pi r_s^2}{4} \left(\frac{8kT_s}{\pi m} \right)^{\frac{1}{2}} \frac{1}{\pi x^2} \tag{5.3}$$

For a supersonic source beam, when the speed ratio s_1 is greater than 4, one can deduce a general expression by simplification as:

$$I_{supersonic} \cong n_s (l_s/l_1)^2 \pi r_s^2 u_1 \frac{1}{\pi x^2} (s_1^2 + \frac{3}{2}) \tag{5.4}$$

Using the Mach number at the "quitting surface" M_1, this can be rewritten as:

$$I_{supersonic} \cong n_s (l_s/l_1)^2 \pi r_s^2 u_1 \frac{1}{\pi x^2} (\frac{1}{2} \gamma M_1^2 + \frac{3}{2}) \tag{5.5}$$

Another interference comes from the background gas penetration when the skimmer is put far away from the source. Under this condition, the beam attenuation effect starts rising and beam signals at the diagnostic spot might be damped as indicated by Eqn. 5.5. In summary, from a design perspective, it would be very helpful to know an optimized skimmer location. However, the impacts of the skimmer and background gas are unlikely to be quantitatively obtained without detailed simulations. This is the reason we carry out the simulations in the following sections.

5.3 DSMC simulation of the skimmer interference

For such a complicated flow field, a sophisticated code would be required. For example, a fixed mesh will not be able to capture the flow field variation downstream. Thus a code with a self-adaptive mesh function will be favored. In our research, we use Bird's DS2V program to simulate the flow and study the impacts of skimmer interference and analyze the statistics. The skimmer

interference is mainly decided by three factors: (1) the distance between the reactor exit and the skimmer entry l_s; (2) the skimmer entry diameter D_s; and (3) the absorptivity of the skimmer surface α_s. Both helium and argon are simulated to study the impact of the carrier gas. The real skimmer shape and its dimensions are shown in Fig. 1.3. In our simulation, an approximate geometry of the skimmer is used, as shown in Fig. 5.12. Both the inner and the outer surfaces are conical. The entry diameter D_s can be varied. The other dimensions of the skimmer are fixed as the following: thickness $t_s = 5$ mm, length $x_s = 2.5$ cm and exit diameter $D_0 = 3$ cm.

Figure 5.12: Cone shaped skimmer in molecular beam simulations

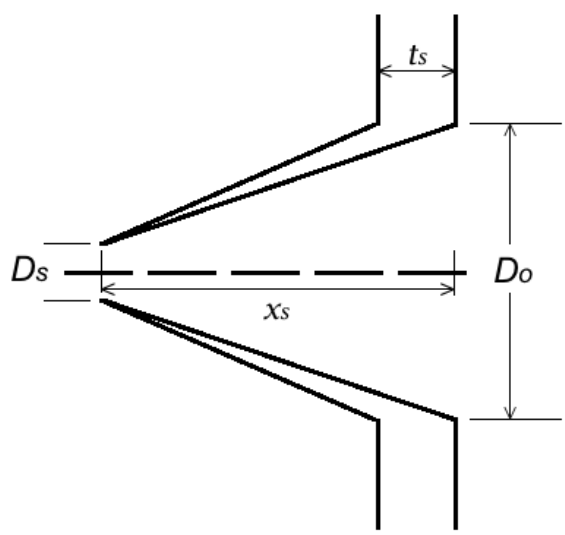

The adsorption coefficient α_s of the skimmer surface may be varied from zero to unity, allowing us to observe the strongest to the slightest skimmer interferences. All the collisions with the skimmer surface are considered to be diffuse reflections. The skimmer temperature is fixed at $T_s = 300$ K. The other bounding surfaces are set with an adsorption coefficient of unity mimicking the vacuum boundaries. Fig. 5.13 is a log10 of the number density contour and shows an example where the skimmer is placed 2 cm downstream of the reactor and the flow domain is 6 cm in length and 3 cm in radius. In this case, the entry diameter D_s is 1 mm. A flow entry boundary is applied at the left lower corner. The stream velocity, number density and temperature are the area-weighted averages of the properties on the reactor exit surface from the CFD simulations. Three cycles

of mesh adaption are applied to capture the local density variation during the simulation. In all cases, 600 MB memory is allocated for the computation. As before, the centerline number density, velocity and temperature are compared.

Figure 5.13: Log10 of number density contour

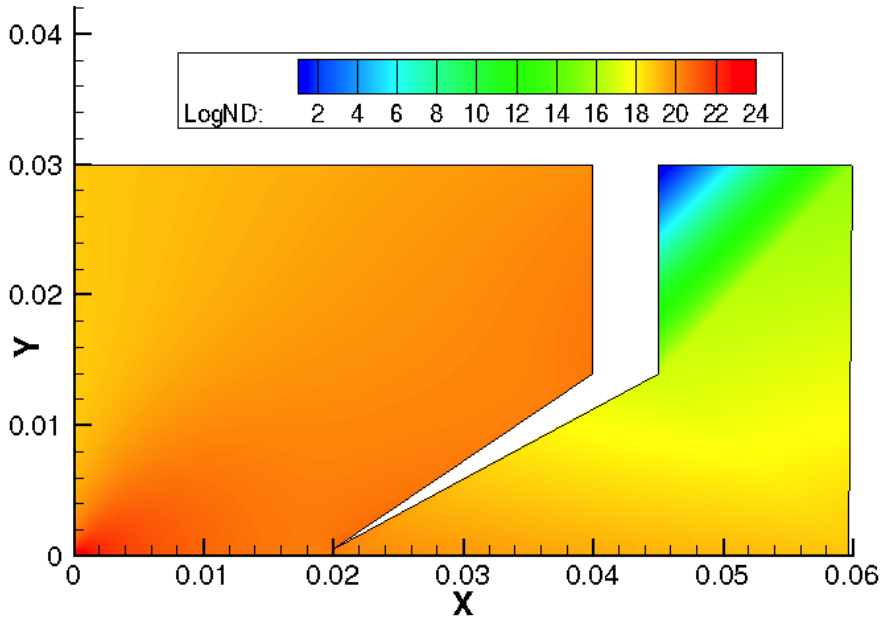

5.3.1 Reactor-skimmer distance l_s

To study the reactor-skimmer distance impact, we vary the distance l_s value between 1.0 cm and 2.0 cm. The skimmer entry diameter D_s is set as 1 mm and an adsorption coefficient of $\alpha_s = 0$ is used. The flow entry data are taken from the case of 1500 K with helium as the carrier gas in reactor #1. Converted to microscopic information, the inlet stream has a velocity of 1922.74 m/s, a temperature of 1009 K and a number density of 1.9666 $\times 10^{23}$ #/m^3.

The number density falls off quadratically against distance as if the skimmer is nonexistent. The number density distribution profiles for both cases are nearly the same as shown in Fig. 5.14. On the other hand, there are noticeable interferences on the velocity and temperature developments as can be seen from Fig. 5.15 and 5.16. At a certain location ahead of the skimmer, the flow acceleration stops and starts decreasing to a minimum value before it reaches the skimmer entry. The further

Figure 5.14: Centerline number vs. distance with different reactor-skimmer distance

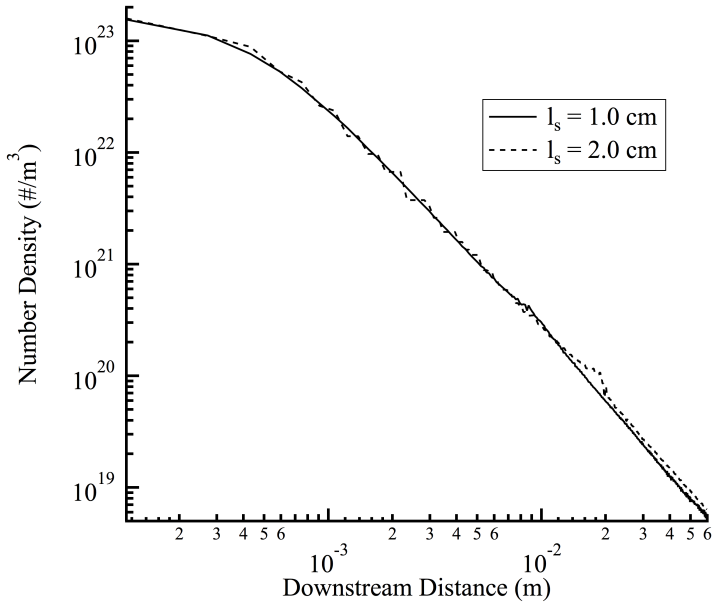

Figure 5.15: Centerline velocity vs. distance with different reactor-skimmer distance

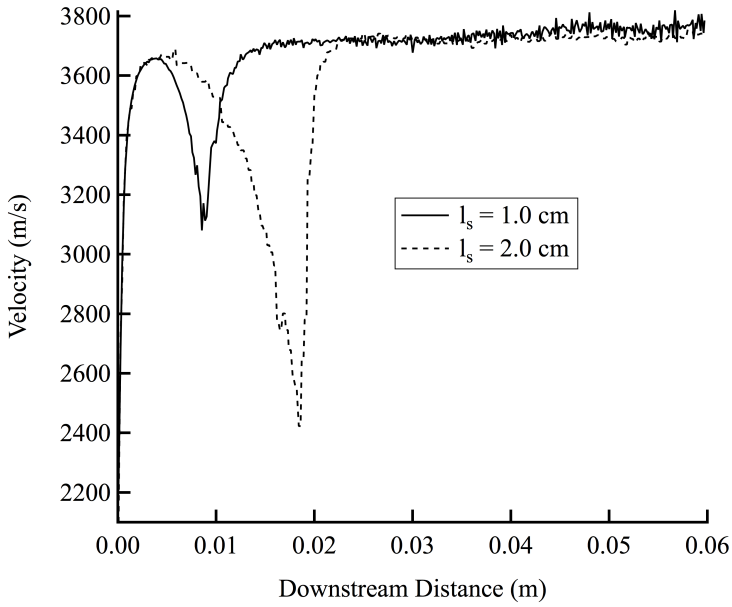

Figure 5.16: Centerline temperature vs. distance with different reactor-skimmer distance

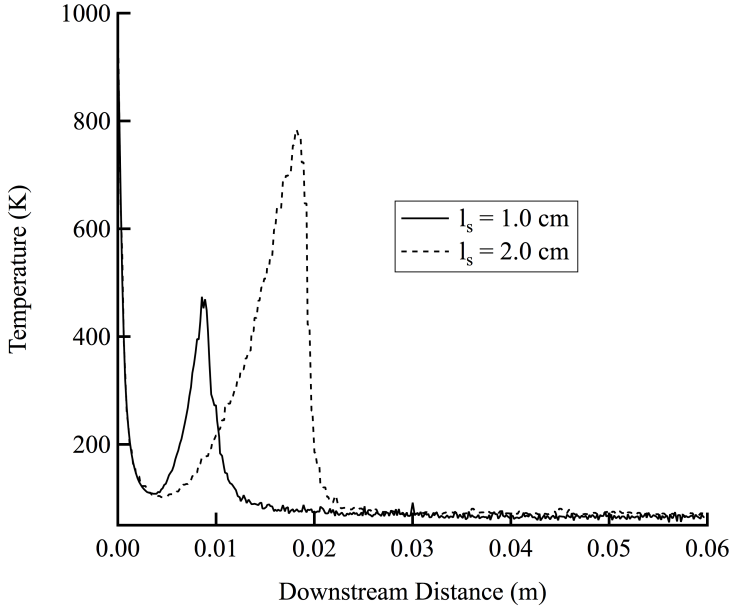

the skimmer is put downstream, the greater this velocity decrease is found. This means that the molecules bouncing back from the skimmer surface are interacting with the molecules flying along the beam center. After the flow passes through the skimmer entry, the velocity quickly rises up and eventually reaches a limit value, i.e. terminal velocity. As one can tell, the same limit values are reached for both cases. The skimmer location does not affect it. The velocity development history is also reflected in the temperature plot. Maximum local temperatures are found before the skimmer entry and the same asymptotic value is reached for different skimmer locations.

5.3.2 Skimmer entry diameter D_s

The skimmer entry diameter impact is studied by varying D_s among 1 mm , 2 mm, and 3 mm. In all three cases, the skimmer is put 2 cm downstream of the reactor and an adsorption coefficient of $\alpha_s = 0$ is used. The flow entry data are taken from the case of 1500 K with helium as the carrier gas in reactor #1.

Figure 5.17: Centerline number density vs. distance with different skimmer entry diameter

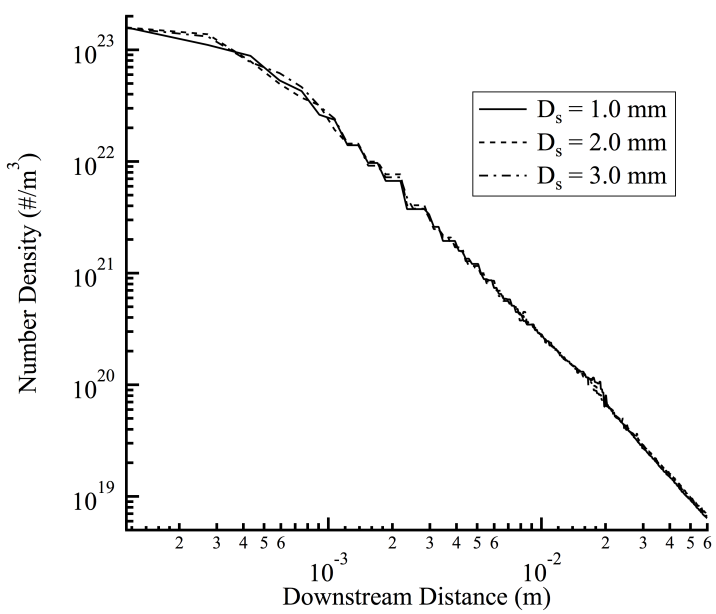

When the entry diameter increases, the skimmer becomes more slender. Molecules bouncing back from the skimmer tend to bounce more outward. At the same time, a wider beam core is

Figure 5.18: Centerline velocity vs. distance with different skimmer entry diameter

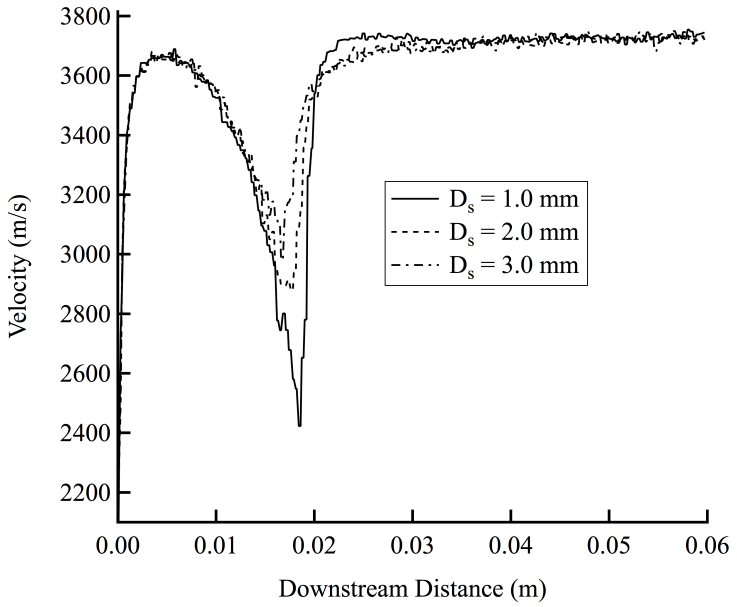

Figure 5.19: Centerline temperature vs. distance with different skimmer entry diameter

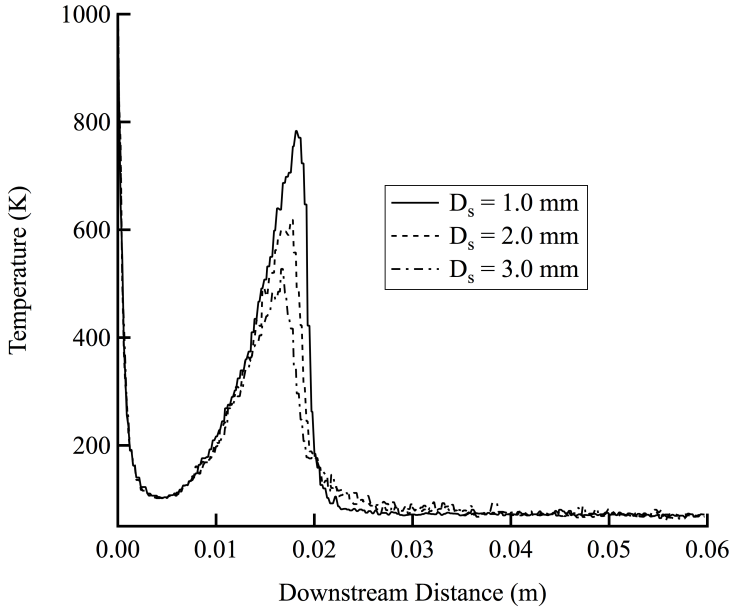

formed since more fluxes are allowed to pass through the skimmer. Thus, one would expect less impact on the molecules along the beam center. This is verified by the centerline plots of the number density, velocity, and temperature shown in Fig. 5.17 to Fig. 5.19. The number density profiles of all three diameters are nearly the same. Although smaller diameter results a bigger interaction ahead of the skimmer, the same terminal velocity and temperature are reached eventually at a certain distance behind the skimmer in all three cases.

5.3.3 Adsorption coefficient α_s

The adsorption coefficient α_s is sometimes also referred to as the sticking coefficient. It represents the fraction of molecules sticking on the wall after the collision. A unity adsorption coefficient behaves exactly as a vacuum boundary where molecules colliding with the wall are deleted from the computation. An adsorption coefficient of zero reflects all the molecules hitting on the wall. To study the impact of the absorptivity, we vary the coefficient α_s value among 0, 0.5 and 1.0. The skimmer is put 2 cm downstream of the reactor with an entry diameter D_s fixed at 1 mm. The flow entry data are taken from the case of 1500 K with helium as the carrier gas in reactor #1.

A better absorptivity means less molecules will be bounced back to the beam and therefore a weaker interaction. From the centerline number density plot in Fig. 5.20, we can find that the absorptivity does not affect the number density distribution. On the other hand, as the absorptivity gets stronger, flow velocity and temperature become less affected, as shown in Fig. 5.21 and Fig. 5.22. At $\alpha_s = 1.0$, the skimmer surface behaves as a vacuum boundary and the beam properties are not affected at all.

5.3.4 Carrier gas

Both helium and argon are often used as the carrier gas. This is why simulations are carried out using the two gases and comparisons are made. For both gases, the flow entry data are taken from the case of 1500 K in reactor #1. For argon, the microscopic stream properties are velocity

Figure 5.20: Centerline number density vs. distance with different adsorption coefficient

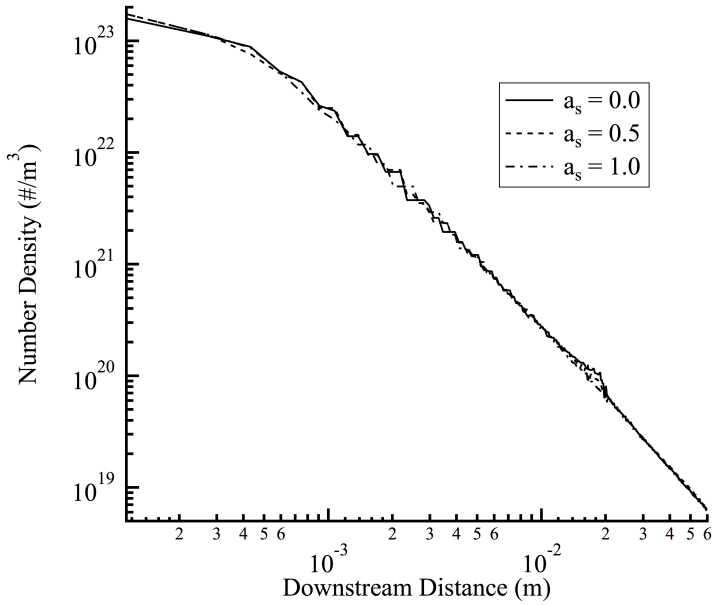

Figure 5.21: Centerline velocity vs. distance with different adsorption coefficient

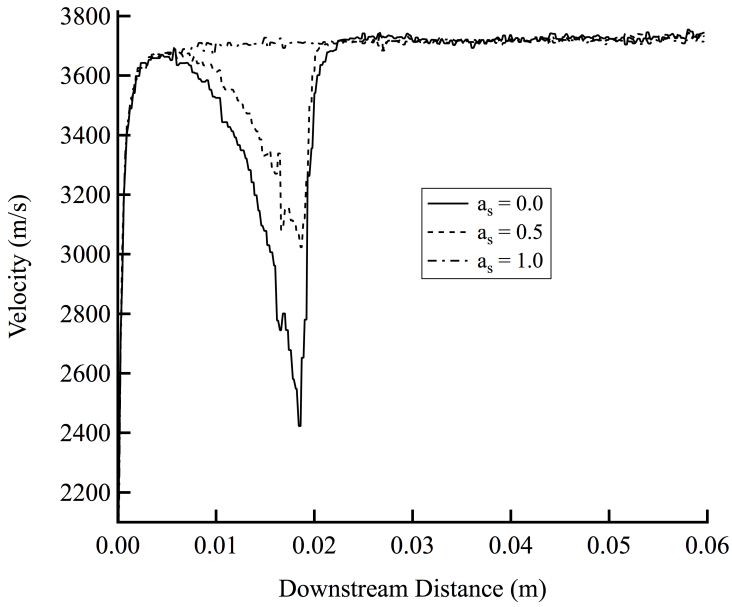

Figure 5.22: Centerline temperature vs. distance with different adsorption coefficient

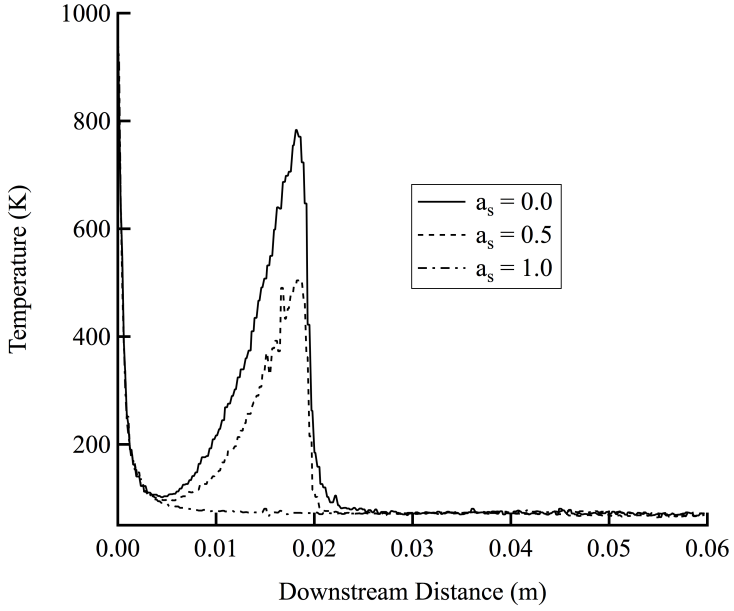

660.78 m/s, temperature 1037 K, and number density 6.3698 $\times 10^{23}$ #/m^3. The entry diameter of $D_s = 1$ mm is used and the reactor skimmer distance is $x_s = 2$ cm. Centerline number density, velocity and temperature are shown in Fig. 5.23 to Fig. 5.25.

Figure 5.23: Centerline number vs. distance with different carrier gas

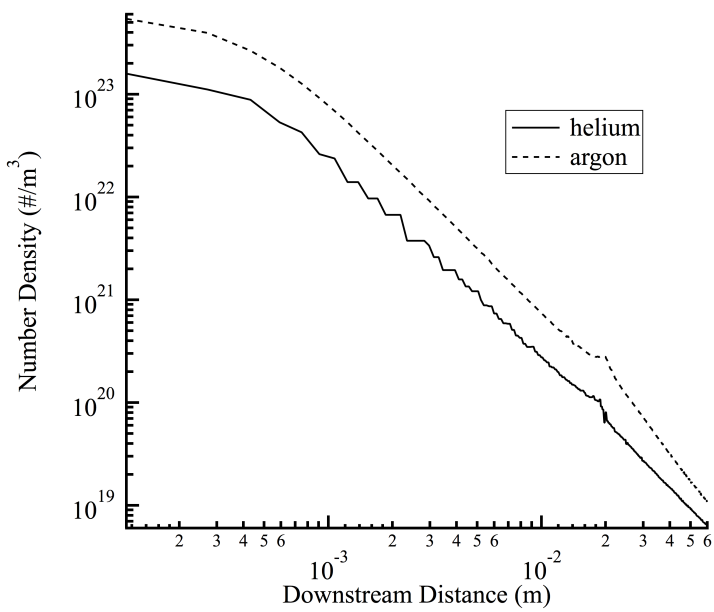

As can be seen from Fig. 5.23, the argon case definitely shows a better continuity as its number density is about five times that of the helium case. In both cases, the beam velocity and temperature are affected by the skimmer and quickly recovers after the skimmer. Faster terminal velocity is reached when the lighter carrier gas species is used, as shown in Fig. 5.24.

5.4 Seeded species in carrier gas

In our experiment, we often mix a dilute fraction of biomass species into the carrier gas. The seeded biomass species will have the same velocities as the carrier gas species within the continuum expansion. When the flow reaches the free molecular expansion, there will not be enough collision frequency to maintain the thermodynamic equilibrium and species with different molecular weights will behave differently. They start to differentiate from each other due to the rarefaction effect.

In the parallel direction, lighter species travel faster than the heavier ones. This phenomenon

Figure 5.24: Centerline velocity vs. distance with different carrier gas

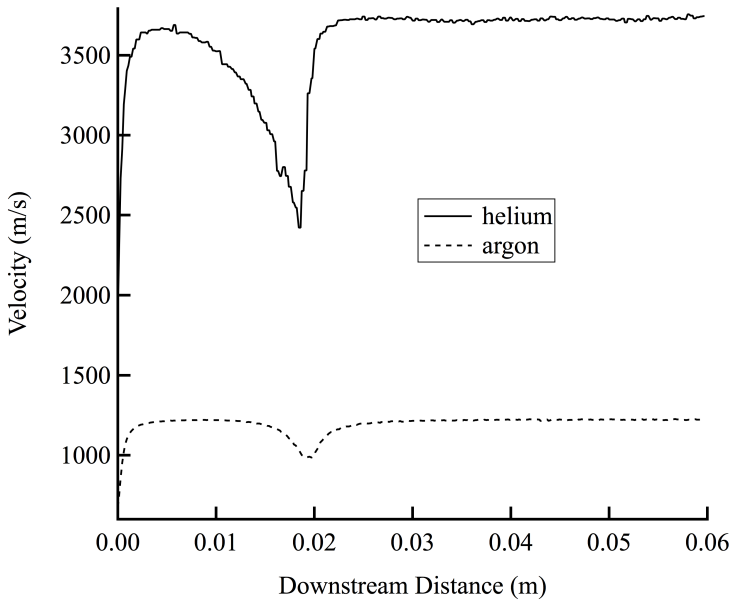

Figure 5.25: Centerline temperature vs. distance with different carrier gas

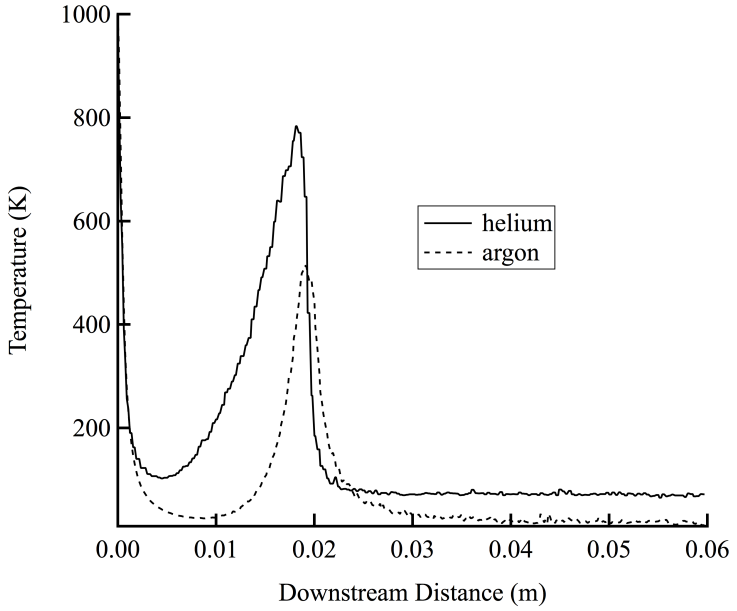

is also often called "velocity slippage" [63]. In our experiment, the carrier gas is usually the lighter species and has a faster speed. Thus, biomass species are accelerated during this process. In the perpendicular direction, thermal velocity is proportional to the square root of the molecular weight [4]. Heavier molecules tend to stay in the beam center while the lighter ones travel more broadly. This leads to a higher concentration of the heavier species along the centerline. The variation of the species concentrations along the centerline is a very interesting phenomenon. To quantify this, in experiment, one often derives a mass-discrimination factor A_i for species i within carrier gas species j. It is related as:

$$\frac{I_i(E_i)}{I_j(E_j)} = A_i \frac{Q_i(E_i)}{Q_j(E_j)} \frac{X_i}{X_j} \tag{5.6}$$

Here $I_i(E_i)$ is the intensity of species i measured at electron energy E_i. $Q_i(E_i)/Q_j(E_j)$ stands for the ionization cross section ratio of carrier gas species j. And X_i/X_j is the mole fraction ratio in the feeding which will be known in advance.

In simulation, one directly models the species distribution. Therefore, the variation of species mole fractions can be obtained. To investigate the seeded species behavior in the carrier gas, a mixture expansion with 1% ideal oxygen, 1% xenon carried by 98% helium is simulated. The properties of these three species are listed in Table 5.2. Ideal oxygen has a constant rotational number of $Z_r = 5$ while its vibrational energy is not considered.

Table 5.2: Physical properties of helium, xenon and oxygen used in mixture expansion

Properties (unit)	Helium	Xenon	Ideal Oxygen
Reference diameter (m)	2.33×10^{-10}	5.74×10^{-10}	4.07×10^{-10}
Reference temperature (K)	273	273	273
Viscosity-temp. power ω	0.66	0.85	0.77
Molecular mass (kg)	6.65×10^{-27}	2.18×10^{-25}	5.31×10^{-26}
Rotational deg. of freedom	0	0	2

To approximate the expansion scenario in the pumping system, we model the flow in a domain with a length of 30 cm and a radius of 15 cm. The skimmer is put 2 cm downstream of the reactor exit, which separates the domain into a source chamber and a diagnostic chamber. The skimmer

has an entry diameter of $D_s = 2$ mm and is assumed to have an adsorption coefficient of $\alpha_s = 0$. Molecular collisions on the skimmer are fully diffuse. Inlet flow entry data are taken from the case of 1500 K with helium as the carrier gas in reactor #1. Converted to microscopic information, this is a stream with a velocity of 1922.74 m/s, a temperature of 1009 K and a number density of 1.9666 $\times 10^{23}$ #/m^3.

Figure 5.26: Log10 of number density contour in a pumping system

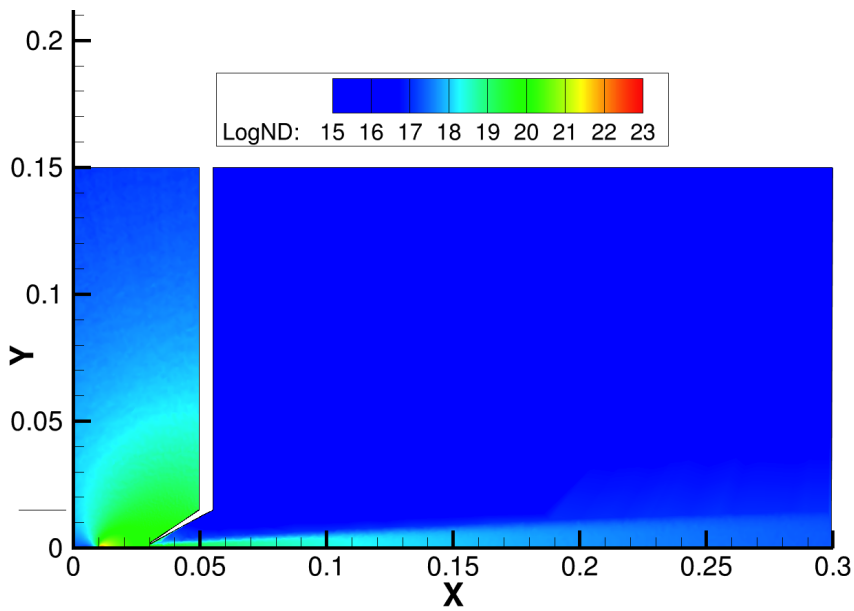

The general scenario of this simulation is shown in Fig. 5.26, where the number density distribution is presented in log10 format. As we can tell, most of the molecules in the supersonic jet hit on the skimmer and bounce back to the source chamber. The remaining molecules pass through the skimmer and form a molecular beam. The beam continues its expansion in the diagnostic chamber and becomes more and more diminished.

The "velocity slippage" phenomenon is reflected in Fig. 5.27 and 5.28. As one can see, within the continuum expansion region, the mole fractions of the heavier seeded species of O_2 and Xe rapidly increase while the lighter carrier gas species of He decreases. As the expansion enters the free molecular flow region, the mole fractions become steady. The species mole fractions of O_2, Xe, and He are about 4%, 16%, and 80%, respectively. The mole fraction ratio of O_2 and Xe are

Figure 5.27: Mole fractions of O_2, Xe and He along centerline

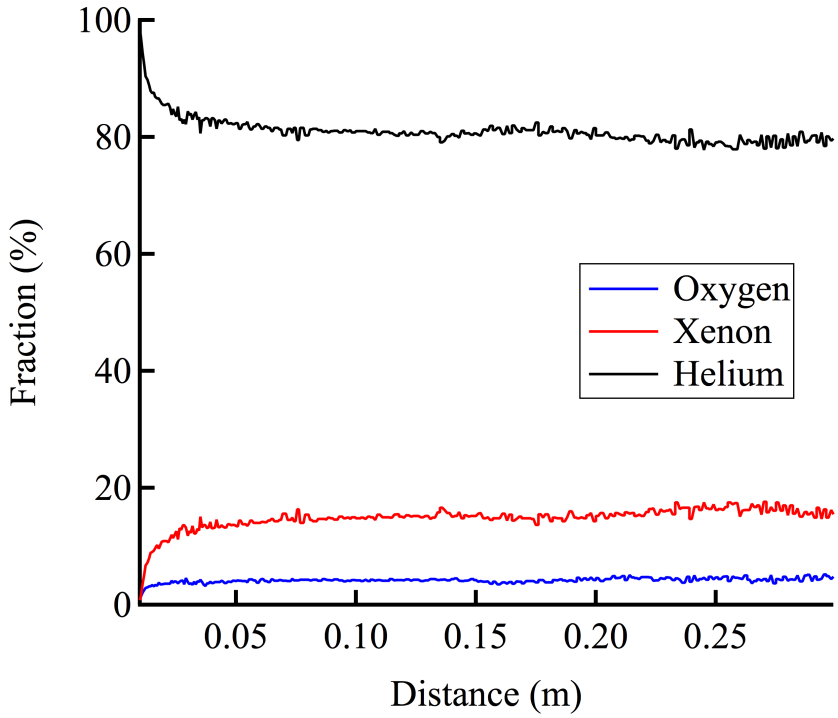

Figure 5.28: Mole fraction ratio of O_2 and Xe vs. He along centerline

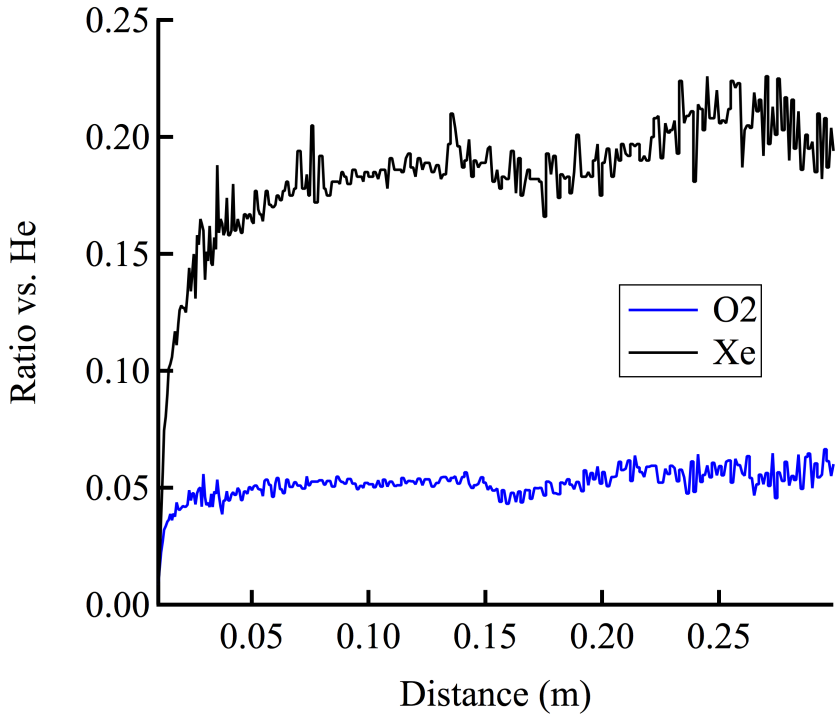

generally proportional to their molecular weight, which is consistent with the prediction made by Anderson [4].

Chapter 6

Conclusion and Future Work

6.1 Conclusion

In this thesis, we have carried out detailed simulations about the flow field development within the reactor and vacuum chamber. Flow field variations under different operating conditions and carrier gases are investigated. Within the reactor section, the CFD method is used. We have found that noncontinuum flow phenomena do happen if high heating temperatures and low mass flow rates are applied. For the cases with less severe rarefied conditions $Kn < 0.1$, a slip boundary condition can be used to model the velocity slip and temperature jump near the reactor exit. Appropriate momentum and thermal accommodation coefficients are selected to match the mass flow rate and upstream pressure measured in the experiment. For the flow in the vacuum chamber, the DSMC method is used to model the rarefied gas dynamics. For our experiment, the skimmer is put within the free molecular flow region which is far away from the reactor exit. The skimmer is found to have some interference on the beam temperature and velocity distribution ahead of the skimmer entry but eventually recovers to terminal values in the supersonic expansion. To connect the CFD and DSMC solutions, we have applied the zonally decoupled CFD/DSMC method. A state based reservoir boundary is used instead of the traditional emitting surface boundary.

6.2 Future Work

Based on the current progress of the project, there are three major major topics to be addressed in future research, including:

- a reacting flow CFD code

  The final aim of the project is to be able to simulate pyrolysis reacting flow of the dilute biomass species. A typical process might include over 10 species and 20 reactions. The current CFD can only solve for a single species flow which is very elementary. To investigate the pyrolysis reactions, a sophisticated reacting flow mechanism needs to be built.

- a more sophisticated DSMC code

  As can be seen in Chapter 5, our current homemade DSMC code does not have the self-adaptive mesh function. This deficiency greatly inhibits the simulation of the skimmer interference. On the other hand, DS2V does not have the species weighting technique which is a big disadvantage in simulating mixtures with dilute seeded species. Thus a combination of self-adaptive mesh and species weighting needs to be implemented in the DSMC code.

- a fully coupled 2D CFD/DSMC

  Our current hybrid code can only simulate the scenario with acceptable continuous flow conditions. This is because the zonally decoupled CFD/DSMC method requires the flow to be both continuum and supersonic on the split interface. However, in the experiments, we also often run cases with much less mass flow rate, e.g. $\dot{V} \approx 25$ sccm. The low mass flow rate will lead to poor continuum conditions within the reactor. This is validated by the experimental measurement of the terminal velocities. For these cases, a zonally decoupled CFD/DSMC is inappropriate. Instead, a fully coupled code needs to be used. The transition from continuum to rarefied flow will happen within the reactor and information has to be correctly transferred to both domains.

Bibliography

[1] Giannandrea Abbate, Chris R Kleijn, and Barend J Thijsse. Validation of a hybrid navier-stokes/dsmc method for multiscale transient and steady-state gas flows. International Journal for Multiscale Computational Engineering, 6(1), 2008.

[2] Francis J Alexander, Alejandro L Garcia, and Berni J Alder. Cell size dependence of transport coefficients in stochastic particle algorithms. Physics of Fluids (1994-present), 10(6):1540–1542, 1998.

[3] J.B. Anderson. Inviscid freejet flow with low specific heat ratios. AIAA Journal, 10:112, 1972.

[4] J.B. Anderson, R.P. Andres, and J.B. Fenn. 8. supersonic nozzle beams. Advances in Chemical Physics, 10:275–317, 1966.

[5] Harry Ashkenas and Frederick S Sherman. Experimental methods in rarefied gas dynamics. Jet Propulsion Laboratory, California Institute of Technology, 1966.

[6] G.K. Batchelor. An Introduction to Fluid Mechanics. Cambridge University Press, 1967.

[7] K. Beijerinck and N. Verster. Absolute intensities and perpendicular temperatures of supersonic beams of polyatomic gases. Physica B and C, 111:327–352, 1981.

[8] E Bich, J Millat, and E Vogel. The viscosity and thermal conductivity of pure monatomic gases from their normal boiling point up to 5000 k in the limit of zero density and at 0.101325 mpa. Journal of physical and chemical reference data, 19(6):1289–1305, 1990.

[9] K. Bier and B. Schmidt. On the form of shock waves in expanding free jets. Z. Angew, 13:493, 1961.

[10] G. A. Bird. Molecular Gas Dynamics and the Direct Simulation of Gas Flows. Oxford Science Publications, 1994.

[11] GA Bird. Molecular gas dynamics, Clarendon. Oxford, 1976.

[12] G.A. Bird. Transition regime behavior of supersonic skimmers. Phys. Fluids, 19:1486, 1978.

[13] GA Bird. Recent advances and current challenges for dsmc. Computers & Mathematics with Applications, 35(1):1–14, 1998.

[14] R.B. Bird, W.E. Stewart, and E.N. Lightfoot. Transport Phenomena. Wiley, NYC, 1960.

[15] Jiri Blazek. Computational Fluid Dynamics: Principles and Applications: Principles and Applications. Elsevier, 2001.

[16] J. A. Blush, H. Clauberg, D. W. Kohn, D. W. Minsek, X. Zhang, and P. Chen. Photoionization mass and photoelectron-spectroscopy of radicals, carbenes, and biradicals. Accounts Chem. Res., 25(9):385–392, 1992.

[17] Iain D Boyd. Conservative species weighting scheme for the direct simulation monte carlo method. Journal of Thermophysics and Heat Transfer, 10(4):579–585, 1996.

[18] Iain D Boyd. Predicting breakdown of the continuum equations under rarefied flow conditions. 2003.

[19] Kenneth S Breuer, Edward S Piekos, and David A Gonzales. Dsmc simulations of continuum flows. In AIAA, Thermophysics Conference, 30 th, San Diego, CA, 1995.

[20] Hadley M. Cave. Development of modelling techniques for pulsed pressure chemical vapour deposition (PP-CVD). PhD thesis, University of Canterbury, 2008.

[21] O. L. Chapman and C. L. McIntosh. Cyclopentadienone. Journal of the Chemical Society D: Chemical Communications, (14):770–771, 1971.

[22] G Chen, ID Boyd, SE Roadman, and JR Engstrom. Monte carlo analysis of a hyperthermal silicon deposition process. Journal of Vacuum Science & Technology A, 16(2):689–699, 1998.

[23] P. Chen. Supersonic Jets of Organic Radicals. John Wiley, Cambridge, UK, 1994.

[24] P. Chen, S. D. Colson, W. A. Chupka, and J. A. Berson. Flash pyrolytic production of rotationally cold free-radicals in a supersonic jet - resonant multiphoton spectrum of the ^{3}P $^2A_2''$ origin band of CH_3. Journal of Physical Chemistry, 90(11):2319–2321, 1986.

[25] P. Chen, J. B. Pallix, W. A. Chupka, and S. D. Colson. Resonant multiphoton ionization spectrum and electronic-structure of CH radical - new states and assignments above 50 000 cm^{-1}. Journal of Chemical Physics, 86(2):516–521, 1987.

[26] S.H.P. Chen and S.C. Saxena. Thermal conductivity of argon in the temperature range 350 to 2500 k. Molecular Physics, 29(2):455–466, 1975.

[27] P.V. Danckwerts. Continuous flow systems: distribution of residence times. Chemical Engineering Science, 2:1–13, 1953.

[28] RA Dawe and EB Smith. Viscosities of the inert gases at high temperatures. The Journal of Chemical Physics, 52(2):693–703, 1970.

[29] Ansys Fluent. 12.0 theory guide. Ansys Inc, 5, 2009.

[30] Alejandro L Garcia and Berni J Alder. Generation of the chapman–enskog distribution. Journal of Computational Physics, 140(1):66–70, 1998.

[31] Alejandro L Garcia, John B Bell, William Y Crutchfield, and Berni J Alder. Adaptive mesh and algorithm refinement using direct simulation monte carlo. Journal of computational Physics, 154(1):134–155, 1999.

[32] Jyothish D. George. A combined CFD-DSMC method for numerical simulation of nozzle plume flows. PhD thesis, Cornell University, 2000.

[33] BE Glass and Peter A Gnoffo. A 3-d coupled cfd-dsmc solution method with application to the mars sample return orbiter. In AIP CONFERENCE PROCEEDINGS, pages 723–729. IOP INSTITUTE OF PHYSICS PUBLISHING LTD, 2001.

[34] Andreas Gross and Hermann F Fasel. Numerical investigation of supersonic flow for axisymmetric cones. Mathematics and Computers in Simulation, 81(1):133–142, 2010.

[35] Nicolas G Hadjiconstantinou. Analysis of discretization in the direct simulation monte carlo. Physics of Fluids (1994-present), 12(10):2634–2638, 2000.

[36] Nicolas G Hadjiconstantinou, Alejandro L Garcia, Martin Z Bazant, and Gang He. Statistical error in particle simulations of hydrodynamic phenomena. Journal of Computational Physics, 187(1):274–297, 2003.

[37] Nathalie Herlin, Michel Lefebvre, Michel Pealat, and Jerome Perrin. Investigation of the chemical vapor deposition of silicon carbide from tetramethylsilane by in situ temperature and gas composition measurements. The Journal of Physical Chemistry, 96(17):7063–7072, 1992.

[38] M.W. Jarvis, J.W. Daily, H.-H. Carstensen, A.M. Dean, S. Sharma, D.C. Dayton, D.J. Robichaud, and M.R. Nimlos. Direct detection of products from the pyrolysis of 2-phenethyl phenyl ether. Journal of Physical Chemistry A, 115:428–438, 2011.

[39] A Kantrowitz and J. Grey. Review of Scientific instruments, 22:32, 1951.

[40] CR Kleijn, R Dorsman, KJ Kuijlaars, M Okkerse, and H Van Santen. Multi-scale modeling of chemical vapor deposition processes for thin film technology. Journal of Crystal Growth, 303(1):362–380, 2007.

[41] F La Torre, S Kenjereš, J-L Moerel, and CR Kleijn. Hybrid simulations of rarefied supersonic gas flows in micro-nozzles. Computers & Fluids, 49(1):312–322, 2011.

[42] Olivier Leroy, Jérôme Perrin, Jacques Jolly, Michel Péalat, and Michel Lefebvre. Thermal accommodation of a gas on a surface and heat transfer in cvd and pecvd experiments. Journal of Physics D: Applied Physics, 30(4):499, 1997.

[43] O. Levenspiel. Chemical Reaction Engineering. Wiley Series in Chemical Engineering, 1972.

[44] J Clerk Maxwell. On stresses in rarified gases arising from inequalities of temperature. Philosophical Transactions of the royal society of London, 170:231–256, 1879.

[45] D.R. Miller. Free jet sources. In Atomic and Molecular Beam Methods, chapter 2, pages 14–53. Oxford University Press, 1988.

[46] C.L.M.H. Navier. Memoire sur les lois du mouvement des fluides. Mem. Acad. Sci. Inst. France, pages 389–440, 1822.

[47] Ove Nilsson, Harald Mehling, Ronny Horn, Jochen Fricke, Rainer Hofmann, Stephan G Müller, Robert Eckstein, and Dieter Hofmann. Determination of the thermal diffusivity and conductivity of monocrystalline silicon carbide (300-2300 k). High Temperatures. High Pressures, 29(1):73–79, 1997.

[48] PL Owen and CK Thornhill. The Flow in an Axially Symmetric Supersonic Jet from a Nearly Sonic Orifice Into a Vacuum. Aeronautical Research Council (U.K.) R & M No. 2616, 1948.

[49] Aránzazu Pérez and José A Moríñigo. Computational efficiency of the inflow boundary conditions in dsmc simulation. In 28TH INTERNATIONAL SYMPOSIUM ON RAREFIED GAS DYNAMICS 2012, volume 1501, pages 601–608. AIP Publishing, 2012.

[50] Helge Petersen. The properties of helium: density, specific heats, viscosity, and thermal conductivity at pressures from 1 to 100 bar and from room temperature to about 1800 K. Report 224, Danish Atomic Energy Commission, 1970.

[51] H.W. Rohrs, C.T. Wickham-Jones, G.B. Ellison, D. Berry, and B.M. Argrow. Fourier transform infrared absorption spectroscopy of jet-cooled radicals. Review of Scientific Instruments, 66(3):2430–2441, March 1995.

[52] Samuel A. Schaaf and Paul L. Chambre. Flow of Rarefied Gases. Princeton University Press, 1961.

[53] A. M. Scheer, C. Mukarakate, G. B. Ellison, D. J. Robichaud, and M. R. Nimlos. Radical chemistry in the thermal decomposition of anisole and deuterated anisoles: An investigation of aromatic growth. Journal of Physical Chemistry A, 114(34):9043–9056, 2010.

[54] A.M. Scheer, C. Mukarakate, D.J. Robichaud, M.R. Nimlos, H.-H. Carstensen, and G.B. Ellison. Unimolecular thermal decomposition of phenol and d_5-phenol: Direct observation of cyclopentadiene formation via cyclohexadienone. Journal of Chemical Physics, 136:044309, 2012.

[55] A.M. Scheer, C. Mukarakate, D.J. Robichaud, M.R. Nimlos, and G.B. Ellison. Thermal decomposition mechanisms of the methoxyphenols: Formation of phenol, cyclopentadienone, vinylacetylene and acetylene. Journal of Physical Chemistry A, 115:13381–13389, 2011.

[56] TE Schwartzentruber, LC Scalabrin, and ID Boyd. A modular particle–continuum numerical method for hypersonic non-equilibrium gas flows. Journal of Computational Physics, 225(1):1159–1174, 2007.

[57] Thomas E Schwartzentruber and Iain D Boyd. A hybrid particle-continuum method applied to shock waves. Journal of Computational Physics, 215(2):402–416, 2006.

[58] Thomas Edward Schwartzentruber. A Modular Particle-Continuum Numerical Algorithm for Hypersonic Non-equilibrium Flows. PhD thesis, The University of Michigan, 2007.

[59] Nathaniel Selden, Natalia Gimelshein, Sergey Gimelshein, and Andrew Ketsdever. Analysis of accommodation coefficients of noble gases on aluminum surface with an experimental/computational method. Physics of Fluids, 21(7):073101, 2009.

[60] A.H. Shapiro. Compressible Fluid Flow, Vols. 1 & 2. Roland Press, 1953.

[61] FS Sherman. Technical report: Fluid mechanics 6-90-63-61. Lockheed Missiles and Space Co., Sunnyvale, California, 1963.

[62] Krist Sherrie L, Biedron Robert T, and Rumsey Christopher L. Cfl3d user"s manual (version 5.0). 1998.

[63] Steven J Sibener, Richard J Buss, Cheuk Yiu Ng, and Yuan T Lee. Development of a supersonic o (3pj), o (1d2) atomic oxygen nozzle beam source. Review of Scientific Instruments, 51(2):167–182, 1980.

[64] Quanhua Sun and Iain D Boyd. A direct simulation method for subsonic, microscale gas flows. Journal of Computational Physics, 179(2):400–425, 2002.

[65] Zhi-Xin Sun, Zhen Tang, Ya-Ling He, and Wen-Quan Tao. Proper cell dimension and number of particles per cell for dsmc. Computers & Fluids, 50(1):1–9, 2011.

[66] Eleuterio F Toro and Eleuterio F Toro. Riemann solvers and numerical methods for fluid dynamics, volume 16. Springer, 1999.

[67] R. S. Tranter, R. Sivaramakrishnan, N. Srinivasan, and K. Brezinsky. Calibration of reaction temperatures in a very high pressure shock tube using chemical thermometers. International Journal of Chemical Kinetics, 33:722–731, 2001.

[68] Stephen R. Turns. An Introduction to Combustion: Concepts and Applications. McGraw Hill, 1996.

[69] Kimberly N. Urness. Pyrolysis of Biomass-Derived Fuels in a Heated Microtubular Reactor. PhD thesis, University of Colorado, 2014.

[70] Kimberly N. Urness, Q. Guan, Amir Golan, John W. Daily, Mark R. Nimlos, John F. Stanton, Musa Ahmed, and G. Barney Ellison. Pyrolysis of furan in a microreactor. J. Chem. Phys., 139:124305–124314, 2013.

[71] NB Vargaftik and LV Yakush. Temperature dependence of thermal conductivity of helium. Journal of Engineering Physics and Thermophysics, 32(5):530–532, 1977.

[72] PV Vashchenkov, AN Kudryavtsev, DV Khotyanovsky, and MS Ivanov. Dsmc and navier-stokes study of backflow for nozzle plumes expanding into vacuum. Technical report, DTIC Document, 2005.

[73] A. Vasiliou, K. M. Piech, X. Zhang, M. R. Nimlos, M. Ahmed, A. Golan, O. Kostko, D. L. Osborn, J. W. Daily, J. F. Stanton, and G. B. Ellison. The products of the thermal decomposition of ch3cho. Journal of Chemical Physics, 135(1):14306–14311, 2011.

[74] A.K. Vasiliou, M.R. Nimlos, J.W. Daily, and G.B. Ellison. Thermal decomposition of furan generates propargyl radicals. Journal of Physical Chemistry A, 113:8540–8547, 2009.

[75] Angayle Vasiliou, Krzysztof Piech, G Barney Ellison, Mark R Nimlos, John W Daily, and John F Stanton. Thermal Decomposition of Acetaldehyde Studied by Matrix IR and PIMS Spectroscopy. In 65th International Symposium On Molecular Spectroscopy, 2010.

[76] AnGayle K Vasiliou, Jong Hyun Kim, Thomas K Ormond, Krzysztof M Piech, Kimberly N Urness, Adam M Scheer, David J Robichaud, Calvin Mukarakate, Mark R Nimlos, John W Daily, et al. Biomass pyrolysis: Thermal decomposition mechanisms of furfural and benzaldehyde. The Journal of chemical physics, 139(10):104310, 2013.

[77] Wolfgang Wagner. A convergence proof for bird's direct simulation monte carlo method for the boltzmann equation. Journal of Statistical Physics, 66(3-4):1011–1044, 1992.

[78] JF Wehner and RH Wilhelm. Boundary conditions of flow reactor. Chemical engineering science, 6:89–93, 1956.

[79] F.A. Williams. Combustion Theory: The Fundamental Theory of Chemically Reacting Flow Systems. Addison-Wesley, NYC, 1985.

[80] Richard G Wilmoth, Robert A Mitcheltree, James N Moss, and Virendra K Dogra. Zonally decoupled direct simulation monte carlo solutions of hypersonic blunt-body wake flows. Journal of Spacecraft and Rockets, 31(6):971–979, 1994.

[81] J-S Wu, W-J Hsiao, Y-Y Lian, and K-C Tseng. Assessment of conservative weighting scheme in simulating chemical vapour deposition with trace species. International Journal for Numerical Methods in Fluids, 43(1):93–114, 2003.

[82] J-S Wu, Y-Y Lian, G Cheng, RP Koomullil, and K-C Tseng. Development and verification of a coupled dsmc–ns scheme using unstructured mesh. Journal of Computational Physics, 219(2):579–607, 2006.

[83] Li Xinlang, Fu Dexun, Ma Yanwen, and Liang Xian. Development of high-order cfd software hoam-opencfd. e-Science Technology & Application, 1(1):46–53, 2010.

[84] X. Zhang, A.V. Friderichsen, S. Nandi, G.B. Ellison, D.E. David, J.T. McKinnon, T.G. Lindeman, D.C. Dayton, and M.R. Nimlos. Intense, hyperthermal source of organic radicals for matrix-isolation spectroscopy. Review of Scientific Instruments, 74(6):3077–3086, June 2003.

Appendix A

Physical Properties of He, Ne, Ar and SiC

The transport properties of He, Ne and Ar that we use in our CFD simulations are those given by Petersen [50], Bich [8], Vargaftik [71] and Dawe [28].

Either helium or argon can be used as the carrier noble gas in this study. Their physical properties are listed in Table A.1.

Table A.1: Physical properties of helium, neon and argon

Properties (unit)	Helium	Neon	Argon
Density (kg/m^3)	ideal-gas	ideal-gas	ideal-gas
Cp (Specific Heat) (J/kg − K)	5193	1029.9	520.64
Thermal conductivity (W/m − K)	polynomial	polynomial	polynomial
Viscosity (kg/m − s)	power-law	power-law	power-law
Molecular weight (g/mol)	4.0026	20.183	39.996
Molecular diameter (Å)	2.33	2.82	4.17

Thermal conductivity of helium and argon are computed as polynomial functions of temperature with the following expressions:

$$\kappa_{\mathrm{He}} = 4.76 \times 10^{-2} + 3.62 \times 10^{-4}T - 6.18 \times 10^{-8}T^2 + 7.18 \times 10^{-12}T^3 \text{ (W/m-K)} \tag{A.1}$$

$$\kappa_{\mathrm{Ne}} = 1.59 \times 10^{-2} + 1.22 \times 10^{-4}T - 3.37 \times 10^{-8}T^2 + 6.43 \times 10^{-12}T^3 \text{ (W/m-K)} \tag{A.2}$$

$$\kappa_{\mathrm{Ar}} = 5.47 \times 10^{-3} + 4.73 \times 10^{-5}T - 1.11 \times 10^{-8}T^2 + 1.60 \times 10^{-12}T^3 \text{ (W/m-K)} \tag{A.3}$$

While viscosities are computed as power-law functions of temperature:

$$\mu_{\mathrm{He}} = 3.674 \times 10^{-7}T^{0.70} \text{ (kg/m-s)} \tag{A.4}$$

$$\mu_{\mathrm{Ne}} = 7.006 \times 10^{-7} T^{0.67} \text{ (kg/m-s)} \tag{A.5}$$

$$\mu_{\mathrm{Ar}} = 4.059 \times 10^{-7} T^{0.71} \text{ (kg/m-s)} \tag{A.6}$$

These relations are plotted in Figs. A.1 and A.2.

Figure A.1: Thermal conductivity of helium and argon

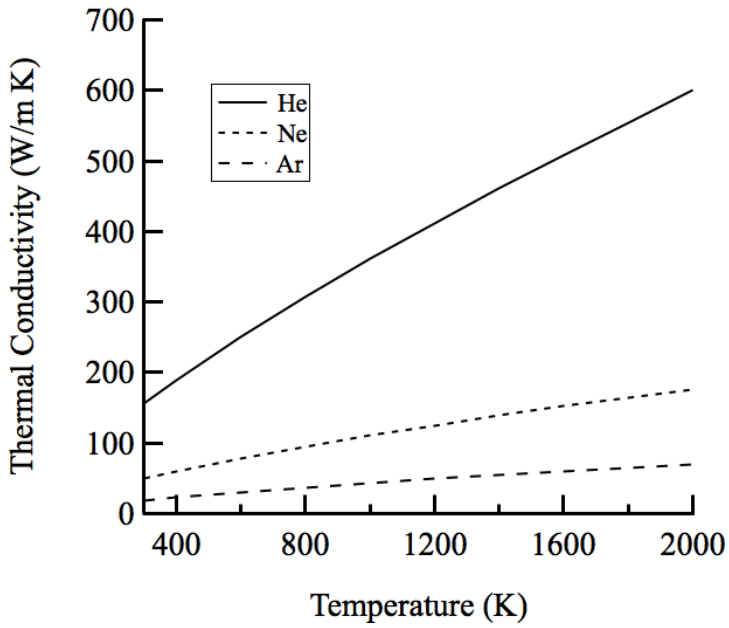

The physical properties of SiC are listed in Table A.2:

Since the reactor walls are included as part of the CFD computation, the thermal conductivity of SiC is needed. We use the following expression from Nilsson [47]:

$$k_{\mathrm{SiC}} = \begin{cases} \frac{61100}{T-115} & \text{if } 300\text{K} < T \leq 1800\text{K}, \\ & \text{(W/m-K)} \\ 360 & \text{if } T \leq 300\text{K} \end{cases} \tag{A.7}$$

Figure A.2: Dynamic viscosity of helium and argon

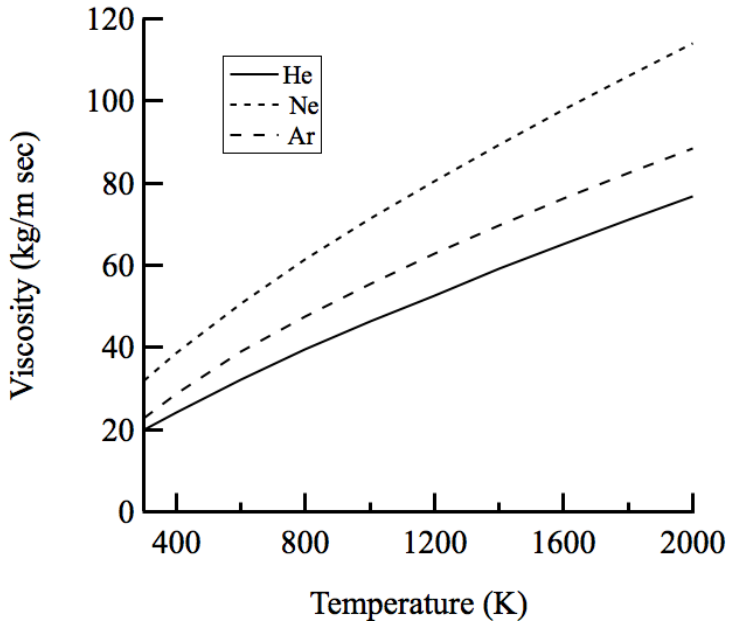

Table A.2: Physical properties of SiC

Properties (unit)	SiC
Density (kg/m^3)	3210
Cp (Specific Heat) (J/kg − K)	750
Thermal conductivity (W/m − K)	$\kappa(T)$

Appendix B

The Navier-Stokes Equations

The complete form of the Navier-Stokes equations can be found in textbooks such as Williams [79]. Here we treat the flow as axisymmetric about the centerline and make some assumptions that are common for large aspect ratio axisymmetric flows (see Turns [68]). The coordinate system used is shown in Fig. B.1.

Figure B.1: Axisymmetic coordinate system used in simulations

Conservation of Mass

$$\frac{1}{r}\frac{\partial r\rho u_r}{\partial r} + \frac{\partial \rho u_z}{\partial z} = 0 \tag{B.1}$$

Conservation of Individual Species

$$\frac{1}{r}\frac{\partial(r\rho u_r Y_i)}{\partial r} + \frac{1}{r}\frac{\partial(r\rho u_z Y_i)}{\partial z} = -\frac{1}{r}\frac{\partial}{\partial r}\left(r\rho D_i \frac{\partial Y_i}{\partial r}\right) + \dot{m}_i''' \tag{B.2}$$

where Y_i is the mass fraction, D_i is the mass diffusion coefficient for diffusion of species i with respect to the carrier gas, and $\dot{m}_i'''$ is the mass production rate of species i due to chemical reactions.

Conservation of Momentum

$$\frac{1}{r}\frac{\partial(r\rho u_z u_z)}{\partial z} + \frac{1}{r}\frac{\partial(r\rho u_z u_r)}{\partial r} = \frac{1}{r}\frac{\partial}{\partial r}\left(r\mu\frac{\partial u_z}{\partial r}\right) \tag{B.3}$$

Here μ is the dynamic viscosity.

Conservation of Energy

$$\frac{1}{r}\frac{\partial(r\rho u_z \int c_p dT)}{\partial z} + \frac{1}{r}\frac{\partial(r\rho u_r \int c_p dT)}{\partial r} = \frac{1}{r}\frac{\partial}{\partial r}\left(r\rho D\frac{\partial \int c_p dT}{\partial r}\right) - \sum h^o_{f,i}\dot{m}'''_i \tag{B.4}$$

$h^o_{f,i}$ is the enthalpy of formation for species i, and $-\sum h^o_{f,i}\dot{m}'''_i$ represents the rate of sensible enthalpy production by chemical reaction per unit volume.

We also require the p-v-T equation of state:

$$p = \rho RT\sum_{i=1}^{N}\frac{Y_i}{W_i} \tag{B.5}$$

The mole and mass fractions are related by:

$$x_i = \frac{(Y_i/W_i)}{\sum\limits_{j=1}^{N}(Y_j/W_j)} \tag{B.6}$$

The transport properties many be obtained theoretically from the Chapman-Enskog solution of the Boltzmann equation or from experiment (Bird, Stewart and Lightfoot [14]).

Appendix C

CFD: Conversion from 2D to 2D axially symmetric

The original FVM code is designed for 2D flow simulations, in order to simulate an axisymmetric flow, changes are made on the source terms and fluxes terms. An arbitrary 2D quadrilateral finite volume cell (see Fig. C.1) is shown to facilitate the illustration.

Figure C.1: Computing cycle of typical CFD programs

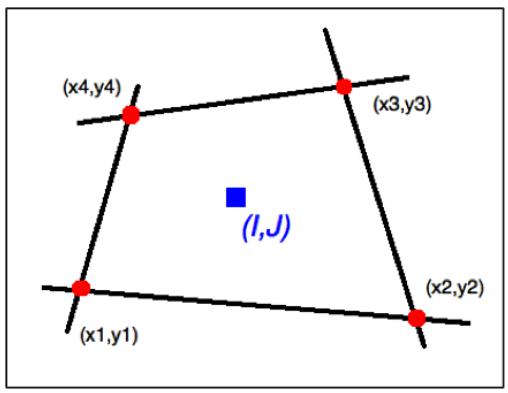

During the computation, geometry information such as the edge lengths, normal components and cell volume are computed and stored. To convert from 2D to 2D axisymmetric, one has to fix the axis on the x coordinate. Then changes are made to compute the metrics of cell faces and volume by considering about the circumferential lengths of each edge. For the left edge of the cell shown in Fig. C.1, the area is:

$$S_{2DA} = \pi(y_4 + y_1)S_{2D} \tag{C.1}$$

where

$$S_{2D} = \sqrt{(y_4 - y_1)^2 + (x_4 - x_1)^2} \tag{C.2}$$

is the area of edge 14 in two dimensional case.

For the volume of the cell, we have:

$$\Omega_{2DA} = \Omega_{2D}(y_1 + y_2 + y_3 + y_4)/4 \tag{C.3}$$

where

$$\Omega_{2D} = [(x_1 - x_3)(y_2 - y_4) + (x_4 - x_2)(y_1 - y_3)]/2 \tag{C.4}$$

stands for the cell volume in two dimensional case.

Lastly, by mathematical derivation, a source term is added on the right hand side of y-momentum equation [34]:

$$S = \frac{V_{2DA}}{y}p + \frac{1}{Re}\frac{2}{3}\frac{\mu}{y}\left[-2\frac{V_{2DA}}{y}v + \frac{\partial}{\partial\xi}(\xi_x u + \xi_y v) + \frac{\partial}{\partial\eta}(\eta_x u + \eta_y v)\right] \tag{C.5}$$

Here p is pressure and μ is the viscosity while ξ and η represent the I and J directions respectively in a structured grid.